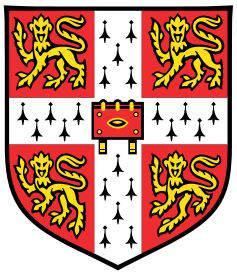

Understanding the Collective Dynamics of Motile Cilia in Human Airways

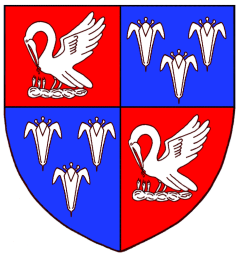

Luigi Feriani

Department of Physics
University of Cambridge

This dissertation is submitted for the degree of
Doctor of Philosophy

Corpus Christi College April 2018

Understanding the Collective Dynamics of Motile Cilia in Human Airways

Luigi Feriani

Eukaryotic organisms rely on the coordinated beating of motile cilia for a multitude of fundamental reasons. In smaller organisms, such as *Paramecium* and the single cell alga *Chlamydomonas reinhardtii*, it is a matter of propulsion, to swim towards a higher concentration of nutrients or away from damaging environments. Larger organisms use instead the coordinated motion of cilia to push fluid along an epithelium: examples common to mammals are the circulation of cerebrospinal fluid in the brain, the transport of ovules in the fallopian tubes, and breaking the left/right symmetry in the embryo. Another notable example, and one that is central to this thesis, is mucociliary clearance in human airways: A carpet of motile cilia helps keeping the cell surface free from pathogens and foreign particles by constantly evacuating from lungs, bronchi, and trachea a barrier of mucus.

The question of how motile cilia interact with one another to beat in a coordinated fashion is an open and pressing one, with immediate implications for the medical community. In order for the fluid propulsion to be effective, the motion of cilia needs to be phase-locked across significant distances, in the form of travelling waves ("metachronal waves"). It is still not known how this long-range coordination emerges from local rules, as there is no central node regulating the coordination among cilia.

In the first part of this thesis I will focus on studying the coordination in carpets of cilia with a top-down approach, by proposing, implementing, and applying a new method of analysing microscope videos of ciliated epithelia.

Chapter 1 provides the reader with an introduction on motile cilia and flagella, treating their structure and motion and reporting the different open questions currently tackled by the scientific community, with particular interest in the coordination mechanisms of cilia and the mucociliary clearance apparatus.

Chapter 2 introduces Differential Dynamic Microscopy (DDM), a powerful and versatile image analysis tool that bridges the gap between spectroscopy and microscopy by allowing to perform scattering experiments on a microscope. The most interesting aspects of DDM for this work are that it can be applied to microscope videos where it is not possible to resolve individual objects in the field of view, and it requires no user input. These two characteristics make DDM a perfect candidate for analysing several hundred microscope videos of weakly scattering filaments such as cilia.

In Chapter 3 I will present how it is possible to employ DDM to extract a wealth of often-overlooked information from videos of ciliated epithelia: DDM can successfully probe

the ciliary beat frequency (CBF) in a sample, measure the direction of beating of the cilia, and detect metachronal waves and read their direction and wavelength. *In vitro* ciliated epithelia however often do not show perfect coordination or alignment among cilia. For the analysis of these samples, where the metachronal coordination might not be evident, we developed a new approach, called multiscale DDM (multiDDM), to measure a coordination length scale, a characteristic length of the system over which the coordination between cilia is lost.

The new technique of multiDDM is employed in Chapter 4 to study how the coordination among cilia changes as a response to changes in the rheology of the mucous layer. In particular, we show that cilia beating under a thick, gel-like mucus layer show a larger coordination length scale, as if the mucus acted as an elastic raft effectively coupling cilia over long distances. This is corroborated by the coordination length scale being larger in samples from patients affected by Cystic Fibrosis than in healthy samples, and much shorter when the mucus layer is washed and cilia therefore beat in a near-Newtonian fluid. We then show how it is possible to employ multiDDM to measure the effectiveness of drugs in recovering, in CF samples, a coordination length scale typical of a healthy phenotype.

In the second part I will focus instead on the single cilium scale, showing how we can attempt to link the beating pattern of cilia to numerical simulations studying synchronisation in a model system.

In particular in Chapter 5 I will describe our approach to quantitatively describe the beating pattern of single cilia obtained from human airway cells of either healthy individuals or patients affected by Primary Ciliary Dyskinesia. Our description of the beating pattern, and the selection of a few meaningful, summary parameters, are then shown to be accurate enough to discriminate between different mutations within Primary Ciliary Dyskinesia.

In Chapter 6 instead I report the results obtained by coarse-graining the ciliary beat pattern into a model system consisting of two “rotors”. The rotors are simulated colloidal particles driven along closed trajectories while leaving their phase free. In my study, the trajectories followed by the rotors are analytical fits of experimental trajectories of the centre of drag of real cilia. The rotors, that are coupled only via hydrodynamics interactions, are seen to phase-lock, and the shape of the trajectory they are driven along is seen to influence the steady state of the system.

Declaration

I hereby declare that except where specific reference is made to the work of others, the contents of this dissertation are original and have not been submitted in whole or in part for consideration for any other degree or qualification in this, or any other university. This dissertation is my own work and contains nothing which is the outcome of work done in collaboration with others, except as specified in the text and Acknowledgements. This dissertation contains fewer than 60,000 words including appendices, bibliography, footnotes, tables and equations and has fewer than 150 figures.

Luigi Feriani
April 2018

Acknowledgements

The last four years have been long, full, and extremely interesting, both in and outside the lab. Many people have contributed to making them so, and this space will see me trying to thank them all as it is fit.

First of all, I would like to thank my supervisor, Pietro Cicuta, first for taking me into his group and then for the advice, guidance, invaluable inputs, and stimuli he gave me throughout my PhD. A massive thank you goes to Jurij Kotar, without whom the entire group would probably implode, and who, besides designing, building, or improving most of the equipment I ended up using, taught me so much. A thank you is a must to Maurizio Chioccioli, for a long and productive collaboration, and for bearing the brunt of some seriously tedious analysis. I am grateful to all the scientific collaborators who provided us with the samples and material without which, literally, this work would not have happened. In no particular order: Cedar J. Fowler, Preston E. Bratcher, Max Seibold, and Vito Mennella. I would also like to thank Nicolas Bruot, for the valuable and insightful discussions about the rotors model.

A never-ending thank you to all past and present members of Pietro's group, and to all my friends for making my time in Cambridge so memorable. I owe you all much, and I will miss you. Roughly in chronological order: Lorenzo and Jessica, Lucia and Avelino, Euggenia and Armandino, Nicolas, Mia, Di, Emma, Evelyn, Ryan, Omar, Sho, Nicola, Viola, Chiara, Cornelius, ...

A special thank you to Evelyn, for making my life in the past two and a half years so, so much better. And also for putting up with me while I was in stressed-panicky-thesis-writing mode.

Finally, I would like to thank my family, and in particular my mother and my sister, for supporting, believing in, and standing by me in every moment.

Table of contents

List of figures

Nomenclature

Acronyms / Abbreviations

ALI Air Liquid Interface

CBF Ciliary Beat Frequency

CBP Ciliary Beat Pattern

CF Cystic Fibrosis

CFTR CF Transmembrane Conductance Regulator

DDM Differential Dynamic Microscopy

multiDDM Multiscale DDM

DLS Dynamic Light Scattering

DMSO Dimethyl Sulfoxide

ENaC Epithelial Sodium Channel

FFT Fast Fourier Transform

FOV Field of View

HAECs Human Airway Epithelial Cells

HSVM High Speed Video Microscopy

ISF Image Structure Function

MCC Mucociliary Clearance

MW Metachronal Wave

PBS Phosphate-buffered Saline

PCA Principal Component Analysis

PCD Primary Ciliary Dyskinesia

PCL Periciliary Layer

PCP Planar Cell Polarity

PIV Particle Image Velocimetry

PSF Point Spread Function

PT Particle Tracking

RFT Resistive Force Theory

Publications list

Some chapters of this thesis are partly reproduced from the following research articles:

- **Assessing the Collective Dynamics of Motile Cilia in Cultures of Human Airway Cells by Multiscale DDM**
  L. Feriani, M. Juenet, C. J. Fowler, N. Bruot, M. Chioccioli, S. M. Holland, C. E. Bryant, and P. Cicuta
  Biophysical Journal, vol. 113, no. 1, pp.109-119, 2017, doi:10.1016/j.bpj.2017.05.028

- **Phenotyping ciliary dynamics and coordination in response to CFTR-modulators in Cystic Fibrosis respiratory epithelial cells**
  M. Chioccioli,* L. Feriani,* J. Kotar, P. E. Bratcher,† and P. Cicuta†
  Submitted, 2018

Chapter 1

Cilia and flagella

1.1 Microscopic flow is a fundamental characteristic of life

Many physiological processes depend on the ability of an organism to generate a net flow of fluid. Microorganisms have to be able to swim along gradients of concentrations towards regions richer in nutrients ("chemotaxis"), or with the right amount of light: for example, the ciliated alga *Chlamydomonas reinhardtii* is [1] able to swim towards dim lights and away from lights too bright, phenomenon known as "phototaxis". Multicellular organisms too have physiological processes that require the generation of flow. A notable example of this is mucociliary clearance in human airways, where the mucus present in the airways has to be constantly evacuated from lungs, bronchi and trachea. Other examples common to mammals are the circulation of cerebrospinal fluid in the brain [2], transport of ovules in the fallopian tube [3], and breaking the left/right symmetry in the embryo [4, 5]. In all such processes fluid flow is generated in a similar way, thanks to motile cilia.

The cilia of eukaryotes are sometimes called flagella in the case of single cell motility, but should not be confused with the very different flagella of motile bacteria [6].

In this chapter is a brief overview of cilia: section 1.2 treats their structure and motion, in section 1.3 are reported the different open questions that are currently being tackled, with the prominent question about their coordination mechanisms examined in more depth in section 1.4. Section 1.5 covers the mechanism of mucociliary clearance while section 1.6 reports instead imaging and analysis techniques that have been employed - both historically and more recently - to study eukaryotic cilia and flagella.

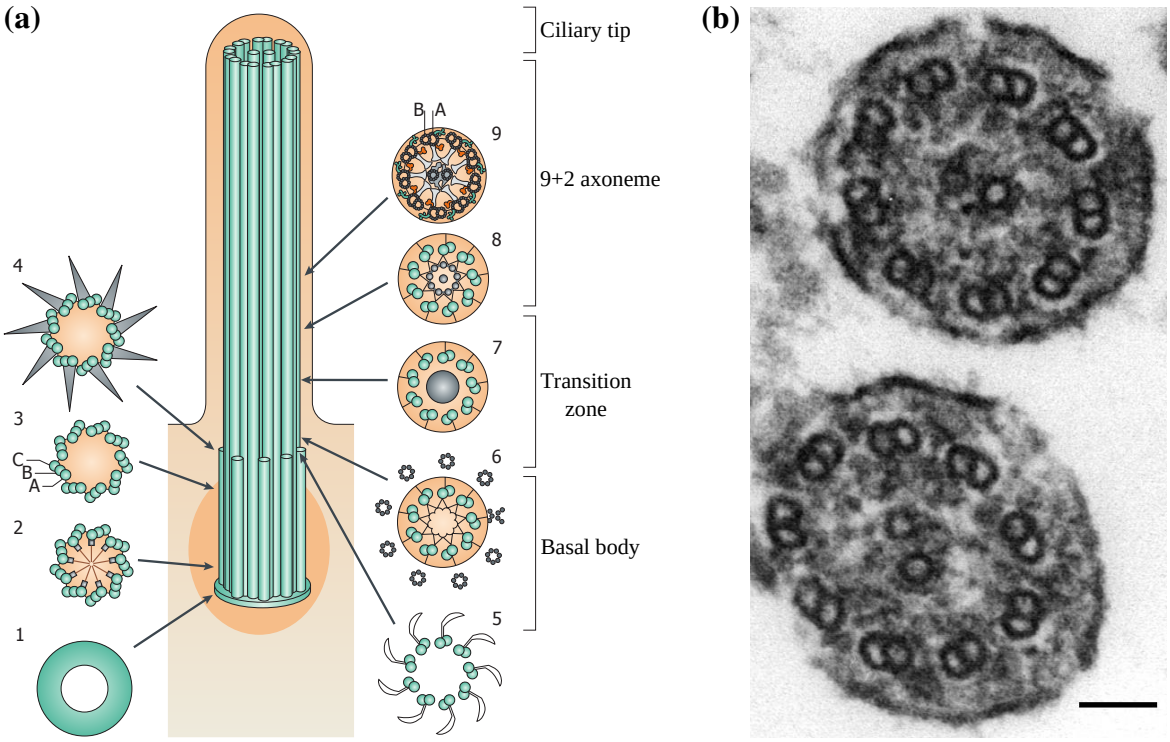

Fig. 1.1 **Structure of a motile cilium. (a)** Schematic representation of a eukaryotic motile cilium. The structural core of a motile cilium is the axoneme, composed by nine peripheral microtubule doublets, comprising an A- and a B-tubule, and two inner microtubule singlets (9+2 structure). Inner and outer dynein arms attached to the A-tubules ensure ciliary bending by reversely binding to the B-tubule. Adapted from [7]. **(b)** Cross-section of motile cilia, obtained by imaging a thin section cut through the bronchiolar area of lung of a mouse via transmission electron microscope. The outer microtubule doublets and the inner microtubule singlets are clearly visible. Scale bar is $60\,\mathrm{nm}$. Adapted from [8], available online at remf.dartmouth.edu/.

1.2 Structure and motion of motile eukaryotic cilia

Cilia are cell organelles, slender protuberances that stick out of the surface of many eukaryotic cells [9, 10]. They are covered in cellular membrane, and contain a bundle of microtubules called axoneme. In virtually all cases, the axoneme can have one of two structures: 9+2, with 9 doublet microtubules arranged radially around two central singlet microtubules (Figure 1.1), and 9+0, where the two central microtubules are missing. Their structure underpins their function. Cilia missing the two central microtubules are called “primary cilia”, they are not motile and have been reported to act as chemical or mechanical sensors [11–13]. Cilia with a 9+2 axoneme are instead motile cilia: a complex of molecular motors (“axonemal dyneins”, missing in primary cilia) can make the microtubule doublets slide on one another, causing the entire cilium to bend. This mechanism enables motile cilia to generate a fluid flow [12]. A few

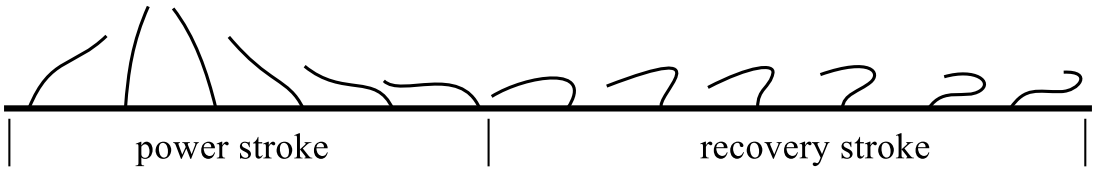

Fig. 1.2 **Beating pattern of motile cilia.** Sketch of the beating pattern of a motile cilium. The cilium moves with a periodic pattern, composed of two strokes. In the power stroke the cilium is extended, and moves fast. A slower movement in a curled configuration is then performed to return to the initial position (recovery stroke). This asymmetry of the two strokes makes the beating cycle non reciprocal, condition required to create a net flow in low-Reynolds number regimes [19]. The horizontal direction can be thought of as “time", but alternatively “space" in the case of a ciliated tissue supporting collective waves. Figure adapted from [20].

exceptions to this categorisation are nodal cilia and *Anguilla* sperm, which are motile despite their 9+0 configuration [14]. Their motion however is very different from the planar beating of 9+2 motile cilia: nodal cilia move with a conical motion while *Anguilla* sperm propels itself with the propagation of helicoidal waves along the flagellum (a screw-like motion) [15]. Finally, motile flagella, in some rare cases, can have an axoneme with a different number of microtubule doublets [14].

Cilia assemble from the bottom up, starting from the basal body which is docked in the cell membrane and connected to the cytoskeleton. From the basal body grows the axoneme, which then keeps growing from the tip thanks to a transport system of proteins along the axoneme itself [16]. The orientation of the basal body dictates the direction of the beat, and it is not defined during ciliogenesis. The process with which cilia orient themselves along a preferred direction is still being studied, although there is strong evidence that hydrodynamic interactions play a fundamental role [17, 18].

The structure of cilia is quite well known, while the dynamics is well characterised only in a few model organisms such as *Chlamydomonas reinhardtii*, *Paramecium caudatum*, and sperm cells [21–23]. In other interesting systems, as in the ciliated cells that cover human airways, the level of detail has so far been much lower, mainly because of the great number of cilia per cell and the presence of mucus that hinders imaging [24, 25]. What it is well known is that the filaments oscillate with a non-reciprocal motion in time. A sketch of one of the typical cycles is in Figure 1.2. The motion can be divided in two parts, or strokes. In the first part, called “power stroke”, the cilium is extended in order to maximise drag with the fluid, and moves fast. In the second part, the “recovery stroke”, the cilium curls

up to minimise interaction with the fluid and slowly returns to the initial configuration [26]. The asymmetry between the two strokes is what makes the cycle non-reciprocal, condition imposed by Purcell's scallop theorem to generate a flow in low Reynolds number [19]. This cycle can be repeated up to 100 times per second, although mammalian airway ciliary beat frequency is mostly reported to be between 10 and $20\,\mathrm{Hz}$ [12].

Not all motile cilia have the same beating cycle: for example, uniflagellar spermatozoa propel themselves by moving their flagellum in a wavelike, planar motion (as a snake slithering on the ground) or with a helical pattern (as a corkscrew) [27].

Dimensions of motile cilia can vary greatly: while the thickness is fairly consistently about 200-$300\,\mathrm{nm}$, the length of the filaments spans orders of magnitude. For example, cilia in the human airways are in average $7\,\mu\mathrm{m}$ long [28], flagella in *Chlamydomonas* are about $12\,\mu\mathrm{m}$ in length [29], spermatozoa are $28\,\mu\mathrm{m}$ long in the porcupine *Hystrix africaeaustralis* but $349\,\mu\mathrm{m}$ in the honey possum *Tarsipes rostratus* (not to mention invertebrate sperm that can reach a few millimetres in length) [30].

1.3 Understanding cilia motility requires an interdisciplinary effort

Motile cilia are structurally conserved, allowing motility in single cell eukaryotes and transport of fluids along cell epithelia in multicellular organisms [31].

Understanding cilia motility requires concepts and a deep understanding from many fields, from cell biology and medicine, to fluid dynamics, soft matter and non-linear physics [32]. Questions range over many scales: at the level of the individual organelle we want to know the metabolic path in ciliary motion, the molecular structures involved in this organelle's assembly and function, and how a cilia waveform for efficient beating is achieved [25, 33]; At the level of tissues, how many of these beating filaments coordinate with each other, the importance of arrangement, density, fluid physical parameters, and then the role played by cilia generated flows in key biological processes such as symmetry breaking and onset of planar cell polarity in development [4, 5, 17, 34, 35]. The medical community has parallel questions in understanding how cilia malfunction is related to various pathologies [36–39], and very practically how to relate imaging of ciliary beating to the diagnosis of such pathologies. Finally, cilia are studied in engineering to replicate biomimetically their capacity of creating flow in low Reynolds number environments [40], or even to try and build micro-robots [41].

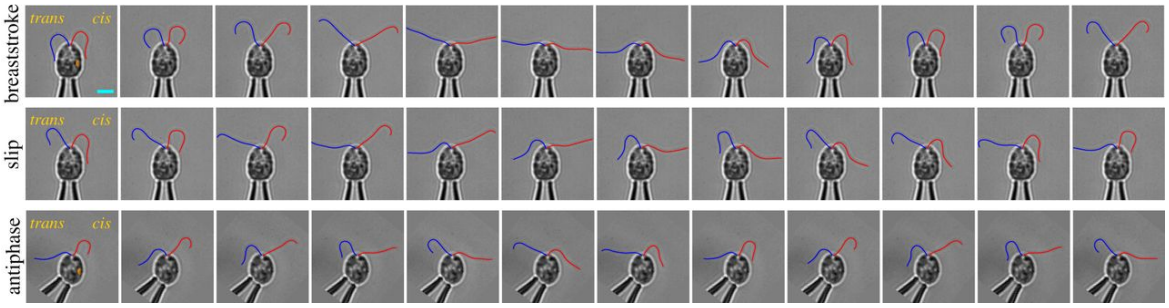

Fig. 1.3 **Beating pattern of *Chlamydomonas*. (top)** Typical, in phase beating pattern of *Chlamydomonas reinhardtii*, resembling a breaststroke motion. **(middle)** Synchronisation is lost and a phase-slip occurs. **(bottom)** Flagella beating in anti-phase synchronisation, recently discovered to be possible in a mutant strain. Red curves highlight the *cis* flagellum (i.e. the closest to the photoreceptor, in orange), blue curves the *trans* flagellum. Figure taken from [47].

1.4 Coordinated motion

A crucial element from the scenario described above is how the coordinated motion of cilia arises, and how the collective state (e.g. travelling wave) properties relate to the mechanisms and mechanics of the individual beating filaments. This can be addressed either with a bottom-up approach, modelling each cilium with something simpler and studying synchronisation of a few model cilia (our group's previous work in that direction is reviewed in [32]), or with a top-down approach, i.e. characterising the collective motion in real systems and trying to infer some information about the properties at the single cilium level. In either case, one needs to appreciate that the single cilium itself is a complex non-linear dynamical system functioning out of thermal equilibrium, and described by many degrees of freedom [42].

Cilia within the same cell are mechanically connected through the cytoskeleton [31], and are immersed in a fluid which in the case of the airways displays viscoelasticity and complex heterogeneous composition that are critical for mucociliary clearance [43].

The conclusion that can be drawn from model experiments in our group so far [32] is that hydrodynamic coupling is sufficient to promote strong synchronization through various mechanisms, and in simple systems it is possible to link the emergent behaviour to the details of how each cilium is driven [44, 45], and how cilia are spatially arranged relative to each other [18, 46].

1.4.1 Cilia synchronisation in *Chlamydomonas reinhardtii*

A well-studied example of synchronisation between flagella is the observed behaviour of the model organism *Chlamydomonas reinhardtii* (Figure 1.3), that has been drawing the

attention of the physics community in recent years thanks to its fairly simple configuration but rich behaviour. The two flagella of this alga beat in phase in a cyclic pattern resembling a "breaststroke" motion for most of the time. Such motion is interrupted by some short periods of phase drift, in which the two flagella move asynchronously. The swimming of the alga is of course affected by this change of stroke: it will swim straight while the two flagella are in sync, and change direction during the out-of-sync period, resulting in what is effectively a eukaryotic version of the "run-and-tumble" motion so common in bacteria [48].

Fairly recently, evidence emerged that mechanical coupling of the flagella through the central body gives an important contribution to flagellar synchronisation in *Chlamydomonas* [49–51]. However, experiments on somatic cells from the colonial alga *Volvox carterii* showed that their flagella, which are very similar to *Chlamydomonas*'s, can synchronise purely via hydrodynamics coupling [52].

1.4.2 Metachronal waves

When cilia are arranged in a tight two-dimensional array as in human airways, or on the outer surface of *Paramecium*, a particular type of collective motion has been observed: Neighbouring cilia do not beat in phase, but maintain a constant, small phase difference (as can be seen in Figure 1.4). This yields without a central organising node (i.e. just out of 'local' rules) a propagating pattern called "metachronal wave" [53–56]. Cilia beat is optimized for fluid transport [33], and according to recent theoretical studies [57] metachronal waves are retrieved when trying to maximise the efficiency of a cilia array in generating a net flow, suggesting that hydrodynamic coupling plays a fundamental role in the swimming of microorganisms and in mucociliary clearance in human airways. Other studies also strongly suggest hydrodynamic coupling to be the mechanism through which cilia metachronality arises [28, 58].

Understanding the physics of how the coordinated behaviour of cilia emerges is still an open question, currently studied both on model organisms [59], and on model systems [32, 52, 60]. In general we still do not fully know how the collective dynamics yield such a fascinating emergent behaviour at a tissue scale.

1.4.3 Synchronisation in model systems

As mentioned above, our group has already started tackling the problem of of cilia synchronisation using model systems, in particular through the work of Dr Nicolas Bruot during his PhD.

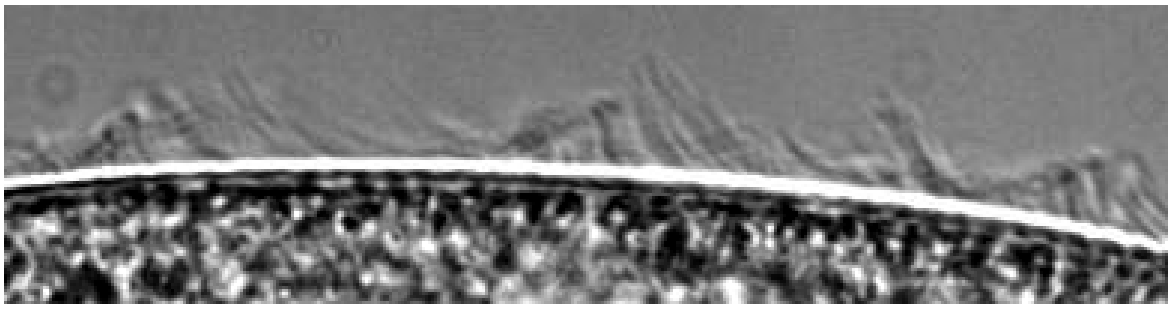

Fig. 1.4 **Metachronal wave in a *Paramecium*.** Neighbouring cilia on the outer surface of *Paramecium* beat keeping a small, constant phase difference. This leads to the formation of a metachronal wave, with wave length in the order of tens of cilia. Image taken from [61], available online at cellsystem.sci.yamaguchi-u.ac.jp/.

The key idea is that in the far field the hydrodynamic flow generated by a moving cilium can be approximated with the one generated by a spherical bead [62]. This allows one to coarse-grain the many degrees of freedom of a moving cilium with a configuration-dependent force used to drive the colloidal bead [18]. The trajectory of this driven bead and its time dependence can mimic those of the biological cilium; in this simpler system it is possible to consider analytical, numerical and experimental studies to work out the possible states of synchronised dynamics between two or more driven objects. In experiments, we can realise this model system by implementing the motile-cilia mimicking trajectories and driving forces via optical tweezers; in simulations, it is instead possible to relate the velocities of the beads to their driving potential via a tensor, without having to solve the Stokes equation numerically [63].

Two model systems have been studied: a "rower", namely a one-dimensional free-phase oscillator, driven by two optical traps that alternatively switch on and off according to the bead position, and a "rotor", in which a bead is driven along a circular trajectory. These model systems, despite being fairly simple to describe, show a very rich range of behaviour.

The earliest experiments explored how a system of rowers is influenced by the thermal noise, discovering that its synchronisation state (between in-phase and anti-phase) depends both by the potential driving the oscillators and by the level of thermal noise [44, 64].

Simulations of bidimensional arrays of rowers show how important the spatial arrangement is for the leading properties of the collective steady state of the system: the placement of rowers influences the direction the oscillators align to [18], the oscillatory modes shown by the system [62], and their stability [65]. These results are important especially in view of better understanding how a ciliated tissue might achieve the high degree of coordination of cilia beating.

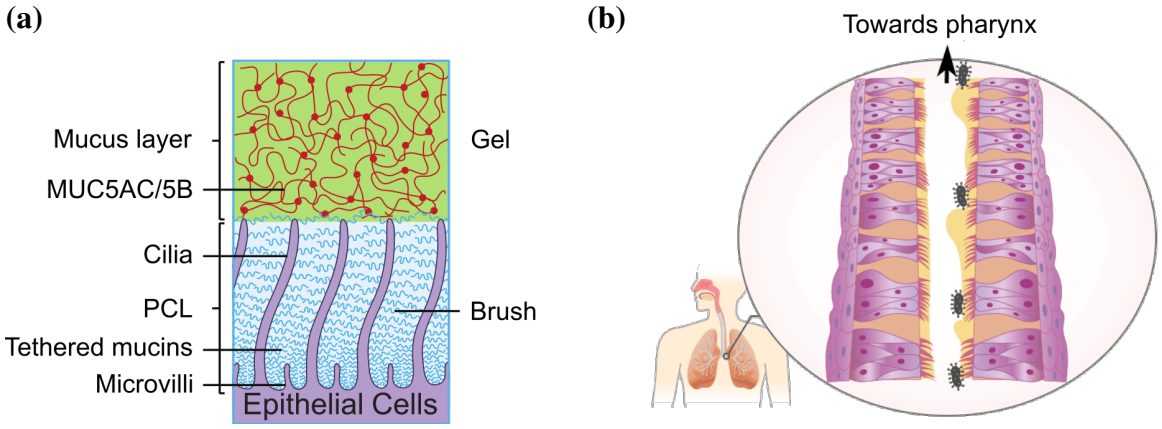

Fig. 1.5 **Mucociliary clearance depends on several mechanisms.** **(a)** Schematic representation of the gel-on-brush hypothesis for the Periciliary Layer: the PCL is occupied by membrane-spanning mucins and large mucopolysaccharides attached to the surface of the cilia. These tethered macromolecules form an extracellular brush with mesh size increasing with the distance from the apical surface of the ciliated cells. Figure taken from [43]. **(b)** Inhaled foreign particles and pathogens are trapped in the mucus layer and propelled upwards along the airways towards the pharynx by the coordinated beating of motile cilia. This defence mechanism is known as mucociliary escalator. Figure adapted from toxtutor.nlm.nih.gov.

One-dimensional arrays of "rotors" have been proven to show transitions between metachronal waves [45] and other collective behaviours, influenced by the presence of no-slip boundaries [60].

In my PhD I have instead been studying a variation on the rotors, by driving the beads along trajectories obtained by coarse-graining the properties of the beat pattern of *in vitro* human airway cilia. In chapter 6 I will discuss how the synchronisation of two cilia-mimicking rotors is influenced by the shape of their trajectory.

1.5 Mucociliary clearance

The lungs and airways are kept pathogen and dust free thanks to the process of mucociliary clearance [66]. The walls of the airways are covered by an epithelium composed by two types of cells: ciliated cells (around 60-80 %) and mucus producing goblet cells. Cilia are immersed in the periciliary layer (PCL), around $6\,\mu\mathrm{m}$ thick. According to a recent study [43], the periciliary layer is occupied by a brush-like structure of macromolecules, namely membrane spanning mucins and tethered mucopolysaccharides, with a mesh size that depends on the distance from the surface of the ciliated cells (Figure 1.5a). The PCL is then topped by a layer of mucus, with a lower osmotic modulus ensuring a stable hydration

level of the PCL (and therefore its constant height) over a range of dehydration states of the airway surface [43]. From a rheological point of view, the mucus is a gel whose viscoelastic properties are strongly dependent on its state of hydration [66].

Mucus is transported out of the airways by mucociliary clearance mechanisms, which rely on the interaction between cilia, the rheologically complex PCL, and the gel-like layer of mucus (Figure 1.5b). In particular, efficient mucus clearance relies upon the cilia beating being aligned in the same direction [67], and coordinated in time and space [53]: in simulations, metachronal coordination was seen to be more efficient both from an energy point of view [17] and in terms of fluid transport [57]. The clearance mechanisms also depends on external parameters: It was observed [68] that ideal conditions for mucociliary clearance are temperature of $37\,^{\circ}\mathrm{C}$ with $100\,\%$ humidity. The velocity of mucus in human airways is not known exactly; measurements using different techniques reported 3.6 to $25\,\mathrm{mm/min}$ for mucus in the trachea, while the only measured value in bronchi is, to our knowledge, $2.4\,\mathrm{mm/min}$ [69].

The ciliated tissue of the airways is studied also from a medical point of view: conditions such as cystic fibrosis (CF) and primary ciliary dyskinesia (PCD) can disrupt the airway clearance mechanism, causing severe consequences such as lung infections, and respiratory insufficiency. Also, the very common asthma is linked to altered airway clearance [70].

1.6 Methods for video analysis of cilia dynamics

Airway cells from human patients can be obtained by biopsy or nose scrape, and then either observed directly or cultured to grow up an *in vitro* epithelium, typically at Air-Liquid Interface. The latter is the most relevant model system for investigating collective dynamics (coordination across many cells) and mucociliary clearance.

The tools that physicians can use to analyse microscopy videos of ciliated cells are limited. A standard is the commercial software Sisson-Ammons Video Analysis (SAVA) [71], which measures the CBF in a user-selected area. The selected area is small (typically $4 \times 4\,\mathrm{px}$), and CBF is measured by Fourier transforming the signal of the pixel intensity over the video. The software thus requires input from the user, which means the need for human resource and possible introduction of bias (e.g. the human eye is naturally drawn towards fast-moving objects). More importantly, and unlike the method presented in the next two chapters, this type of analysis does not probe the spatial correlation in the phase of beating cilia, thus ignores information about metachronal coordination.

This section will provide an overview of how the dynamics of beating cilia have been investigated so far.

1.6.1 Tools for investigating the collective properties of beating cilia

Historically, a few approaches have been explored for quantitative measurements on ciliated cells. Initially, CBF would be measured using a photomultiplier or a photodiode, analysing the changes in the intensity of the light passing through beating cilia [72–74]. With high frame rate cameras it became possible to record high-speed videos of beating cilia, for subsequent analysis. The most straightforward method to measure CBF became therefore to measure the period over a few beating cycles [75]. This was done by visual inspection of the slowed down video. The ability to record and store high-speed microscopy video of beating cilia encouraged development of new algorithms for CBF measurement: Most extract the CBF via FFT analysis of pixel intensity over time, either in user-selected regions of interest [71, 76, 77] or in the entire field of view [78]. This method however only performs a temporal analysis.

An alternative approach is to use an optical flow algorithm: After mapping the movements of objects in between subsequent frames on a vector field, one can obtain the CBF from the displacement signal via FFT [79, 80] or peak detection [81]. Other tools, also based on optical flow, try and extract more than just the CBF from microscopy videos in which cilia are seen from the side: in [82] the beating direction is retrieved, while [83] even attempts an automatic diagnosis of PCD based on the decomposition of ciliary motion as measured in a location chosen by the user into quantitative elemental components. Phase-correlation measurement between physically separated points in the sample are instead at the base of methods aimed to measure the parameters of metachronal waves [53, 84–88].

A very thorough work by Ryser *et al.* [89] showed that reflected light microscopy videos of excised mammalian and aviary ciliated tissues can be analysed to measure both the CBF and the direction and wavelength of metachronal wave. The analysis presented in [89] and employed successively in [90] is very well suited to study samples in which the metachronal coordination is well-developed: First, the sample's CBF is measured via FFT, then the metachronal coordination is characterized using space-time correlation functions and the time evolution of the phase of the recorded signal.

A different approach is however needed when working with ALI cultures, which are the standard condition for culturing *in vitro* human airway epithelial cells. Here cilia are usually not aligned and often only show isolated patches of good metachronal coordination on the scale of a few cells. This is where the method we suggest in chapter 3 can be very powerful, in that it performs simultaneously and in a completely automated fashion both a temporal and spatial analysis on top-view high-speed microscopy videos of a layer of ciliated cells. Our analysis method, expanding on Differential Dynamics Microscopy (DDM), does not require any input from the user, and can not only (a) reliably measure the CBF of a sample, but also (b) quantify to what extent the cilia are synchronized across the field of view,

(c) identify metachronal waves (if present), and (d) measure their wavelength and direction of propagation.

1.6.2 Video analysis at the single cilium scale

On a smaller scale, and using different techniques such as video microscopy [75, 91], micro-Optical Coherence Tomography [92], and Scanning Electron Microscopy [93], encouraging attempts have been made to systematically study the beating pattern of the single cilium, either from human [75, 91, 92] or rabbit airways epithelium [93].

This approach presents many challenges: the arrangement of ciliated cells in the epithelium and the very high number of cilia per cell make it extremely difficult to image clearly the single cilium for several beating cycles. These limitations are not present when studying model organisms, such as *Chlamydomonas reinhardtii*, *Volvox carteri*, and sperm cells: The low number of flagella and their spatial arrangement allow for an almost automatic tracking of the flagellar waveform over time [21, 25, 41, 47, 94]. Since the data so obtained are usually of high temporal and spatial resolution, they can be used to try and understand how the interplay between the internal structure of the flagellum and the action of the molecular motors dictates the flagellar waveform [25, 42, 95].

While the study of the dynamics in model organisms with few cilia and flagella has benefited from this type of almost automatic tracking, the same can't be said when it comes to cells with many cilia. Some of the imaging techniques employed historically to study multiciliated cells present strong limitations. SEM for example can only image a static system, so it is necessary to very quickly freeze the ciliated epithelium. If the freezing process is successful, the cilia will be stuck "mid beat" and it is possible to obtain a very detailed snapshot of their configuration [93, 96]. Micro-Optical Coherence Tomography on the other hand can image live, moving cilia, even in *in vivo* systems, but is limited in terms of spatial resolution [92, 97]. High speed video microscopy yields recordings of moving cilia with good spatial and temporal resolution. However so far the assessment of the ciliary beat pattern have mostly been either qualitative, due to the difficulty of consistently tracking cilia in microscopy videos [98], or limited in the quantities measured [99]. Our own successful approach to the in-depth probing of the beat pattern at the single-cilium level, and the results achieved by applying it to study cilia from donors both healthy and affected by PCD, are described in chapter 5.

1.7 Pressing questions about cilia motility and coordination

There are several open questions regarding cilia motility, and while as previously mentioned they make for fascinating subjects of study for biologists and physicists, it is the medical community that would stand to gain the most if they were answered. Cystic Fibrosis is, after all, one of the most common genetic diseases (more precisely, it is the most common lethal genetic disease in white population [100]). During my PhD work I have touched on a few main questions, that feature in this manuscript.

First, is Ciliary Beat Frequency, which is the parameter most used so far, a complete and comprehensive indicator for cilia motility? Or should scientists and medical doctors be looking at other physical quantities in order to fully characterise the behaviour of cilia?

A very closely related question is whether the degree of coordination in the beating across a ciliated epithelium is an important feature, how it affects mucociliary clearance, and, if it is an important parameter, why it is not currently exploited.

Diagnosing ciliopathies relies on a series of steps that often involve several tests and Transmission Electron Microscope (TEM) imaging of samples from ciliated epithelia. This, as it will be explained better in section 5.2, is often not enough. In the case of Primary Ciliary Dyskinesia, for example, the assessment via high speed video microscopy of the ciliary beat pattern by highly trained clinicians has recently being strongly advised by the European Respiratory Society [101]. In this context it would be extremely useful to understand if it is possible to develop a software for automatic diagnosis of ciliopathies, based on the analysis of high speed microscopy videos. As an alternative, it would at least be very helpful if it were possible to devise an analysis software for high speed microscopy videos that provided clinicians with precise quantitative measurements they could employ to aid their diagnosis.

A final more fundamental question addressed in this manuscript concerns how the beating pattern can affect synchronisation, and through it affect the large scale coordination and the mucociliary clearance mechanism.

As mentioned above, finding an answer to these open questions would bring several benefits to the medical and pharmaceutical communities. A better understanding of how cilia work and how they interact to synchronise, both at a small (few microns) and a larger scale (hundreds of microns), would be advantageous in terms of drug designing. The development of alternative screening methods would make the drugs development process less expensive. And more importantly, the availability of new and reliable tools to supply medical doctors with quantitative measurements would lead to easier, cheaper, more accurate, and more timely diagnoses.

Chapter 2

Differential Dynamic Microscopy

2.1 Scattering experiments with a microscope

My work builds on Differential Dynamic Microscopy (DDM), which is introduced in this chapter. DDM is an extremely powerful video analysis technique invented in 2008 by Roberto Cerbino and Veronique Trappe [102].

DDM effectively bridges the gap between scattering and microscopy, as it allows for the characterisation of the dynamics of scatterers in the field of view even if they can not be resolved individually [103]. Ultimately it allows, via the analysis of a standard white-light microscopy video, to access the same information usually yielded by Dynamic Light Scattering (DLS) [102].

In section 2.2 we will briefly go over the theoretical foundation of DDM, while section 2.3.1 contains a review of the studies that have recently been undertaken exploiting the power of DDM.

2.2 What is DDM

DDM is a near-field (or deep-Fresnel) technique that relies on the Fourier analysis of difference images to retrieve information about dynamics in a sample [102]. As mentioned above, DDM delivers, in some simple conditions such as colloidal particle diffusion, the same information usually accessed by DLS. This is possible because, as derived in [104, 105], in near-field condition the light intensity measured by the microscope gives direct access to the real part of the scattering field (Figure 2.1).

In a typical imaging experiment a microscope video is acquired via a camera. The raw input data are thus time-lapse images $F(\mathbf{r}, t)$, where $\mathbf{r}$ is the position vector in the image

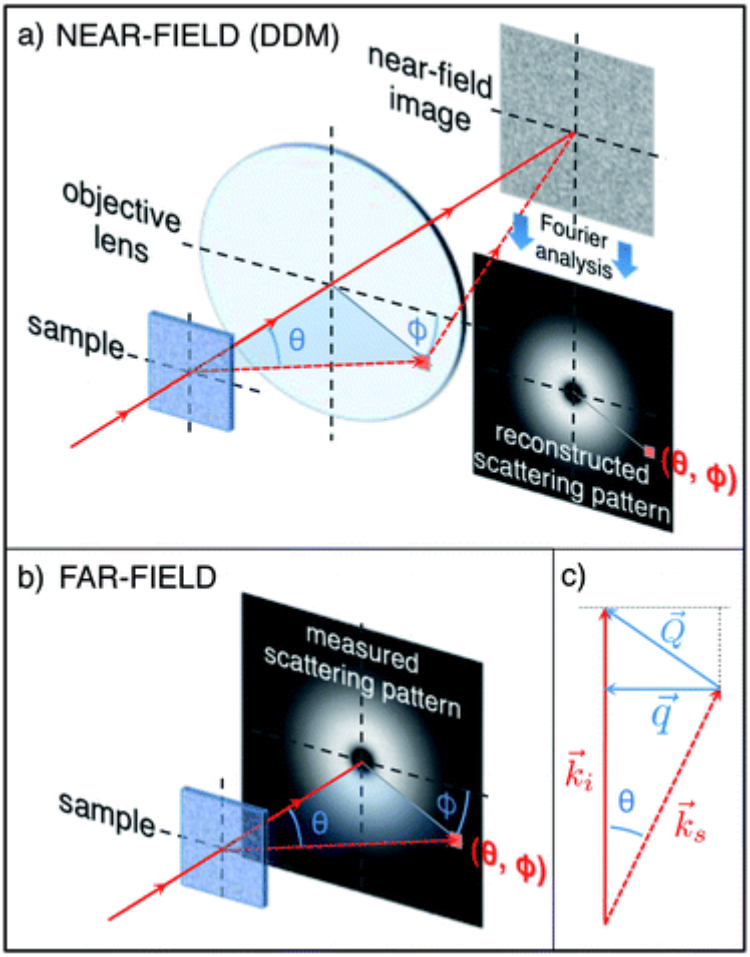

Fig. 2.1 **DDM is a scattering experiment.** **(a)** In a DDM experiment the sample scatters the incident light at various angles. The scattering light is then collected by the objective lens and impressed on the camera sensor. The Fourier analysis of the images of the samples can access information usually investigated through **(b)** scattering experiments in the far field, as the generic scattered ray with polar angle θ and azimuthal angle ϕ is collected by the objective lens and contributes to the image. Two-dimensional Fourier analysis can isolate the contribution of each scattering wave. **(c)** It is worth noting that the 2D scattering vector $\mathbf{q}$ is the projection of the 3D scattering vector $\mathbf{Q}$. Figure taken from [104].

plane. Let $F(\mathbf{r}, t_0)$, the frame recorded at time t_0, be the reference image, and $D(\mathbf{r}, t_0, \tau)$ the algebraic difference between the reference frame and the frame recorded a time interval τ ("lag time") after t_0:

$$D(\mathbf{r}, t_0, \tau) = F(\mathbf{r}, t_0) - F(\mathbf{r}, t_0 + \tau). \tag{2.1}$$

Let then $D(\mathbf{q}, t_0, \tau)$ be the two-dimensional Fourier Transform of the differential image $D(\mathbf{r}, t_0, \tau)$. Assuming a stationary and ergodic sample (i.e. the dynamics do not depend on the reference time t_0) it is possible to average over all difference images with the same time τ,

obtaining the Image Structure Function

$$I(\mathbf{q},\tau) = \left\langle \left| D(\mathbf{q}, t_0, \tau) \right|^2 \right\rangle_{t_0}. \tag{2.2}$$

If the sample is also isotropic, then the Image Structure Function will have a circular symmetry in $\mathbf{q}$. It is therefore possible to perform an azimuthal average: The Image Structure Function $I(q,\tau)$ now depends only on the magnitude of the scattering vector ($q = \sqrt{q_x^2 + q_y^2}$) and on the lag time τ. It is worth noting that the 2D scattering vector $\mathbf{q}$ is the projection of the 3D scattering vector $\mathbf{Q}$ (Figure 2.1c).

Information about the system dynamics is then obtained by looking at how the amplitude of the Fourier modes (related to q) changes with τ, which is the time separation between the two subtracted images. More specifically, the Image Structure Function is fitted with the theoretical expression

$$I(q,\tau) = A(q)\left[1 - f(q,\tau)\right] + B(q), \tag{2.3}$$

where $B(q)$ is a background term that takes into account detection noise, and $A(q)$ is the product between the intensity scattered by the sample and a transfer function that depends on the microscope. $A(q)$ and $B(q)$, as it will be shown later, do not need to be known, and can be retrieved as parameters of the fit. The system dynamics are contained in $f(q,\tau)$, which has been shown [106, 107] to be none other than the Intermediate Scattering Function usually measured in scattering experiments, which is in turn the Fourier transform of the Van Hove function $G(\mathbf{r},\tau)$ [108]. It is worth noting that because of the very definition of $f(q,\tau)$ a decay of the latter to zero ($f(q,\tau \to \infty) \to 0$) reflects the fact that sample configurations separated by a progressively larger lag time τ become more decorrelated due to motion in the imaged sample [109].

As a side note, exploiting the linearity of the Fourier transform, one can rearrange eq. (2.2) as

$$I(\mathbf{q},\tau) = \left\langle \left| \mathcal{F}\left(F(\mathbf{r}, t_0)\right) - \mathcal{F}\left(F(\mathbf{r}, t_0+\tau)\right) \right|^2 \right\rangle_{t_0}, \tag{2.4}$$

where $\mathcal{F}$ denotes the Fourier transform. This is computationally advantageous: In a video with N frames, one can compute only N Fourier Transforms and store them in the memory to be re-used as needed, whereas using eq. (2.2) the number of FFTs to computed can be as high as $N(N-1)$.

2.3 DDM is a general technique apt for several applications

Since it was invented in 2008 DDM proved to be a very general and powerful tool, useful in probing the dynamics of several systems, both in Soft Matter and in Biological set-ups [110]. This section reports a series of examples of studies in which DDM has been fruitfully employed, as well as a comparison against particle tracking and dynamic light scattering.

2.3.1 DDM is being employed to study a variety of different systems

In their pioneer work, Cerbino and Trappe [102] demonstrated the validity of DDM by analysing the q-dependent dynamics of colloidal dispersions, finding good agreement with what was theoretically expected for Brownian particles in a viscous medium. Ferri *et al.* [105] subsequently used DDM to study the kinetics of colloidal fractal aggregation, measuring the radius of colloidal aggregates over time and extracting their fractal dimension.

The first time DDM was employed on active (living) samples was in 2011, when Wilson *et al.* [106] employed it to measure the swimming speed distribution and motile cell fraction in *Escherichia coli* suspension. The same group published a second paper one year later [109], in which also the dynamics of *Chlamydomonas* was investigated.

All the studies cited so far investigated isotropic dynamics, but in 2012 Reufer *et al.* tuned the DDM algorithm to probe the dynamics of anisotropic colloidal samples, and tested the improved technique on a dilute aqueous dispersion of anisotropic magnetic particles aligned in a magnetic field. The group measured the diffusion coefficient along the two main axis (parallel and perpendicular to the field) and also extracted the orientational order parameter of the system [111].

While DDM is very often used as a particle sizing tool in systems where the viscosity of the medium is known, if the known variable is instead the particle size then DDM turns into a viscometry tool. This was exploited in [112] to measure the viscosity of supercooled water by probing the diffusivity of tracer polystyrene particles. While the experiment performed for this work could have been done via particle tracking, the advantages of DDM proved to be the key in exploring very low ranges of temperature: By using many small particles DDM allows for a statistically significant and user-independent characterisation of the dynamics in an experiment shorter than the time needed for the water to solidify.

Two key features of DDM, especially as opposed to DLS, are its insensitivity to static contributions to the image and the contemporaneous access to multiple wave vectors $\mathbf{q} = (q_x, q_y)$. These features were fundamental in the application of DDM to probe the dynamics of

nanoscale diffusers in a dense array of nanoposts [113]: As in DDM the images are subtracted from one another, the static contribution of the nanoposts cancels out allowing the dynamics of the diffusers to be fully captured, and to be characterised as isotropic despite the confinement conditions.

DDM has also been shown to be able to investigate dense, opaque, fluorescent samples of micron-sized object [114] exploiting confocal microscopy. Variations of DDM using more than one contrast mechanism have been developed to study the dynamics of cytoskeletal filamentous actin and endogenous vesicles within a *Drosophila* oocyte [115], and the diffusivity of a population of small particles in an environment crowded by mobile obstacles [116]. The dynamics of two populations of different size can instead be simultaneously probed by "standard" DDM [117].

A time-resolved version of the DDM algorithm, implemented by not taking the ensemble average in eq. (2.2), allowed the characterisation of the complex dynamics in the kinetic arrest of a colloidal gel undergoing spinodal decomposition [118].

Modifying the experimental DDM set-up (a microscope) with two aptly oriented polarisers allows to investigate the dynamics of nematic liquid crystals [104], and to simultaneously characterise the translational and rotational diffusivity of optically anisotropic particles [119].

Recently, Wulstein *et al.* suggested engineering the point spread function (PSF) of the microscope to extend the reach of DDM. In their work they explore two main ideas: using an astigmatic PSF in order to reduce the size of the imaged region without losing information at low wave-vectors, and using a saddle-point PSF to increase the sensitivity of DDM to displacements of scatterers in the axial direction [120].

Finally, Edera *et al.* demonstrated that it is possible to perform microrheology experiments using DDM, and thus to characterise the mechanical moduli of soft materials in a simple, calibration-free manner [121].

2.3.2 Advantages (and disadvantages) of DDM compared to DLS and particle tracking

DDM is an optical technique that bridges the gap between microscopy and light scattering experiments, and have several advantages over either of them [110].

Compared to dynamic light scattering, DDM shows several strong points. First, it simultaneously probes multiple q-vectors, allowing to collect data with very good statistics while reducing the overall length of the experiment. DDM also explores a range of wave-vectors that is usually not accessible by DLS: Since low ranges of wave-vectors correspond in DLS to very small angles off the direction of the incident light, detection is usually perturbed

by stray light from imperfections in the optical path. DDM on the other hand is robust to such perturbation, as they would only give a static contribution that cancels out when taking the difference between frames. This insensitivity to static contributions also makes DDM especially useful in set-ups with low-quality optics, or where the optical elements are less than perfectly cleaned. On the other hand any moving imperfection or contamination will give its contribution - hard or impossible to decouple from the sample's signal - to the Image Structure Function. In non-homogeneous samples DDM can probe different regions of the field of view, yielding a space-resolved information that is very challenging and time consuming to achieve in DLS experiments. Of course DDM also shows some limitations compared to scattering experiments, in particular when it comes to the sensor used: camera detectors are still outperformed by photomultiplier tubes and avalanche photodiodes when it comes to speed and sensitivity.

The advantages of DDM over particle tracking (PT) are different: In a typical tracking experiment, the user needs to segment the image and track the desired features across frames (recognise who's who in consecutive frames). This usually requires the fine tuning of several parameters: the minimum and maximum size for a feature to be of interest, the allowed amount of movement between frames, and so on. DDM has no need for segmentation, and requires no image pre-processing, which can in fact be very detrimental, in that filters and operations of simple interpretation in real space play havoc in Fourier space [103]. It is worth stressing that the single advantage that makes DDM a much better candidate than particle tracking for automation is that there is no user-defined parameter: only a family of fitting functions needs to be decided for the analysis of a sample. DDM suffers of course from some drawbacks against particle tracking: PT offers a more complete characterisation of the population of tracers, as trajectories can be post-processed, filtered, sorted, and binned, while in DDM the user can only access probability distributions (e.g. of size or velocity) by inverting the intermediate scattering function. This makes DDM very susceptible to moving impurities, as their contribution to the signal can be impossible to remove *a posteriori*.

The ability of DDM to probe the dynamics of crowded, weakly scattering, un-trackable objects is what makes it a perfect candidate for the analysis of motile cilia, as it will be demonstrated in the next chapter. I will also show an extension of DDM, which I called multiDDM, which extends DDM in a powerful new direction for measuring spatial coherence of the dynamics.

In order to successfully apply DDM to the investigation of the dynamics of motile cilia, we had to overcome one of its limitations. In general, DDM is at its most powerful when combined with a model for the Intermediate Scattering Function. Calculating *a priori* an analytical form for the Intermediate Scattering Function has been done now on relatively

simple systems [102, 106, 109, 117], but it becomes a fairly complicated task on more complex systems. Without an analytical prediction for the Intermediate Scattering Function, it becomes potentially difficult to interpret the Image Structure Function yielded by DDM. We overcome this particular problem by fitting the Image Structure Function with an empirical function. This allows us to obtain meaningful parameters that describe the dynamics of the sample, as the next chapter will show in more detail.

Chapter 3

DDM and multiDDM to characterise ciliated epithelia

3.1 A novel approach to the study of ciliated epithelia

This chapter describes a new approach for user-independent characterisation of cilia collective dynamics.

As reported in detail in chapter 2, the technique of Differential Dynamic Microscopy (DDM) was invented fairly recently to characterise dynamics in colloidal suspensions [102, 103] and relies on Fourier analysis of difference images. Here we build on this approach, developing what might be called a "multiscale-DDM" - multiDDM for short.

The very first goal of our technique is to obtain an unbiased measurement of the Ciliary Beat Frequency, which can be compared to previous analysis approaches (section 3.3). A discussion on how to perform a more thorough analysis on the sample in order to retrieve additional parameters will be carried in sections 3.4 and 3.5, and in Appendices A and B.

MultiDDM offers significant improvements over the most established approaches, based on single-point FFT, for the analysis of *in vitro* ciliated cells: First, it requires no user input, thus removing the most important source of bias and reducing significantly the time required for analysis; second, as will be detailed in the following sections, it is a technique that intrinsically extracts physical quantities averaged over the sample, improving statistics over single-point techniques (it can be easily tuned to maintain the spatial information, if this is desired). However the most notable advantage of multiDDM over point-FFT approaches is that DDM measures various physical quantities of the cilia dynamics that might be related to diseases, thus providing doctors and researchers with full information for diagnostics.

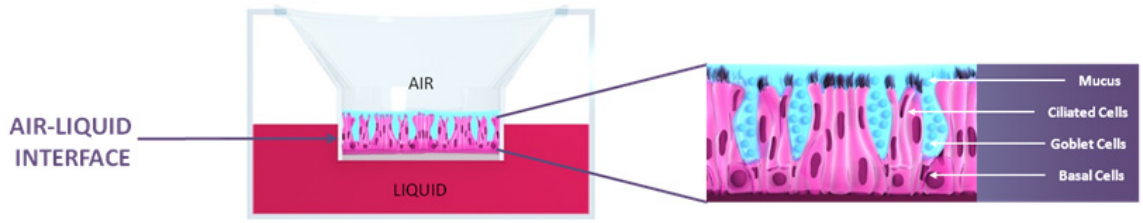

Fig. 3.1 **Sketch of *in vitro* samples.** Cartoon showing the arrangement of the commercially available samples purchased from Epithelix. The reconstructed airway epithelium is composed of basal cells, goblet cells, and ciliated cells, and sits on a semipermeable membrane at the bottom of a plastic insert. The epithelium is kept at Air-Liquid Interface by placing the plastic insert in a 24-well plate: the semipermeable membrane allows the uptake of nutrients from the basal medium, but the mucus layer remains exposed to the atmosphere. The drawing, taken from www.epithelix.com, is not to scale: in real life, the cilia are about $7\,\mu\mathrm{m}$ long, while the diameter of the membrane supporting the ciliated epithelium is $6.5\,\mathrm{mm}$.

3.2 Methods of cell culture and imaging

Data presented in this chapter was either collected in-house by me on commercial ALI samples, following 3.2.1, or by Dr Cedar J. Fowler for his PhD research on commercial cells grown in-house, following methods described in section 3.2.2.

3.2.1 In-house imaging of commercially available assays

The videos analysed for sections 3.3.3 and 3.4 were obtained from assays purchased from a commercial company and imaged in-house as follows. A healthy Human Airway Epithelium reconstituted *in vitro* (MucilAir™, see Figure 3.1) was purchased from Epithelix (Epithelix Sàrl, Geneva, Switzerland) and maintained following the protocol provided by the company. The layer of ciliated cells (much more densely ciliated than was possible via the method of section 3.2.2) was then imaged in bright field on a Nikon Ti-E inverted microscope (Figure 3.2) equipped with a $40\times$ dry Nikon objective (NA 0.95). High speed videos were then recorded using a CMOS camera (model No. GS3-U3-23S6M-C; Point Grey Research/FLIR Integrated Imaging Solutions (Machine Vision), Richmond, British Columbia, Canada) connected to a LINUX workstation running a custom video grabbing software developed in house. The videos have a resolution of $1024\,\mathrm{px} \times 1024\,\mathrm{px}$ and $150\,\mathrm{fps}$ frame rate. This magnification yields a $0.146\,\mu\mathrm{m/px}$ ratio and, together with the frame size $L = 1024\,\mathrm{px}$, a spatial sampling frequency $q_{min} = 0.042\,\mu\mathrm{m}^{-1}$.

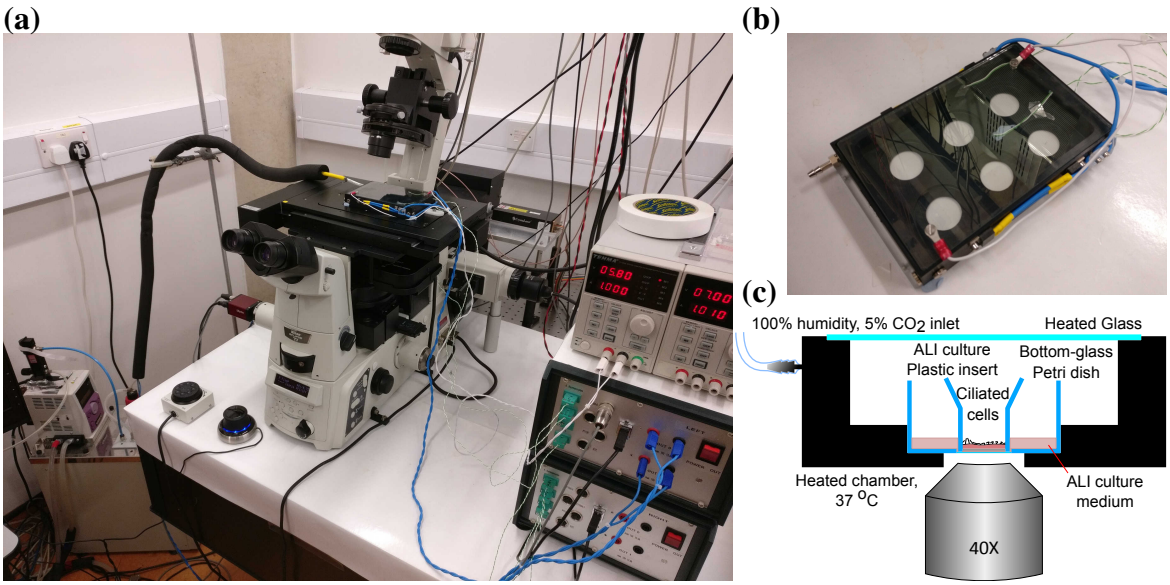

Fig. 3.2 **Imaging chamber.** Cells are imaged on a Nikon Ti-E inverted microscope **(a)** while being kept in ideal conditions throughout the experiments thanks to a custom imaging chamber designed by Dr Jurij Kotar **(b, c)**. Samples are kept at $37\,^{\circ}\mathrm{C}$ and in a controlled atmosphere with $100\,\%$ humidity and $5\%\,\mathrm{CO}_2$.

Samples of ciliated cells were kept in ideal conditions ($37\,^{\circ}\mathrm{C}$ temperature, $5\%\,\mathrm{CO}_2$, $100\,\%$ humidity) during the experiments, thanks to a custom-made imaging chamber designed and manufactured by Dr Jurij Kotar (Figure 3.2).

3.2.2 Culture of ciliated cells at the air-liquid interface and their imaging

The videos analysed while developing the analysis tools and featured in section 3.3.2 were collected by Dr Cedar J. Fowler during his PhD as follows.

Commercially available Normal Human Bronchial Epithelial (NHBE) cells provided by Lonza (Lonza, cat# CC-2540, Walkersville, MD) were grown at the air-liquid interface (ALI) following a protocol issued by the selling company. After defrosting, 9.5×10^4 cells were seeded into $6.5\,\mathrm{mm}$ collagen-coated polyester Transwell inserts (12-well with a pore size of $0.4\,\mu\mathrm{m}$, Corning Inc., Lowell, MA) with basal ALI media (Lonza, cat # B-ALI-BulletKit, Walkersville, MD). When confluent, the transwells were shifted to ALI culture by removing the apical media and maintaining $800\,\mu\mathrm{l}$ ALI media in the basal compartment. The media were exchanged every other day. Mucociliary differentiation and cilia beating occurred within 4 weeks.

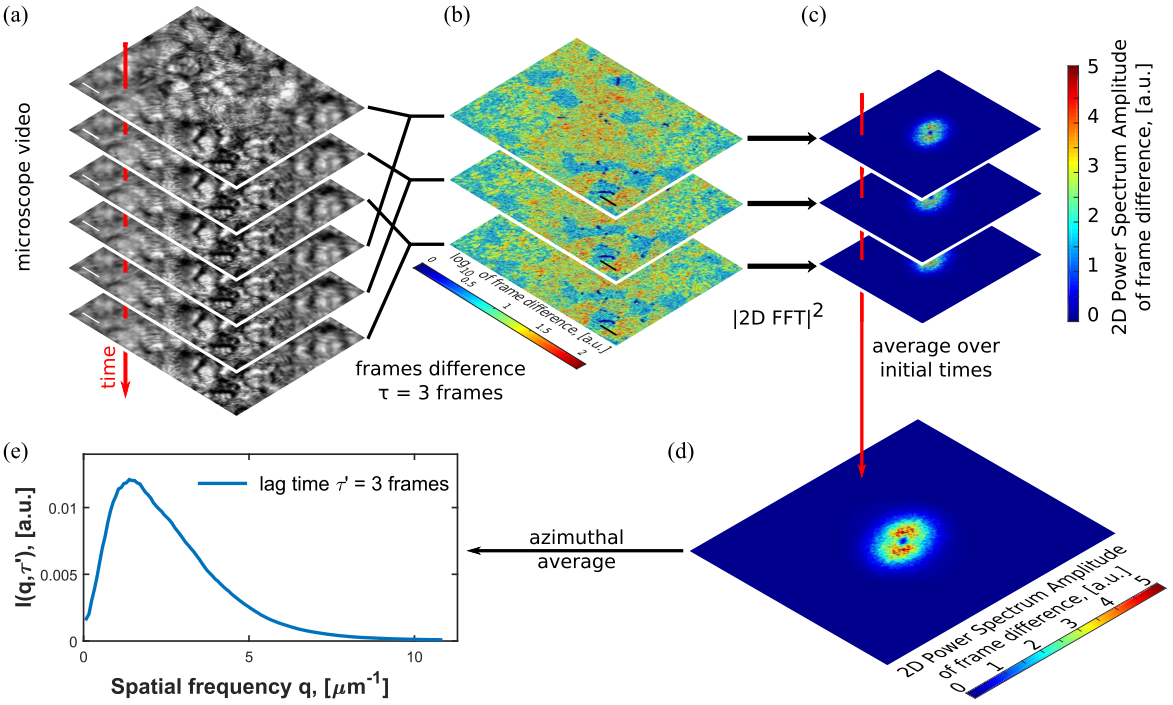

Fig. 3.3 **Differential Dynamic Microscopy (DDM) allows a complete characterisation of collective dynamics in ciliated cells.** The technique relies on the Fourier analysis of **(a)** time-lapsed, bright field microscopy images. **(b)** Images separated by a time interval ("lag time") τ are subtracted, and **(c)** the absolute value of the two-dimensional Fast Fourier Transform (FFT) of the differential images is then computed. **(d)** Assuming a stationary and ergodic sample we average over all the Fourier transforms of the differential images with given τ. **(e)** If sample dynamics is isotropic, then the two-dimensional power spectrum can be azimuthally averaged yielding a one-dimensional power spectrum.

NHBE cells were imaged in bright field using a $63\times$ glycerol objective with a $1.5\times$ internal magnification on a Leica DM IRBE inverted microscope (Leica Microsystems, Inc., Bannockburn, IL) on a vibration dampened table. An area scan high-speed monochromatic digital video camera (model A602f-2, Basler AG, Ahrensburg, Germany) was used for image and video acquisition, recording a $\sim 2.56\,\mathrm{s}$ video with a resolution of $720\,\mathrm{px} \times 480\,\mathrm{px}$ and $100\,\mathrm{fps}$ frame rate. At this $94.5\times$ magnification $1\,\mathrm{px} = 0.161\,\mu\mathrm{m}$. The inverse pixel size $k = 6.2\,\mu\mathrm{m}^{-1}$ and the frame size $L = 480\,\mathrm{px}$ (the algorithm was coded to work on square images, therefore L is the size of the shortest side of the image) define the spatial sampling frequency $q_{min} = 2\pi k/L = 0.081\,\mu\mathrm{m}^{-1}$.

All imaging was done at $37\,^{\circ}\mathrm{C}$ in ALI media. At each time point of the experiment, approximately 40 fields of view (FOV) of each sample were imaged. All samples were kept at $37\,^{\circ}\mathrm{C}$ and $5\%\ \mathrm{CO_2}$ and in ALI media throughout the experiment and imaging.

3.3 DDM on videos of ciliated cells

Figure 3.3 shows all steps of DDM analysis. As outlined above, the first step is to take difference images between a reference frame $F(\mathbf{r}, t_0)$ and a frame recorded a time interval τ later. 2D power spectra of differential images are then calculated. All 2D power spectra obtained by the difference of images separated by the same value of τ are averaged, as the system dynamics is assumed to be stationary.

The next step is the azimuthal average $q = \sqrt{q_x^2 + q_y^2}$, possible when the 2D power spectra show radial symmetry (i.e. the system dynamics is isotropic). This is clearly not the general case in samples with planar cell polarity and metachronal waves. Nevertheless, *in vitro* cultures often lack directionality. Here, the anisotropy is disregarded as a first approximation, as the primary goal of the analysis outlined in this section is just the assessment of the Ciliary Beat Frequency. An example of radially averaged power spectra $I(q, \tau')$ is shown in Figure 3.3e. As the Image Structure Function $I(q, \tau)$ is a function of the two variables spatial frequency q and lag time τ, to indicate a cross-section of $I(q, \tau)$ at a fixed value of either variable, such variable will be primed: $I(q', \tau)$ is a cross-section at fixed spatial frequency, while $I(q, \tau')$ a cross-section at fixed lag time.

3.3.1 Interpreting motile cilia DDM results

System dynamics are accessible in the Image Structure Function by studying how the amplitude of the Fourier modes changes with τ. The data in each $I(q', \tau)$ (some examples shown in Figure 3.4b) behave like a damped oscillator, and can therefore be fitted with an empirical function

$$I(q', \tau) = A\left[1 - \exp(\cos(2\pi\nu\tau))\right]\exp(-\tau/\tau_c) + B. \tag{3.1}$$

The meaning of the fitting parameters A and B has already been discussed in section 2.2, but for this section of particular interest are ν and τ_c.

The parameter ν is the frequency of the oscillations of the amplitude of the Fourier component q', and this is the Ciliary Beat Frequency of the sample. As shown in Figure 3.4, such frequency does not depend on the spatial frequency q. This is not (yet) a robust estimate of CBF, as in many videos the DDM signal was dominated by some high contrast impurity that would either move randomly or oscillate with a different frequency. The solution to this issue is addressed in section 3.3.2.

The other interesting parameter is the decay time τ_c, as this is related to the coherence of cilia movement. It is sensible to expect that two factors might contribute to the decay time τ_c: First, a spatial factor, related to how different cilia (or cells) can beat at slightly different

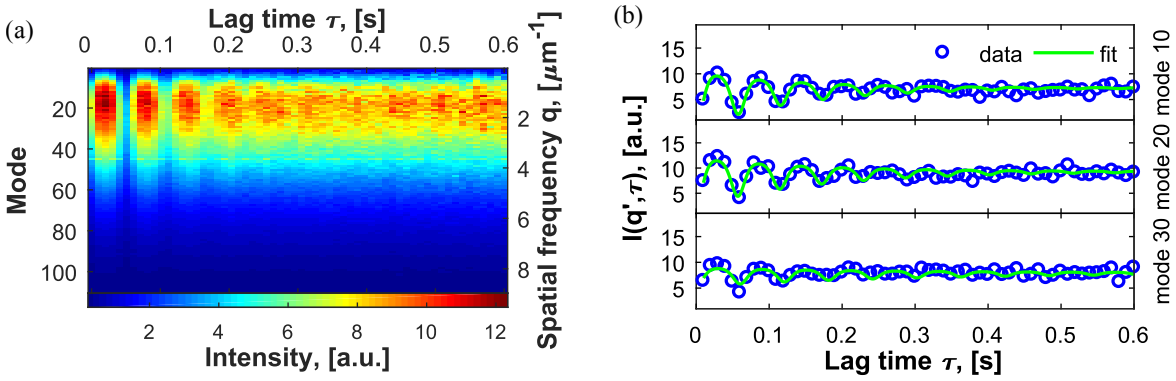

Fig. 3.4 **DDM measures the system dynamics.** A one-dimensional power spectrum can be computed for all possible values of the lag time τ by repeating the steps described in Figure 3.3, thus yielding **(a)** the Image Structure Function $I(q, \tau)$. **(b)** The system dynamics can then be investigated through the dependence of the amplitude of each Fourier mode on the lag time τ. In the case of a layer of ciliated cells, the Fourier mode amplitudes undergo damped oscillations, and are fitted with a suitable functions (see eq. (3.1)). Only three Fourier modes are shown in **(b)** as an example.

frequencies, therefore not being perfectly phase-locked. This is especially due to the fact that in most of the videos in the dataset the cilia coverage of the sample surface was patchy, with only small clumps of ciliated cells surrounded by non-ciliated cells. In the hypothesis that the synchronisation among cilia comes from hydrodynamic coupling (which decays as the reciprocal of the separation in the bulk, and as the reciprocal of the separation cubed close to a wall [32]), we expect to see cilia extruding from the same cell to be better synchronized than cilia belonging to different cells because of a distance effect. Second, the beating cycle of one cilium might be not always identical to itself (at least because of thermal noise influence on molecular motors), and this might affect the decay time as well. This concept, which is analysed in more detail in Appendix A using simulated data, is the basis of the new method we propose in section 3.4.

3.3.2 Spatially resolved DDM can provide a more robust estimate of CBF

In the experimental dataset described here, approximately 40 videos are analysed. Unfortunately in several of them there is some dirt or some other high contrast feature moving in the field of view, making the results of full-field DDM unreliable. To work around this issue, the $720\,\mathrm{px} \times 480\,\mathrm{px}$ imaged region is divided into square "boxes" of $80\,\mathrm{px}$ side, which is roughly the size of a cell. The DDM algorithm is then run only on the boxes with the most activity. To select these regions, first we create a "movement map" of the whole movie: this is

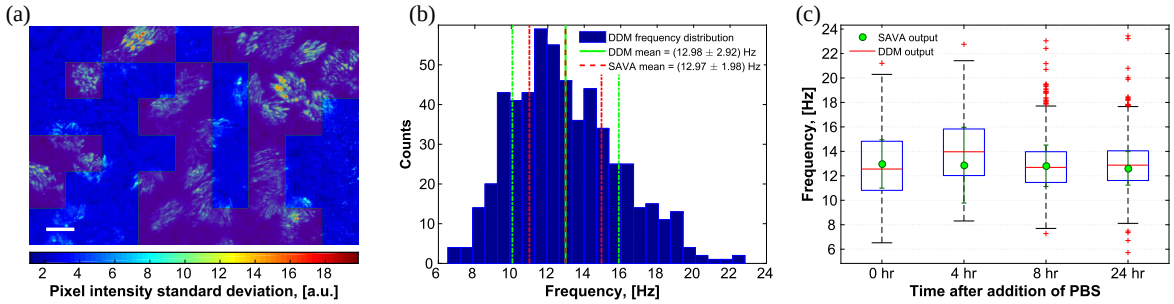

Fig. 3.5 **DDM can yield an accurate and robust measurement of ciliary beat frequency.** While the analysis of the entire field of view with the algorithm described in section 3.3.1 yields an accurate estimate of the average ciliary beat frequency, such measurement can be affected by stray objects (e.g. cell debris) drifting or being transported into the field of view. **(a)** Robustness of the analysis can be improved by dividing the field of view into small square boxes of approximately the size of a cell, and running the DDM algorithm only on the boxes with the most activity (selected by thresholding the standard deviation of pixel intensity over time), yielding one CBF value for each box. Scale bar is $10\,\mu\mathrm{m}$. **(b)** A distribution of CBF arises running DDM (exploiting the division of the field of view into small boxes) on 44 videos, sampling different regions of the same assay. The mean and standard deviation are shown in green, and compared with CBF values obtained by the commercial software SAVA on the same set of videos. **(c)** CBF measurements of a sample of ciliated cells, at increasing times after addition of Phosphate-buffered saline. Each box shows median (central mark), 25$^{\text{th}}$ and 75$^{\text{th}}$ percentile (box) and outliers of the distribution of CBF values, extracted from approximately 40 videos on the same assay. The same set of videos was analysed with the SAVA software (green circles), showing good agreement with DDM results.

a matrix of the same size of any of the frames of the original video, and each entry contains the standard deviation over time of the grey level of the corresponding pixels in the original video, following $\sigma^{video}(\mathbf{r}) = \sqrt{\frac{1}{N-1}\sum_t \left(F(\mathbf{r},t) - \langle F(\mathbf{r},t)\rangle_t\right)^2}$, where N is the number of frames and $F(\mathbf{r},t)$ is the frame recorded at time t. We then divide the field of view into boxes of the desired size, and coarse-grain the movement map by summing all the entries of it that lie within the same box. A threshold is set on the coarse-grained movement map via Otsu's method [122]. DDM is then performed on the boxes whose "movement level" is over the threshold (Figure 3.5a).

For each box the Image Structure Function $I(q,\tau)$ is obtained, and the τ-dependence of the amplitudes of the Fourier modes is investigated by fitting $I(q',\tau)$ curves with eq. (3.1). This yields a value of the frequency ν_q for each value of q, the average of which, $\langle \nu_q \rangle_q$, is the estimated CBF for the box. For each sample one value of CBF for each analysed box of each video is measured, building a distribution as shown in Figure 3.5b. The mean value of the distribution is the final (and robust) estimate of CBF in the sample, its uncertainty being the spread of the distribution. It is worth stressing that the error on CBF is not the uncertainty

with which the DDM can assess a frequency, but it comes from the fact that across the sample there is a distribution of cells with different CBF, and all beating cells have been measured.

Dividing the field of view into boxes proved to be an effective way to minimise the effect of debris on the measurements: When a high contrast feature moves across a region analysed with DDM it gives its own contribution, difficult to separate from the cilia's, to the Image Structure Function. This effect is maximum when taking DDM on the entire field of view, as the dirt will affect the only box of the video and for many frames. When dividing the field of view into many boxes instead only the boxes on the trajectory of the debris will be affected and for fewer frames. In this way we do not need to exclude the boxes crossed by debris from the analysis, but rather we minimise the effect of this high contrast features on the analysis.

A by-product of using an - albeit rudimentary - motion-detection algorithm is the ability of providing the user with a percentage of regions showing movement. This can be useful in comparing, for example, different culture methods or stages of development.

Comparisons between CBF as obtained through DDM and by using the commercial software SAVA are shown both in Figure 3.5b for a single set of 44 videos taken on the same assay in a limited amount of time, and in Figure 3.5c where the evolution of CBF in a sample is followed in time after Phosphate-buffered Saline (PBS) was added to the sample. The results show very good agreement between DDM and SAVA measurements of CBF. It is worth stressing that CBF measurements with DDM are completely automatic, requiring no user input that might induce a bias towards faster beating (high frequencies). Keeping in mind that DDM can also extract other physical quantities (as described later), this is a serious improvement on the existing approaches for analysing *in vitro* samples of ciliated cells.

3.3.3 DDM-based detection of metachronal waves

Arguably the most prominent feature of a ciliated tissue is that phase-locking among beating cilia yields a metachronal wave. It is thus essential that DDM can provide insight into the metachronal wave for it to be deemed suitable for the analysis of ciliated tissues. Unfortunately almost the entirety of *in vitro* samples analysed in this chapter do not display long range metachronal waves (as discussed in section 3.3.1, instead of a continuous carpet of cilia the samples described in section 3.2.2 are constituted of small regions of only few ciliated cells). We believe that a possible reason for the lack of metachronal waves may be the absence (unlike the *in vivo* case) of flow at the moment of cilia development, and the low density of ciliated cells. Metachronal waves were therefore studied on the commercially available cultures described in section 3.2.1, where despite the absence of flow during ciliary development the higher density of ciliated cells makes it possible to have some degree of long range coordination in the ciliary beat (Video B.1 in the supplementary materials).

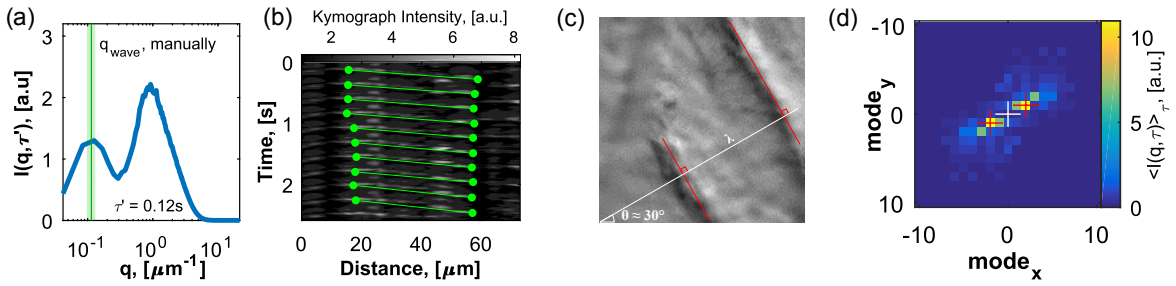

Fig. 3.6 **DDM can detect a metachronal wave and measure its wavelength.** A metachronal wave is a travelling wave with wavelength λ: it shows up as a sharp peak in the Image Structure Function, at $q_{wave} = 2\pi/\lambda$. **(a)** A section of the Image Structure Function at fixed lag time τ', showing the sharp peak at low q signature of a metachronal wave. The green line shows a direct measurement of q_{wave}, and the shaded region its standard deviation. **(b)** The high speed video analysed in **(a)** (Video B.1) was processed by taking the differences between subsequent frames, and calculating the local standard deviation of each differential frame (Video B.2). A kymograph was then built by taking a cross section of the processed video along a manually selected line that would follow the direction of propagation of the wave. The average slope of the characteristic regions of high intensity in this kymograph (typical of travelling waves) is the reciprocal of the wave velocity c, and the wavenumber is then $q_{wave} = 2\pi\nu/c$, where ν is the CBF. **(c)** Manual measurement of the metachronal wave in a microscopy video of an ovine trachea, published as supplemental information in [89]. The measuring line (white) is defined so to be perpendicular to the wavefronts (red lines). The wavelength is then the distance between two wavefronts along the measuring line: $\lambda = (70 \pm 2)\,\mathrm{px}$ at 30° from the horizontal axis. **(d)** The lag-time-averaged Image Structure Function of the same video clearly shows two peaks at low Fourier modes m_x and m_y (red $+$) symmetrical with respect to mode $(0, 0)$ (white $+$). Then $\lambda = 2\pi/q = L/\sqrt{m_x^2 + m_y^2} = 57.3\,\mathrm{px}$, and the propagation direction is $\theta = \tan^{-1}(q_y/q_x) = 26.6°$. The confidence intervals are $\lambda \in [50.2, 81.0]\,\mathrm{px}$, and $\theta \in [11.3°, 45°]$, obtained assuming a ± 0.5 uncertainty on both m_x and m_y. The large confidence intervals are a direct consequence of the inherently poor spatial resolution at low Fourier modes. The manual and DDM results are in very good agreement.

We found that DDM is particularly well suited to spot metachronal waves, as shown in Figure 3.6a: Since a metachronal wave is a travelling wave with a well-defined wavelength λ, it creates a very sharp peak in the Image Structure Function at the spatial frequency corresponding to its wavenumber $q_{wave} = 2\pi/\lambda$. The wavelength obtained in a completely automated fashion by DDM was then cross-checked with a manual measurement, obtaining good agreement. Details of this alternative method are in Figure 3.6b and in the supplementary materials.

A second example of DDM-based detection metachronal wave is shown in Figure 3.6c and 3.6d: we analysed a microscopy video published as supplemental information in [89] featuring a very well developed MW in ovine tracheal tissue, obtaining a measurement of

wavelength and propagation direction in good agreement with a manual measurement. To manually analyse the video first we measured the slope of a line drawn along each wavefront, as shown in Figure 3.6c (red lines). The wavelength is then measured along a set of several parallel lines drawn perpendicularly to the wavefronts (an example is in white in Figure 3.6c). A measurement of λ was taken at each frame per each measurement line as the distance between two peaks of the gradient of the pixel-value cross-sections along the measurement line, yielding $\lambda = (70 \pm 2)$ px for measuring lines at $30°$ from the horizontal axis. The DDM algorithm was then run on the video, but without performing the azimuthal average on $\mathbf{q}$, so to yield an Image Structure Function $I(\mathbf{q}, \tau)$. The metachronal wave showed up in the $I(\mathbf{q}, \tau)$ as a pair of sharp, symmetrical $\mathbf{q}$-peaks (Figure 3.6d). The wavelength can be calculated as $\lambda = 2\pi/|\mathbf{q}|$, while the propagation direction of the metachronal wave can be measured as $\theta = \tan^{-1}(q_y/q_x)$. As shown in Figure 3.6, the manual and DDM results are in very good agreement.

3.4 Multiscale-DDM can provide information about the spatial coordination of beating cilia

Spatial information on how cilia are coupled can be recovered from the analysis of a sample with an extension of the DDM algorithm. In the scope of this work, interesting information are whether the DDM is able to give an estimate of a length scale across which cilia beat cooperatively, if the algorithm is able to detect a metachronal wave, and how this shows up in the $I(q, \tau)$ signal. The latter two points are discussed in sections 3.3.3 and A.2. The case of *in vitro* cultures, where the metachronal coordination might not be evident, is where a DDM-based, multiscale approach can be powerful particularly giving valuable information about ciliary coordination. In this section we exploit an idea already mentioned in section 3.3.1: that the characteristic time τ_c for the decay of the oscillations in the time behaviour of the Image Structure Function accounts both for how well synchronised the cilia in the FOV are, and for how consistent the period of each cilium is over time. In this section we show how, by running the DDM algorithm on a whole series of tilings of the field of view, we can extract a coordination length scale, a characteristic length of our system over which the coordination between cilia is lost.

Length scale of synchronisation: *in vitro* samples

The hypothesis of a better synchronisation amongst cilia on the same cell than across different cells is easy to verify. The resolution of all videos in the dataset described in section 3.2.1 is

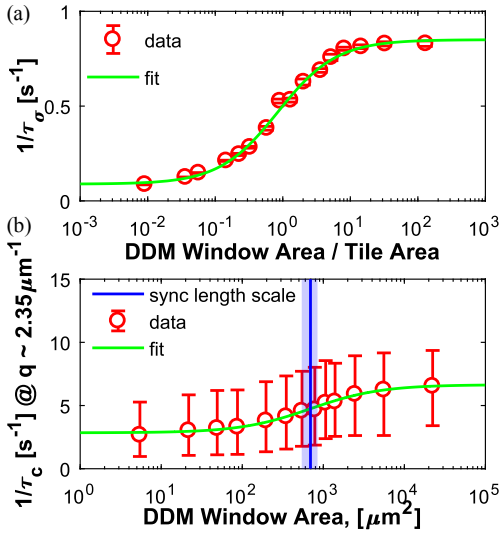

Fig. 3.7 **DDM can detect a characteristic length scale for synchronisation.** **(a)** The DDM algorithm was run on computer generated data (see section A.3), a greyscale matrix with pixel intensity oscillating over time, divided into phase-locked hexagonal tiles. This was done several times, changing the area ("window") of DDM. Notably, the decay time τ_σ of $\langle I(q,\tau)\rangle_q$ diverges when the DDM window becomes smaller than the size of a phase-locked tile. The transition is smooth because of the shape mismatch between the hexagonal tiles and the square DDM windows. The green line is an empirical fit of the data to $1/\tau_\sigma = ax/(x+b)+c$, where x is the DDM window area normalised over the area of the hexagonal tiles. The error on the data is comparable with the marker size. **(b)** In experimental data a similar behaviour is observed when plotting the reciprocal $1/\tau_c$ of the decay time of $I(q',\tau)$ against the size of the DDM window (following section 3.4). Again the decay time increases significantly when the DDM algorithm is run on a small enough window, here this happens at $\approx 700\,\mu\mathrm{m}^2$. The red markers show the median, and the error bars the 25$^{\text{th}}$ and the 75$^{\text{th}}$ percentile for each value of the DDM window area. The green line is an empirical fit of the data to $1/\tau_c = ax/(x+b)+c$, while the blue line shows the position of its inflection point with the 95% confidence interval in shaded blue.

$1920\,\mathrm{px} \times 1024\,\mathrm{px}$. First, a square region of the largest possible size, $1024\,\mathrm{px} \times 1024\,\mathrm{px}$, is selected in each video and analysed with the DDM algorithm. Then, the region is divided in smaller sub-regions, and the DDM is run on each one. This process of 'multiscale-DDM' continues with the "window" on which the DDM runs getting smaller and smaller (from $1024\,\mathrm{px} \times 1024\,\mathrm{px}$ to $16\,\mathrm{px} \times 16\,\mathrm{px}$). The $I(q,\tau)$ signal of each window is fitted as in eq. (3.1), thus extracting an amplitude, frequency and (the one this section focuses on) decay time as a function of q for each region ($A(q)$, $\nu(q)$, $\tau_c(q)$). Comparing values of $\tau_c(q)$ as a function of the DDM window size should give insight into the length scale of synchronisation. As the DDM algorithm was run on regions of different size, also the range of spatial frequency q it probed is different (although overlapping). In order to compare the decay time $\tau_c(q)$

across different sizes of the analysed region, one interval in q was selected. This interval ($q = 2.35 \pm 0.4\,\mu\mathrm{m}^{-1}$) was chosen so that all $\tau_c(q)$ curves (one for each DDM window, or box) have at least one point in it. The reciprocal of the decay time, measured as the median of the distribution of $\tau_c(q)$ at $q \approx 2.35\,\mu\mathrm{m}^{-1}$ across the windows of the same size on all 30 videos in the dataset is plotted in Figure 3.7b against the size of the DDM window. The median of the distribution, and not its mean, was chosen to increase robustness against outliers. The plot shows that the decay time increases significantly when the DDM window becomes smaller than a critical area, estimated to be $\approx 700\,\mu\mathrm{m}^2$ by fitting the data to the empirical curve

$$1/\tau_c = ax/(x+b) + c \tag{3.2}$$

where x is the window area, and locating its inflection point (the empirical curve is a sigmoid when plotted on a logarithmically spaced $x-$axis). This value is significantly higher than the area of a single ciliated cell, whose diameter is $\approx 10\,\mu\mathrm{m}$ [123].

3.5 DDM can identify the beating direction

One of the steps of the DDM algorithm, as presented in 2.2 and 3.3, is the azimuthal average of the Image Structure Function $I(\mathbf{q}, \tau)$ over the angles of the scattering vector $\mathbf{q}$. In a sample with anisotropic dynamics this step effectively leads to the loss of information about the anisotropy. While this was acceptable in the case of cilia as a first approximation, it is worth remembering that DDM can indeed access this information [111].

The benefits of accessing the information on anisotropy are obvious in the case of cilia, as it would mean measuring the direction along which the cilia beats. This would make DDM an invaluable tool also in the study of Planar Cell Polarity, as there are still open questions about how the cilia align themselves to all beat in the same direction *in vivo*, why this does not happen *in vitro*, and how the *in vivo* results can be achieved *in vitro*.

In simple cases, as for example small particles oscillating back and forth, all moving along the same direction, it is easy to use DDM to find the direction of movement: without the average across the angles of the scattering vector, the direction of movement is simply the angle in the (q_x, q_y) plane where, in the relevant q-range, the signal $I(\mathbf{q}, \tau)$ is maximum. This simple example is shown in Appendix A and Figure A.1.

In vitro ciliated epithelia are a much more complicated system, in which the simple approach of the previous paragraph does not work for two reasons. First, when imaging *in vitro* ciliated epithelia a field of view typically contains cilia that beat in different directions. This is a problem easy to overcome: one only needs to divide the field of view into smaller tiles and analyse the section of the microscope video pertaining to each tile to have a spatially-

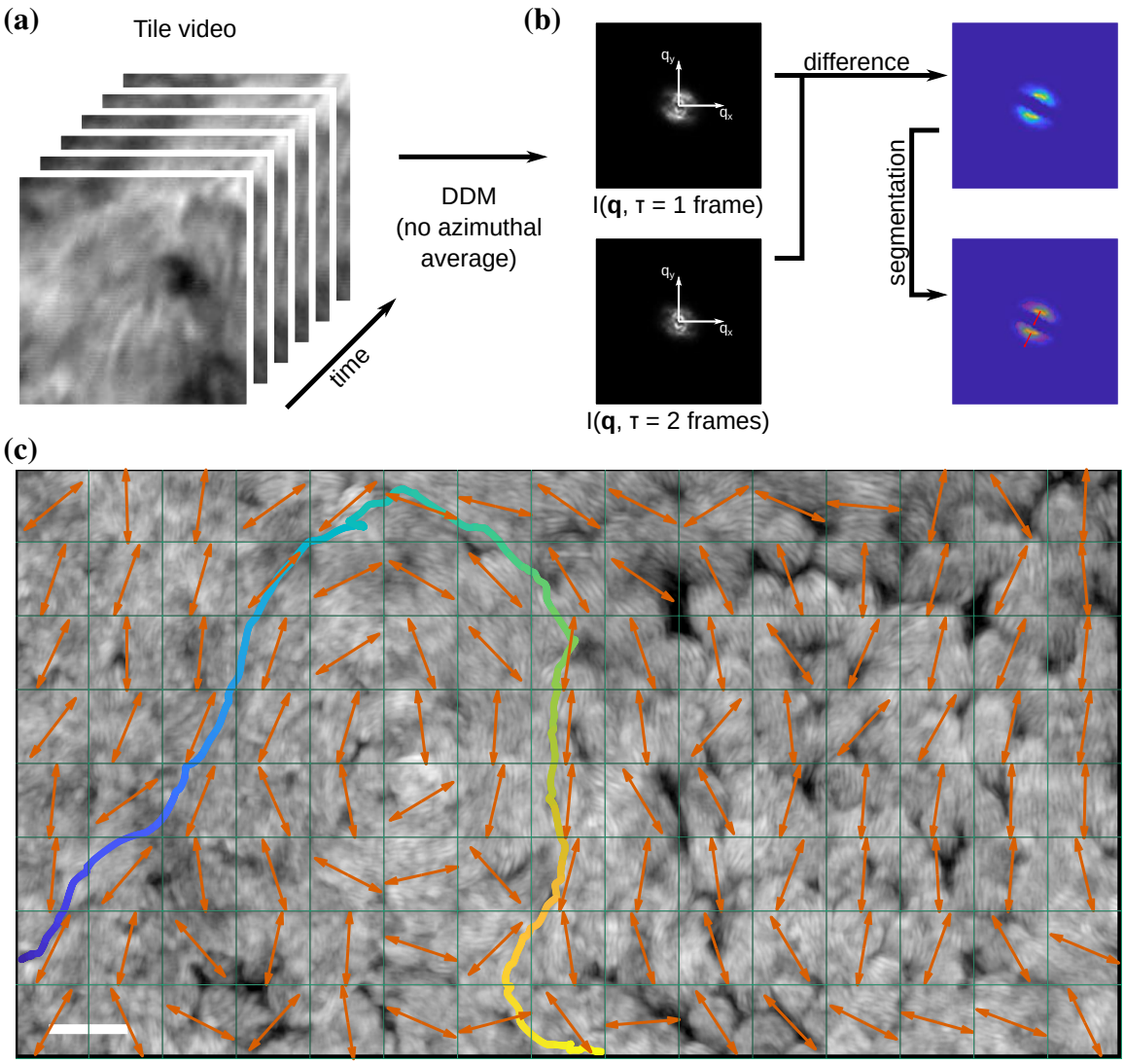

Fig. 3.8 **DDM can measure the beating direction.** **(a)** The FOV is first divided into small tiles within which the beating direction is homogeneous. **(b)** The difference between the image structure function at the two smallest accessible values of τ highlights two oblong regions in the (q_x, q_y) plane in which the signal is relatively higher in $I(\mathbf{q}, \tau = 1\,\text{frame})$ than it is in $I(\mathbf{q}, \tau = 2\,\text{frames})$. The short axis of these regions, identifiable via segmentation, is aligned with the beating direction. **(c)** Repeating the analysis described in **(a)** and **(b)** over all the tiles (in green) of the FOV yields a spatially resolved measurement of the beating direction (orange arrows). This was found to be in good agreement with visual evaluation of the high speed microscope video (motion map in the background) and with tracking of impurities propelled by the cilia (line indicating the trajectory, with the time going from blue to yellow). Scale bar is $20\,\mu\text{m}$.

resolved measurement of the beating direction (Figure 3.8a,c). The other issue that makes finding the beating direction challenging is that, even in a tile within which all cilia are

aligned, the direction in the (q_x, q_y) plane where the signal $I(\mathbf{q}, \tau)$ is maximum changes with τ. We hypothesise that this stems from the fact that DDM takes differences of images of, in this case, long filaments imaged from above. When the time difference between the two subtracted frames τ is high, one can see long stripes in the differential image caused by cilia parallel to the focal plane. These stripes then give a high contribution to the 2D Fourier transform. To prevent this we only look at the very fast dynamics (Figure 3.8b), measuring the Image Structure Function only up to the two shortest values of τ we can access (1 and 2 frames). We then normalise $I(\mathbf{q}, \tau = 1\,\mathrm{frame})$ and $I(\mathbf{q}, \tau = 2\,\mathrm{frames})$ so that they only assume values between 0 and 1, and take their difference. This process effectively finds the areas in the (q_x, q_y) plane in which $I(\mathbf{q}, \tau = 1\,\mathrm{frame})$ has a stronger signal relatively to $I(\mathbf{q}, \tau = 2\,\mathrm{frames})$. These areas are of oblong shape, with their short axis aligned to their beating direction. A simple intensity-based segmentation to identify the short axes of the two oblong regions in the fast-dynamics signal yields therefore the beating direction.

This empirical algorithm does not require any input by the user once the size of the tiles has been chosen, and yields a spatially resolved measurement of the beating direction (a "direction field"). We found the results to be accurate, and in good agreement with both visual examination of the high speed microscopy videos and manual tracking of the rare impurities that are transported by the ciliated epithelium (Figure 3.8c). We are however attempting to perform this same measurement of beating direction with a different technique so that we can thoroughly cross-validate the results.

3.6 MultiDDM probes the coordination in time and space of ciliated epithelia

We have presented a new toolkit for the analysis of ciliated tissues based on Differential Dynamic Microscopy, extending to "multiscale-DDM", proving this to be a valuable tool to measure the ciliary beat frequency of *in vitro* human airways ciliated cells at the air-liquid interface. On one hand, this yields results in agreement with point-FFT approaches but in a completely automated procedure without any user input, thus reducing a source of bias and speeding up the analysis. This suggests DDM analysis to be a serious alternative to commercial software for providing a reliable, fast and unbiased estimate of the ciliary beat frequency, even in a clinical environment. On the other hand, conceptually new information is retrieved using DDM compared to fixed-point FFT analysis: the algorithm gives an output signal which is closely related to the intermediate scattering function, quantifying fully the system dynamics.

Guided also by simulated data, presented in more depth in Appendix A, we have suggested new ways of extending the DDM algorithm ("multiDDM") to extract spatio/temporal information from the samples, namely the correlation length for cilia beating.

The analysis algorithm was also shown able to detect the presence of a large length scale feature such as a metachronal wave, and to measure its wavelength and direction. Being able to estimate these quantities (a length scale across which movement is coordinated, the angular spread of cilia beating, and properties of the metachronal wave) is fundamental towards a possible employment of DDM in a clinical environment, in particular to assess the structural and functional integrity of ciliated tissues. For example, in chapter 4 we use multiDDM to assess how modifying the mucus rheology affects the ciliary movement in samples from Cystic Fibrosis donors. This technique could also be of use in studying if and how ciliated airways tissues can recovery after being damaged because of a blast wave [124] or in regenerative medicine.

Chapter 4

Response of respiratory ciliated epithelia to changes in the rheology of the mucus layer

4.1 MultiDDM as a tool to assess the response of ciliated epithelia to drug treatments

This chapter is focused on testing our new method on an important disease, Cystic Fibrosis (CF). CF is a life-threatening genetic disorder caused by loss-of-function mutations in the cystic fibrosis transmembrane conductance regulator (CFTR) gene [125].

This study was conducted in collaboration with Dr Maurizio Chioccioli, a postdoc in our group, and Dr Preston Bratcher, from the Division of Pediatric Pulmonary Medicine at National Jewish Health, in Denver, CO, USA, who provided cells and shared in the study design.

After introducing the F508del/F508del mutation, which is one of the genotypical causes of Cystic Fibrosis (section 4.2), and three drugs used to tackle its effects (section 4.3), in section 4.5 multiDDM analysis is used to measure CBF and cilia coordination on human airways epithelial cells (HAEC) samples from subjects both healthy and affected by the F508del/F508del mutation. The ability of multiDDM to quantify the loss of cilia coordination over distance is used here to measure how coordination is affected by mucus properties in both direct perturbations and pharmacological intervention, providing new important information about coordination of cilia dynamics in the context of CF. In particular, section 4.6 shows data collected upon repeated washes of the mucous layer on samples from CF patients. In section 4.7 instead multiDDM is used to demonstrate the efficacy of the CFTR-modulating

drug combination of VX-770 (ivacaftor/ KALYDECO®) and VX-809 (lumacaftor, together termed ORKAMBI®) on HAECs derived from subjects homozygous for F508del CFTR. We also investigated the effect of VX-809 alone on these cells, as well as a recently-reported CFTR-modulating compound Tα1 [126]. The development of a rapid, quantitative assay for characterising collective cilia beating dynamics in a standard cell culture model has important applications in diagnostics and drug screening. To our knowledge, these data represent the first in-depth, quantitative assessment of cilia coordination in HAECs derived from subjects with CF and how this changes in response to CFTR-modulating drugs. Although this study applies multiDDM analysis to investigate ciliary beating dynamics in the context of CF, this technique could be applied to the other respiratory diseases in which ciliary beating is affected.

4.2 Homozygous F508del mutation of the Cystic Fibrosis Transmembrane conductance regulator gene

Cystic Fibrosis (CF) is one of the most common lethal autosomal recessive diseases in the Caucasian population [100, 125, 127]. It does not only affect the lungs, but all mucus-producing organs, such as the lungs, sinuses, reproductive organs, intestine, and pancreas [127]. In the airways, CF causes the build-up of thick, sticky mucus of abnormal composition. This in turn reduces the mucociliary clearance, which can then lead to plugging of the airways, and favour the onset of chronical bacterial infections and inflammations [43, 127, 128].

As discovered almost 30 years ago, CF is caused by a mutation in the CF TransMembrane conductance regulator gene (CFTR) [70, 100]. More than 1500 mutations have been identified so far, albeit not all mutations cause CF. Only a few mutations have been characterised extensively enough to learn their functional importance [100].

The lack of a Phenylalanine at position 508 (F508del) is the most common mutation by far, accounting for about $2/3$ of mutated alleles in Caucasian patients [100]. During translation, the missing amino acid causes the synthesis of a protein with a folding defect. When the quality control mechanism in the endoplasmic reticulum recognises the defect, the protein is chaperoned, ubiquinated, and marked for degradation [100]. Misfolded proteins that get to the cell surface despite the quality control mechanism only retain a degree of the normal levels of functionality [100, 125].

The CFTR gene encodes for a Chloride channel present on the surface of several epithelia that also acts as a regulator for other membrane proteins, including the epithelial sodium channel (ENaC)[127].

Malfunction of the CFTR gene leads to dehydration of the airways. In particular, the concentration of mucins in the mucus layer increases. By osmosis, the mucus layer then draws more water from the periciliary layer, which is in part occupied by mucins tethered to the surface of cilia. The PCL collapses, greatly hindering the ciliary beat, if the concentration of mucins in the mucus layer grows past a critical value of $5\,\%$ solid, as the osmotic pressure of the PCL becomes lower than that of the mucus layer [43, 70, 127].

The impaired mucociliary clearance then paves the way to bacterial growth, and the formation of biofilms. This in turn triggers a complex biological feedback mechanism: for example, bacterial inflammation causes an increase of the number of goblet cells (goblet cells hyperplasia) and the recruitment of neutrophils (one type of white blood cells, part of the innate immune system). The immune system response leads to the release of extracellular DNA in the mucus, worsening its properties and further reducing clearance [127].

Only the most common CF-causing mutations expressed by large groups of subjects have been targeted for drug screening due to the high cost and time-consuming nature of clinical trials. Many mutations that are rare or uncharacterised have not been tested for their responsiveness to clinically available CF drugs yet.

However, a recent study showed that selected CFTR-modulating drugs used to treat patients with the common F508del-CFTR mutation could in some cases be effective in treating patients with rare, uncharacterised CFTR mutations that are currently not registered for treatment, if only cost-effective assays could be used to screen such samples [129]. MultiDDM is a technique that could be useful in this direction.

Airways mucus is a complex material that behaves, from a rheological point of view, as a viscoelastic gel-like material [130]. Mucus owes its gel-like properties to its main organic components, a family of gel-forming proteins called mucins. These cross-link and form a network via both covalent bonding and reversible interactions, such as electrostatic and hydrophobic interactions [131–133]. The viscoelastic properties of the mucus affect the ability of the mucociliary clearance mechanism to transport it along the epithelium. In particular, transport is hindered if the mucus rheology exhibits a marked elastic component [134]. This is relevant since, as mentioned in the section above, CFTR mutations lead to an increase in the mucins concentration in CF mucus, and hence to an increase in its solid content [133, 135]. In turn, the high percentage of solid content typical of CF mucus has been shown to cause both a reduction of the pore size of the mucins network and, crucially, an increase of about two orders of magnitude in the elastic modulus of CF mucus with respect to “healthy” mucus [133, 136].

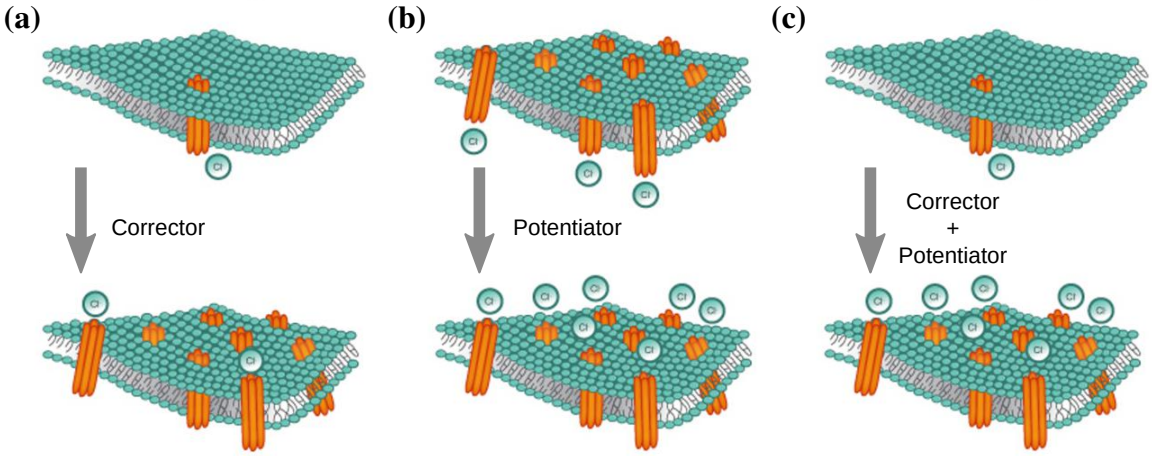

Fig. 4.1 **Action of CFTR-modulating compounds.** Administration of **(a)** CFTR correctors increases the number and function of CFTR channels at the cell surface, while **(b)** CFTR correctors increase the gating ability of such CFTR channel. Since in the F508del mutation both the number of CFTR proteins located at the cell membrane and their gating are reduced, **(c)** a combination of a corrector and a potentiator is needed to rescue CFTR functionality. Figure adapted from www.cftr.info.

4.3 CFTR modulating drugs

The F508del-CFTR mutation affects both protein folding and channel gating, resulting in a protein which not only does not function properly but where the majority is degraded before it can reach the plasma membrane. Given the two distinct defects caused by F508del-CFTR, it is generally believed that two complementary strategies are required to target it (Figure 4.1). Agents that correct the location of the protein, allowing it to leave the endoplasmic reticulum for the cell surface, are called “correctors", while drugs that enhance the activity of correctly located CFTR proteins are called “potentiators". The combination of a corrector and a potentiator can increase the number of CFTR proteins at the cell surface and improve their functionality [100].

VX809 (Lumacaftor)

VX809 is a CFTR corrector, as it increases the trafficking of the CFTR protein to the cell membrane. It acts as a chaperone, promoting the folding process of a fraction of F508del-CFTR and allowing it to exit the endoplasmic reticulum without being tagged for degradation, and has been shown to have a significant impact in *in vitro* testing [137, 138]. In a randomised, double-blind, placebo-controlled study on a cohort of patients, however, while VX809 alone

improved CFTR function in the sweat glands, it did not have any clinically significant effect on the nasal epithelium nor on lung function [139].

VX809/VX770 (Lumacaftor+Ivacaftor)

VX770 is a CFTR potentiator, and has been shown to increase the gating activity of the CFTR protein in *in vitro* F508del samples [138, 140]. However trials on patients showed no clinically significant effect, and VX770 was not authorised for treatment of homozygous F508del CF [138].

While separate treatments with VX809 and VX770 were not deemed effective enough in treating patients with the homozygous F508del CFTR mutation, their combined corrector/potentiator effect was shown to provide a benefit for patients in clinical trials [138, 141]. The drug was approved for use by the FDA and is commercialised with the trade name ORKAMBI® (Vertex Pharmaceuticals Boston, MA.).

Thymosin α1

Thymosin α1 (Tα1, commercialised as ZADAXIN®) is a peptide of 28 amino acids that is already used routinely as an immunomodulator for treating viral infections, immunodeficiencies, HIV/AIDS, and, notably, infections of the airways, for example in COPD [126, 142]. Its potent anti-inflammatory action prompted a study to assess its effectiveness to alleviate inflammation in the early stages of CF, possibly breaking the vicious circle that leads to chronically inflamed lungs in response to infectious agents. A very recent study by Romani et al. [126] conducted on mouse models and human bronchial epithelial cells reported that not only Tα1 has a beneficial effect in improving inflammation and immune tolerance in CF, but it also has a secondary effect of increasing the trafficking, stability, and gating of F508del-CFTR. Unlike VX809 and VX770, Tα1 is primarily an anti-inflammatory drug, that can also rescue F508del-CFTR functionality. Its cost-effectiveness and safety suggest that it will be tested in clinical trials as a beneficial treatment for CF.

4.4 Experimental methods

Data featured in this chapter were collected in-house both on the commercially available assays described in section 3.2.1 and on ciliated epithelia cultured from primary clinical samples by Dr Preston Bratcher at National Jewish Health in Denver, Colorado. Data collection was performed in collaboration with Dr Maurizio Chioccioli, who also co-designed the experiment.

4.4.1 Study design

The overall objective of this chapter was to use the recently developed multiDDM algorithm to characterise ciliary beating in cells from subjects with CF, and to test whether the approach was sensitive enough to detect changes in ciliary beating over time and in response to various drug treatments.

As a first-pass, we applied multiDDM to the primary HAECs purchased from Epithelix detailed in section 3.2.1 and manipulated the mucous layer to affect ciliary beating. Once our approach was validated – i.e., it became clear that the data obtained from multiDDM analysis could be used to distinguish between different samples under different conditions - we obtained primary clinical samples for experiments involving CFTR-modulating drug treatments. For every experiment, the DDM analysis was based on data collected from HAECs obtained from three different subjects, either healthy subject controls or cells harbouring the F508del/F508del mutation in CFTR. We chose to focus on this mutation as it is the most common cause of CF and one for which at least one therapeutic drugs has been approved (ORKAMBI®).

At least sixteen - often more - videos were taken of each of the samples at each data collection point, avoiding the perimeter of the cell culture insert due to the accumulation of mucus in that region (an experimental artefact caused by the geometry of the vessel). MultiDDM analyses were performed as previously described in [143] and chapter 3 and in such a manner as to ensure the entire field-of-view was represented in an unbiased manner. This study was not blinded.

4.4.2 Culture of nasal epithelial cells from primary clinical samples

Culturing of ciliated epithelia from primary clinical samples was performed by Dr Preston E. Bratcher.

HAECs were isolated from nasal brushings of the inferior turbinate performed using a cytology brush on CF subjects attending the Adult Clinic at National Jewish Health (Denver, CO, USA). Samples were collected using a protocol approved by the Institutional Review Board at National Jewish Health, and all subjects provided written informed consent. The median age of the donors was 41 years old, 4/6 were female, and all were Caucasian and of the CFTR genotype F508del/F508del.

Nasal epithelial cells obtained from brushings were expanded in culture using previously described methods of conditional reprogramming culture (CRC) [144]. Briefly, nasal brushing samples were dissociated in Dulbecco's phosphate buffered saline solution containing $5\,\mathrm{mM}$ EDTA and $5\,\mathrm{mM}$ EGTA and mechanically processed by repeatedly pipetting. After washing,

cells were resuspended in CRC medium containing the rho-kinase inhibitor, Y-27632, and plated on a feeder cell layer of gamma-irradiated 3T3 fibroblasts. Reprogrammed epithelial cells were expanded at $37\,^{\circ}\mathrm{C}$ in a humidified incubator in an atmosphere containing $5\%\,\mathrm{CO_2}$, removed using two-stage trypsinisation, and replated on a fresh feeder layer. After reaching $\sim\ 80\%$ confluence, passage 2 cells were aliquoted and stored in liquid nitrogen. Later, thawed cells were plated onto feeder layers in CRC media with Y-27632 and expanded until $\sim 80\%$ confluence was reached. After a two-stage trypsinisation and treatment with DNase I, cells were plated onto collagen-coated permeable supports in a 24-well format (Corning Incorporated, Tewksbury, MA, USA) at a density of $10^5\,\mathrm{cells/cm^2}$. Once confluence was reached, apical media was removed and basal media was switched to PneumaCult ALI media (STEMCELL Technologies). Cells formed well-differentiated cultures after 4 to 6 weeks at the air-liquid interface.

4.4.3 Mucus washing

The experiments described in this chapter required the mucous layer present on the epithelial layer to be washed. This was done by incubating the apical surfaces for 20 minutes in $200\,\mu\mathrm{l}$ sterile Phosphate-Buffered Saline, PBS (GIBCO™), and then gently removing the solution by suction pipette. This procedure was repeated twice.

4.4.4 CFTR-modulating drug assays

Solutions of VX-809 (lumacaftor; Selleck Chemicals LLC, Huston, USA), and VX-809 and VX-770 (ivacaftor; Selleck Chemicals LLC, Huston, USA) were prepared in DMSO (Sigma) at $3\,\mathrm{mM}$, $0.1\,\mathrm{mM}$ concentrations respectively. Thymosin $\alpha 1$ (Tα1, CRIBI Biotechnology, Padova, Italy) was reconstructed in MilliQ water at $100\,\mu\mathrm{g/ml}$ concentration [126]. All compounds were then diluted 1000-fold in culture media and added basolaterally to HAECs in ALI culture at 0, 24, and 48 hours into the experiment. The control treatment consisted of dimethyl sulfoxide (DMSO) 0.1% (Sigma).

4.4.5 Data processing

The results presented in this chapter are obtained employing multiDDM as detailed in chapter 3 and in [143].

Distributions of CBF featured in sections 4.5.1, 4.6.1, and 4.7.1 are obtained by dividing the field of view of each microscopy video in small tiles of $\sim\ 9.3\,\mu\mathrm{m}$ side and running

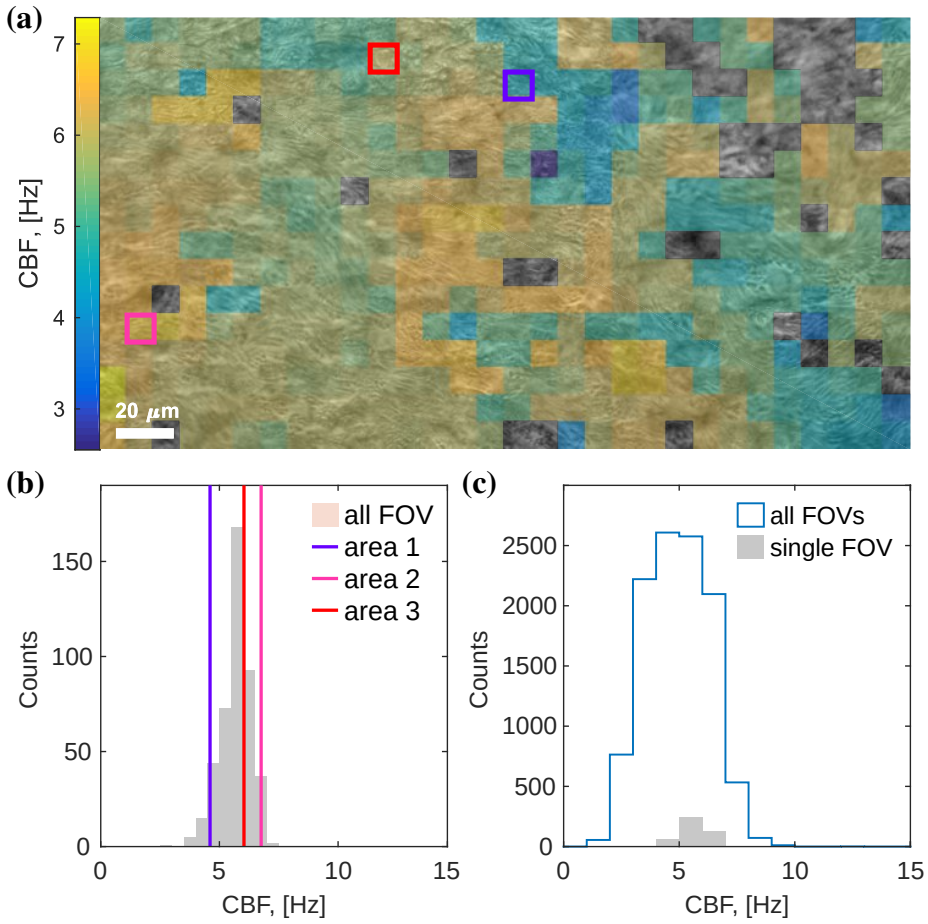

Fig. 4.2 **MultiDDM captures the CBF distribution of a sample.** **(a)** shows an example image from a microscopy video used in the analysis. To build a full distribution of CBF values we divided the whole field of view into a collection of square tiles, and measured the CBF via DDM on each of the tiles. Here the measured CBF values are overlaid (in false colours) to the video microscopy frame. Tiles where no motion was detected are left transparent. Three boxes are highlighted as an example, and their CBF reported in **(b)** overlaid to the full CBF distribution of the field of view (grey). To have a more exhaustive measurement of CBF of an ALI sample one should take several microscopy videos from FOVs scattered around the insert: **(c)** shows the distribution of CBF values built by aggregating the distributions from all such FOVs. We also show on the same axes, for sake of comparison, the same CBF distribution as in **(b)**.

the DDM algorithm on the tiles that showed movement, and pooling together CBF values obtained by tiles belonging to different videos taken across the sample (Figure 4.2).

The sigmoidal curves showing the loss of coordination upon increasing the DDM tile size are built by pooling together data from many fields of view on the same sample. For each analysed tile size, we build the distribution of values of decay time τ_c measured on tiles

of matching size across all videos on the same sample. The marker in the plots shows the medians of such distributions, while the whiskers show the 25$^{\text{th}}$ and 75$^{\text{th}}$ percentiles (see an example in Figure 4.3). The experimental data points are then fitted as

$$\tau_c^{-1} = \frac{a}{1 + \mu/A} + c, \tag{4.1}$$

where a and c give the level of the left and right plateaus, A is of the area of the DDM tile. In a plot with the x-axis on a logarithmic scale, this curve is a sigmoid, and μ is the abscissas of its inflection point. The left and right shoulders of the sigmoidal curve are then the abscissas ($\lambda^2 = \mu \mathrm{e}^{-2}$ and $\Lambda^2 = \mu \mathrm{e}^{2}$) of the points where, again in a plot with the x-axis on a logarithmic scale, the line that best fits the central slope meets the prolongation of respectively the left and right plateaus.

Improved motion detection algorithm

The motion detection used for the experiments in sections 4.5 and 4.6 is described in chapter 3, and relies on thresholding an image obtained by taking the standard deviation of the fluctuation of each pixel's recorded grey level over time. This simple approach works well in most cases, but struggled in some videos during the experiments described in section 4.7, because it did not discard some DDM tiles where there was no ciliary motion. We therefore devised a different motion detection algorithm, geared towards better performances in case of low signal-to-noise ratio.

In this revised algorithm we take differences between every other frame, to highlight regions where the sample shows fast motion. These images undergo a median filtering, to reduce the effect of camera noise, and a local standard deviation filtering. This last filter highlights regions with high alternation of dark and bright pixels, where the moving cilia are located. We then take the $\log_{10}$ of the standard deviation across all these filtered images. The motion map thus obtained is bright in correspondence of moving cilia, and dark over static regions of the sample. Segmentation then finds the foreground features, where the beating cilia are. This is done by fitting the dark end of the pixel values histogram with a Gaussian, and marking as background (so, no moving cilia) all pixels with value smaller or equal than the sum of mean and width of the fitted Gaussian.

This algorithm essentially differs from the one described in chapter 3 in that by looking at the difference between subsequent frames we are favouring the signal corresponding to fast timescale motion, and in that we take the motion map is built by taking the logarithm of the standard deviation across filtered differential images. This was seen to improve the

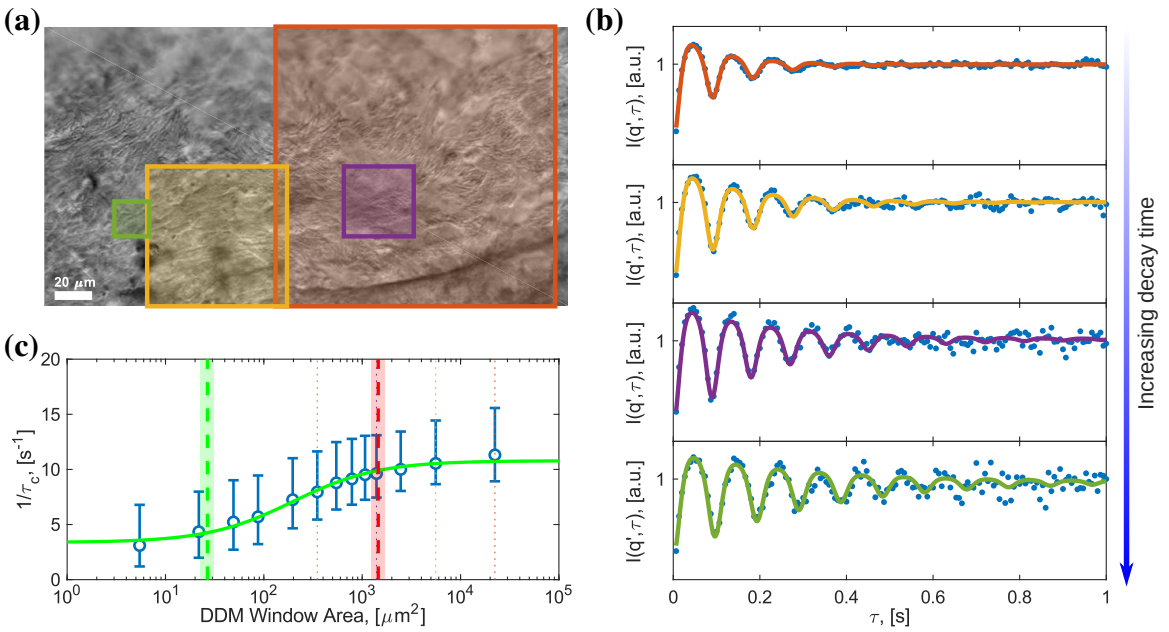

Fig. 4.3 **MultiDDM decouples the contributions to the decay of the ISF.** MultiDDM can measure a synchronisation length scale by systematically changing the size of the regions DDM is run on, to probe to which extent cilia beating is coordinated in space. To measure the synchronisation length scale we first divide the field of view into tiles, repeating this process while systematically increasing the size of the tiles. DDM is then run on each tile. In **(a)** we show the outline of 4 tiles, each of a different size, as an example. As extensively detailed in section 3.3 we can fit the time dependence of the Image Structure Function with an oscillating function multiplied by an exponentially decaying term. The frequency of the oscillations is the CBF, while the time constant of the decaying term is a proxy for how well coordinated the motion within the analysed region is. **(b)** shows examples of the oscillating and decaying behaviour of the Image Structure Function. Fitted curves (solid lines, colours matching the respective regions in **(a)** are superimposed to the experimental data (dots), showing excellent agreement. Note how the time constant increases for smaller tiles. In **(c)** we build a sigmoidal curve by plotting the median of the inverse time constant τ_c (circles, while whiskers show the 25$^{\text{th}}$ and 75$^{\text{th}}$ percentile) measured at each tile area across several fields of view. By fitting the experimental data points with eq. (3.2) we can locate the shoulders of the sigmoidal curve (geometrically, this is where the left and right plateau respectively meet with the line that approximates the central slope). Physically, the right shoulder marks the length scale above which there is no coordination left, while the left shoulder locates the length at which objects start not being perfectly coordinated. As the left and right shoulders are separated by a fixed shift on the (log-scaled) x-axis (see eq. (3.2)) we will be using either of the two, according to which one falls within the accessible range of our microscope setup. The position of the left and right shoulder is shown here as dashed vertical lines lines (in green and red respectively), while the shaded region indicates the 68 % confidence interval. The area of the highlighted tiles in **(a)** is reported here as a dotted line of matching colours.

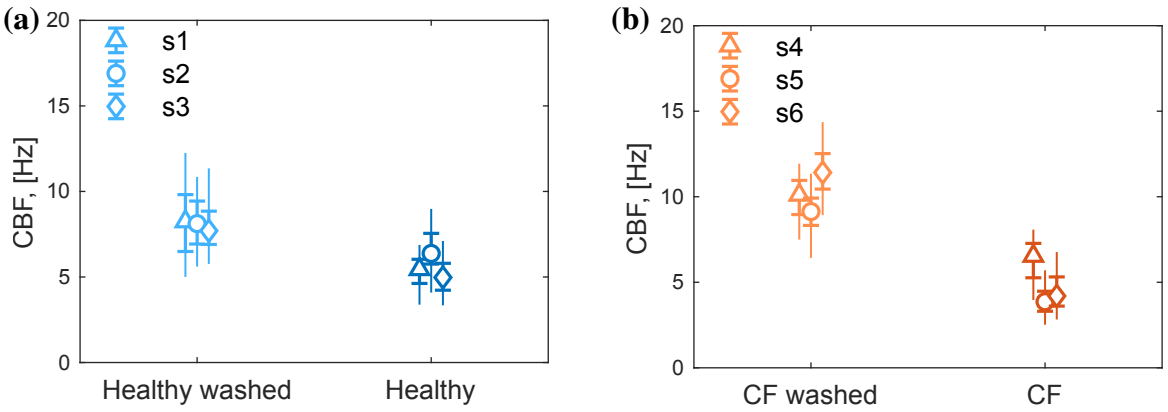

Fig. 4.4 **Rheological properties of mucus affect the CBF. (a)** CBF measured on cells obtained from healthy subjects (s1 to s3) compared to **(b)** subjects with CF (s4 to s6). The CBF was measured before and after mucus removal. Markers show the median, the horizontal caps mark the 25$^{\text{th}}$ and 75$^{\text{th}}$ percentile, and the vertical thin lines mark the 5$^{\text{th}}$ and 95$^{\text{th}}$ percentile. CBF was measured on at least 20 FOVs, using a tile of $\sim 9.3\,\mu\text{m}$ side.

thresholding in case of low signal-to-noise ratio. This algorithm was seen to reliably work as long as some static regions are present in the field of view.

4.5 Collective dynamics in ciliated epithelia of healthy and CF samples

We used multiDDM to compare CBF and cilia coordination in HAECs from both healthy donors and from subjects affected by CF. CF samples are characterised by a defective CFTR gene, which leads to a loss of airway surface liquid and incompletely hydrated periciliary layer. This results in a thick mucus layer that restricts cilia beating.

4.5.1 CBF in healthy and CF samples

The distribution of CBF measured on three healthy samples and three CF samples are shown in Figure 4.4. CF samples show a lower frequency than the healthy ones in the presence of mucus. In line with the literature, we hypothesise that the difference in CBF between the healthy and CF sample is attributable only to the physical properties of the mucus, since the CFTR mutation only affects the properties of the mucous layer but not the structure or function of the cilia [100]. We therefore analysed the CF samples following a wash treatment to remove the mucus layer. CBF values following mucus removal are higher than in the presence of mucus, for both healthy and CF samples. Moreover, the CF samples do not

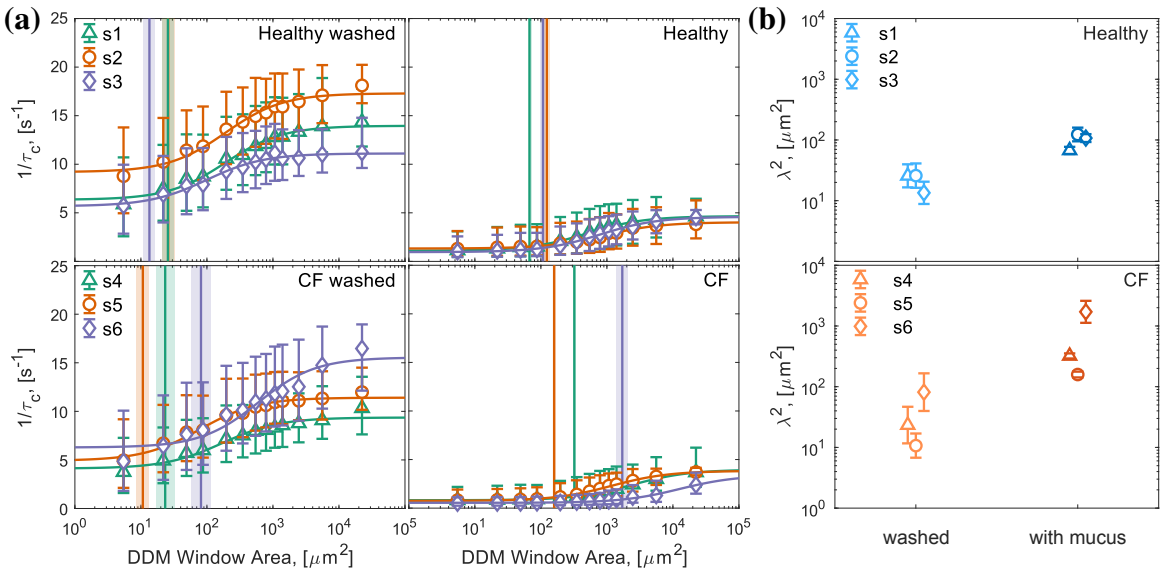

Fig. 4.5 **Rheological properties of mucus affect the synchronisation length scale. (a)** shows the sigmoidal curves of the inverse of the time constant as a function of the area of the DDM tile for samples from three healthy donors (top) and three CF donors (bottom), before and after mucus removal (respectively right and left). The coordination length scale squared λ^2 is measured as the left shoulder (vertical line, shaded area showing uncertainty) of the curve (continuous line) obtained fitting the experimental data (symbols).Each sigmoidal curve is built from at least 20 FOVs imaged across the sample. **(b)** Comparison of λ^2 for each sample revealed significant changes in the length scale of ciliary coordination following removal of the mucus ($p < 0.05$ and $p < 0.01$ for healthy and CF samples respectively. Paired, two-tailed Student's t-test comparing $\log_{10} \lambda^2$). CF samples are characterised by a higher synchronisation length scale than healthy samples. This difference could be due to different rheological properties of the mucus layer, as it is not apparent after washing the mucus.

exhibit lower beating frequency with respect to the healthy samples. This confirmed that mucus hinders the beating of cilia, and particularly so when the composition of the mucus layer is altered by the CFTR mutation.

4.5.2 Coordination of cilia beating in healthy and CF samples

We next assessed the degree of ciliary coordination in the CF samples in the presence of mucus and after a wash treatment. In Figure 4.5a we show the curves obtained plotting the reciprocal of the decay time of the Image Structure Function versus the size of the analysis tile, following the procedure described in section 3.4 and depicted in Figure 4.3. The position of the left shoulder of these sigmoidal curves (λ^2), that we use to measure a length scale of ciliary coordination, differs depending on the absence or presence of the mucus layer (Figure 4.5b):

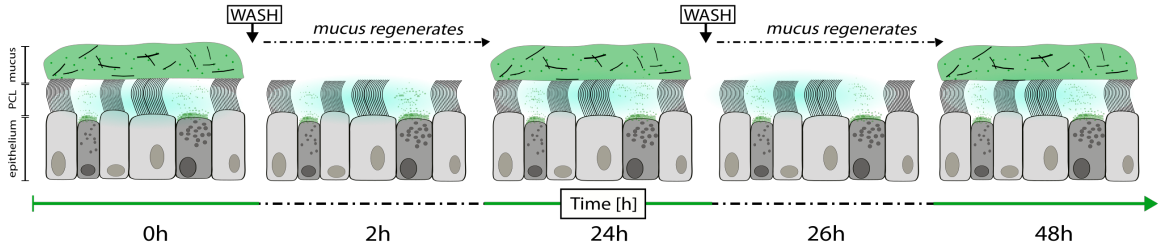

Fig. 4.6 **Repeated mucus washes.** In this experiment we repeatedly imaged samples from three subjects affected by CF in different mucus conditions. We first imaged the samples (0h) then proceeded to wash the mucus and imaged the samples again (2h). We imaged the sample again after allowing the sample to re-grow the mucus (24h), then washed and imaged (26h). Finally, we imaged the samples (48h) after allowing the mucus to reform for a second time.

Following a wash, the ciliary coordination length scale decreases towards values measured on healthy samples. We measured a statistically significant shift of λ^2 towards smaller values following the wash treatment ($p < 0.01$) in CF samples. This is also observed, albeit to a smaller extent, when mucus is removed from samples from healthy donors ($p < 0.05$, Figure 4.5b).

A decrease in the length scale of ciliary coordination means that cilia are worse coupled with their neighbours in absence of mucus. This implies that the mucus, acting like an elastic gel-like raft, helps cilia synchronising. This is consistent with our observation that, in presence of mucus, λ^2 is lower in healthy samples than in CF samples, where the mucus layer is thicker and its elastic modulus much higher [133, 145].

4.6 Repeated cycles of mucus wash/regrowth on Cystic Fibrosis ciliated epithelia

The experiments with multiDDM presented in section 4.5 compared the results of the analysis of different HAEC samples maintained under constant cell culture condition. While this is useful to convey information about the differences between the samples, it does not explore how the collective dynamics of cilia evolve over time in response to external stimuli. This is particularly relevant for understanding the response of the ciliated epithelium to pathogenic infections and/or pharmacological treatments. Having shown how the presence of mucus has a dramatic effect on both CBF and cilia coordination in section 4.5, we tested the effect of successive cycles of washing the epithelium and allowing the mucus layer to regenerate.

HAECs obtained from three different subjects (s1 to s3) affected by homozygous F508del mutation were subjected to successive rounds of mucus removal and regeneration over two

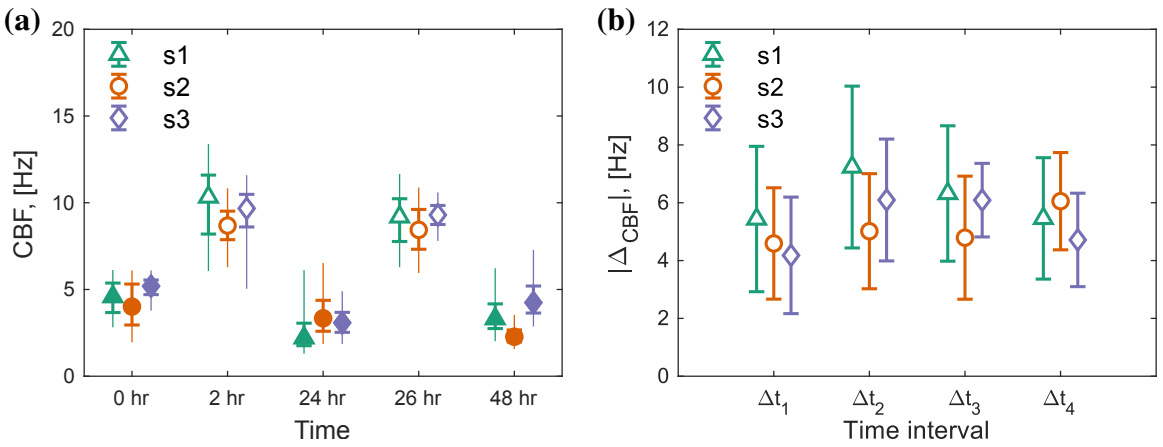

Fig. 4.7 **Mucus removal consistently increases CBF. (a)** shows how the CBF distribution of each subjects evolves over the different time points. Empty and full markers show whether the sample had just been washed or if the mucus layer had had time to regenerate. Markers show the median of each CBF distribution, the horizontal caps mark 25th and 75th percentile, and the thin lines 5th and 95th percentile. Each distribution was built from at least 20 fields of view imaged across each of the three samples. CBF constantly increases subsequently to a mucus wash, and decreases again upon the regeneration of the mucus layer. **(b)** The absolute value of the difference in CBF upon mucus wash/regrowth was consistent across the entire experiment and between different subject samples regardless of the time interval. The markers show the absolute value of the difference between the average of CBF distributions at consecutive time points, and the error bars the square root of the sum of their standard deviations squared.

days. As detailed in Figure 4.6, the samples were imaged in presence of mucus ($0\,\mathrm{h}$), shortly after the epithelium was washed ($+2\,\mathrm{h}$) and then again after the mucus had regenerated ($+24\,\mathrm{h}$). This cycle was repeated at $+26\,\mathrm{h}$ and $+48\,\mathrm{h}$. We observed a complete regeneration of the mucus layer, and consequently a compromised cilia beating, both after the first and the second wash.

4.6.1 Evolution of CBF upon repeated wash treatments

The DDM analysis provided a quantitative measure of the complete regeneration of the mucus layer, revealing cyclical changes in CBF over time (Figure 4.7): the average CBF was in the $2.4\,\mathrm{Hz}$ to $5.1\,\mathrm{Hz}$ range in the presence of mucus, and in the $8.4\,\mathrm{Hz}$ to $10\,\mathrm{Hz}$ range after a wash treatment. The change in CBF upon successive imaging time points is shown to be consistent (Figure 4.7b).

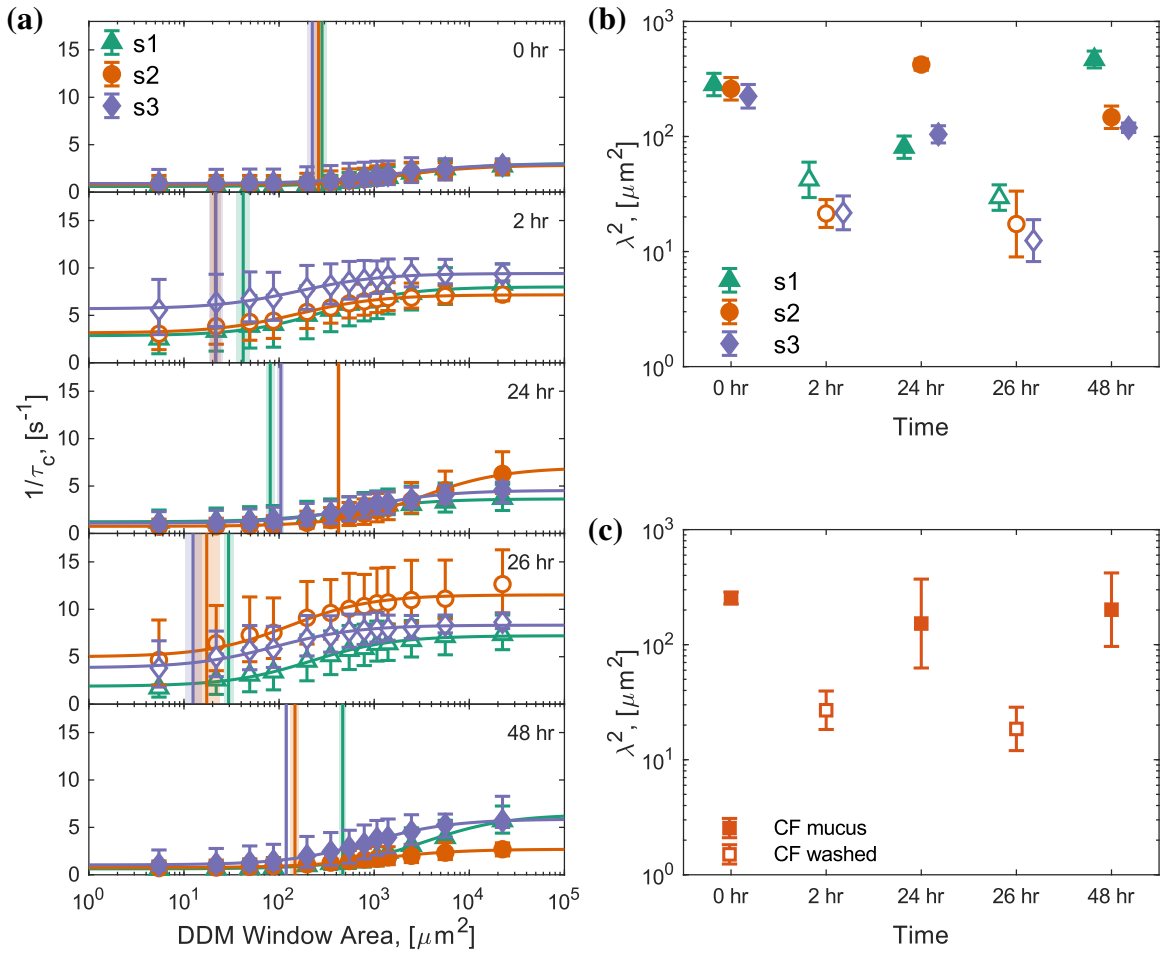

Fig. 4.8 **Mucus removal consistently decreases the length scale of coordination.** **(a)** shows the sigmoidal curve of the inverse of the time constant as a function of the area of the tile DDM was applied to. Experimental data points (symbols, error bars mark 25$^{\text{th}}$ and 75$^{\text{th}}$ percentiles), are fitted (continuous line) in order to find the square of the coordination length scale λ (vertical line, shaded region shows its uncertainty). **(b)** shows λ^2 as a function of time for each sample. Empty markers are used for data points collected when the mucus had just been washed, full markers if the mucus layer had had time to regenerate, and error bars show the uncertainty on λ^2. The length scale of cilia coordination consistently decreases after removing the mucus layer, and increases again after the mucus layer is regenerated. This can be appreciated also in **(c)** where we plot the geometric average of λ^2 across the three samples versus time (squares, with the error bar showing the geometric standard deviation).

4.6.2 Evolution of the length scale of cilia coordination upon repeated wash treatments

The sigmoidal curves generated by multiDDM show a similar cyclical behaviour as the CBF, as we show in Figure 4.8a. Consistent with the experiments presented in section 4.5 the

coordination length scale of cilia beating decreases upon removal of mucus, and increases again after the mucus layer has regenerated. This behaviour is highlighted if we plot λ^2 measured on each sample at each time point (Figure 4.8b, and the average across samples in Figure 4.8c). All measurements of the coordination length scale in presence of mucus cluster together, separately from values of λ^2 on freshly washed samples. We found a statistically significant difference in the values of λ^2 measured between each consecutive time point ($p < 0.05$, unpaired, two-tailed Student's t-test on $\log_{10} \lambda^2$). This results show how the progressive accumulation of mucus increases the length scale over which cilia lose the phase locking, and that multiDDM is particularly well-suited to measure this phenomenon.

4.7 Response of Cystic Fibrosis ciliated epithelia to CFTR-modulator drugs

Having demonstrated how multiDDM can measure changes in the CBF and spatial coordination of a ciliated epithelium, also in response to experimental variables, we now show how multiDDM can be used for screening and testing of therapeutic compounds for the treatment of respiratory diseases, or in general any condition affecting ciliary beat. In the experiment presented in this section we assess the effect of the three compounds detailed in section 4.3 on ALI samples from donors with the homozygous F508del mutation of the CFTR gene: VX809, VX809/VX770, and Tα1.

Four samples from each of the three CF donors were treated respectively with VX809, VX809/VX770, Tα1, and DMSO (for the control) as detailed in section 4.4.4. The samples were imaged at $0\,\mathrm{h}$, $24\,\mathrm{h}$, and $48\,\mathrm{h}$ into the treatment. The inserts were washed of mucus $48\,\mathrm{h}$ prior to the beginning of treatment.

4.7.1 CBF response to CFTR modulating drugs

CBF measurements on microscope videos taken at $0\,\mathrm{h}$, $24\,\mathrm{h}$, and $48\,\mathrm{h}$ into the treatment show an increase of CBF over time for samples treated with VX809 and VX809/VX770 (Figure 4.9a,b). This increase is highlighted by plotting the evolution of $\Delta_{CBF}(t)$, defined as the difference between the CBF measured at each timepoint and at $0\,\mathrm{h}$ (Figure 4.9c,d). While samples treated with Tα1 do not show an increase of CBF over time, they do show a less marked decrease in CBF over time than in the DMSO control, which becomes evident when plotting the difference between $\Delta_{CBF}(t)$ measured on the treated samples and on the control (Figure 4.9e,f).

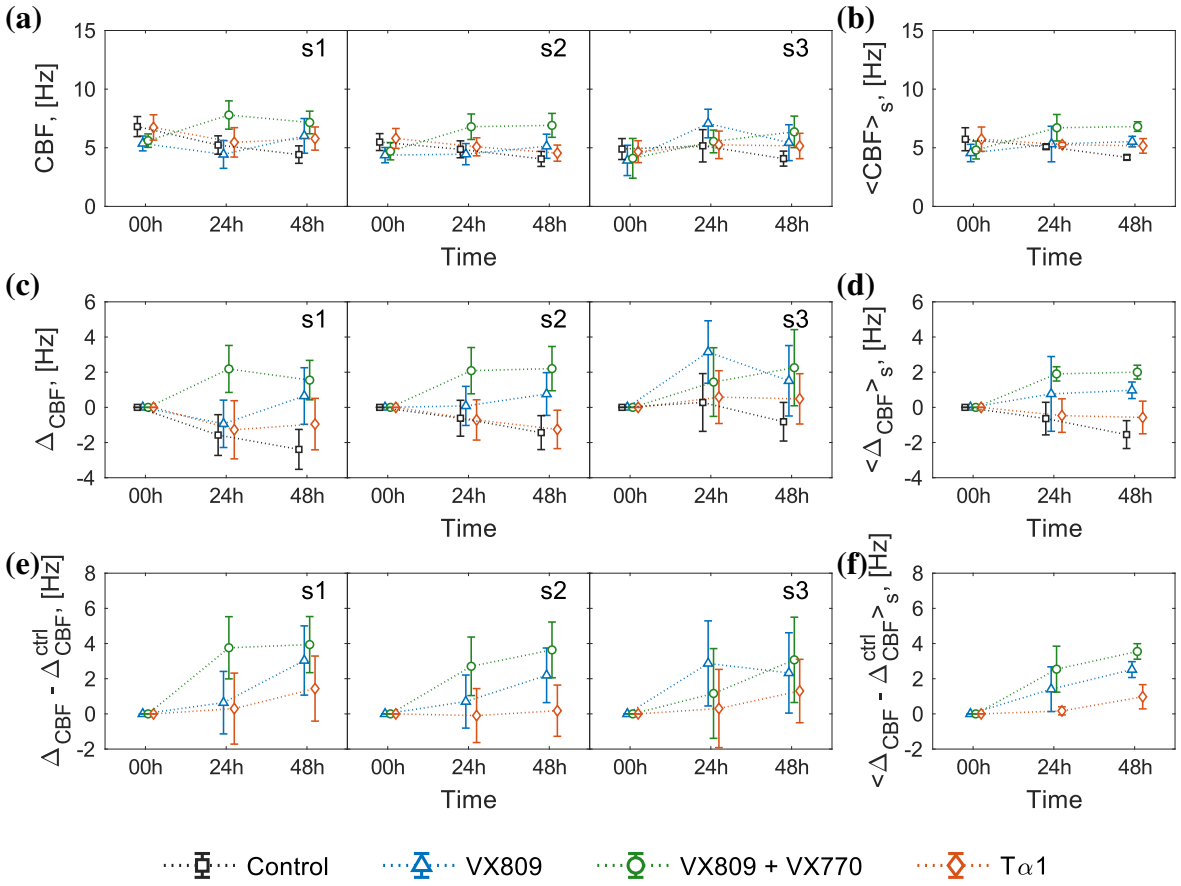

Fig. 4.9 **Effect of CFTR-modulating drugs on ciliary beat frequency.** **(a)** shows the evolution of CBF on each sample (s1 to s3, from left to right) versus treatment time. The error bars show mean $\pm$ standard deviation, while the dotted lines guide the eye. Each data point is built from at least 16 FOVs. The standard deviation here measures the spread in the distribution of CBF values within a single sample. **(b)** shows instead the time evolution of the average CBF across samples (the error bars showing the standard deviation of the samples' means). Trends in the data are easier to see in **(c)**, where we plot the difference in CBF after the initial time point $\Delta_{\mathrm{CBF}}(t) = \mathrm{CBF}(t) - \mathrm{CBF}(0\,\mathrm{h})$ for each sample, and **(d)** where we show the average across samples. While treatment with VX809 (blue triangles) and with VX809 and VX770 combined (green circles) show an increase in CBF over time, this is not the case for the control (black squares) or for the samples treated with Tα1 (orange diamonds). Tα1 is however reducing the decrease in CBF we see in control samples. This can be seen in **(e)**, where we plot the difference between the time evolution of CBF in each treated sample and their respective control sample, and in **(f)** where we plot the average across samples.

Among the compounds tested in the experiment presented in this section the combination of VX809 and VX770 affected the beat frequency the most, with an average increase in CBF compared to the control of $3.6 \pm 0.4\,\mathrm{Hz}$. In comparison, the treatment with VX809 alone

and Tα1 yielded an increase of CBF of respectively $2.5 \pm 0.5\,\mathrm{Hz}$ and $1 \pm 0.7\,\mathrm{Hz}$ compared to the DMSO control.

4.7.2 Length scale of ciliary coordination upon treatment with CFTR modulating drugs

MultiDDM allowed us to measure the length scale of cilia coordination on the samples treated with CFTR modulating drugs, thus extracting additional important information beyond the CBF.

By looking at the left shoulder point of the sigmoidal curve obtained as detailed in sections 3.4 and 4.4.5 we can see how, on average, the length scale of coordination increases with time in the control sample. This is expected, and consistent with the experiments reported in sections 4.5 and 4.6, as the mucus layer thickens over time (Figure 4.10a). On the other hand in all samples treated with CFTR modulating drugs we see either a decrease in the coordination length scale, or a smaller increase compared to the control sample (Figure 4.10). As we saw in sections 4.5 and 4.6 a reduction in the coordination length scale when compared to the CF phenotype is a shift towards healthy ciliary beating dynamics, especially when coupled with an increase in CBF.

Not all the CFTR modulating drugs cause the same amount of response in coordination length scale. In Figure 4.10b we show the relative change in λ^2 in each sample, normalised by the change in λ^2 measured on the relative control. Here we can see how, while all three compounds are effective in reducing the coordination length scale, Tα1 causes the most marked response. The same can be seen in Figure 4.10 where we show the relative change in λ^2 over time averaged across the three donors.

The data presented in this section make a compelling case for using multiDDM as a tool during screening for putative drugs: while samples treated with Tα1 only showed a marginal increase in CBF when compared to the control, they showed the most marked response in terms of the coordination length scale. The effectiveness of Tα1 would therefore be severely underestimated by only measuring the CBF of the samples.

4.8 MultiDDM is well suited to measure the response of ciliated epithelia to drug treatments

The ability to determine whether a given treatment has a positive therapeutic benefit on cells with different classes of CFTR mutations is of great value. Out of the nearly 2000 different mutations in CFTR, there are still many that, despite inducing Cystic Fibrosis, are

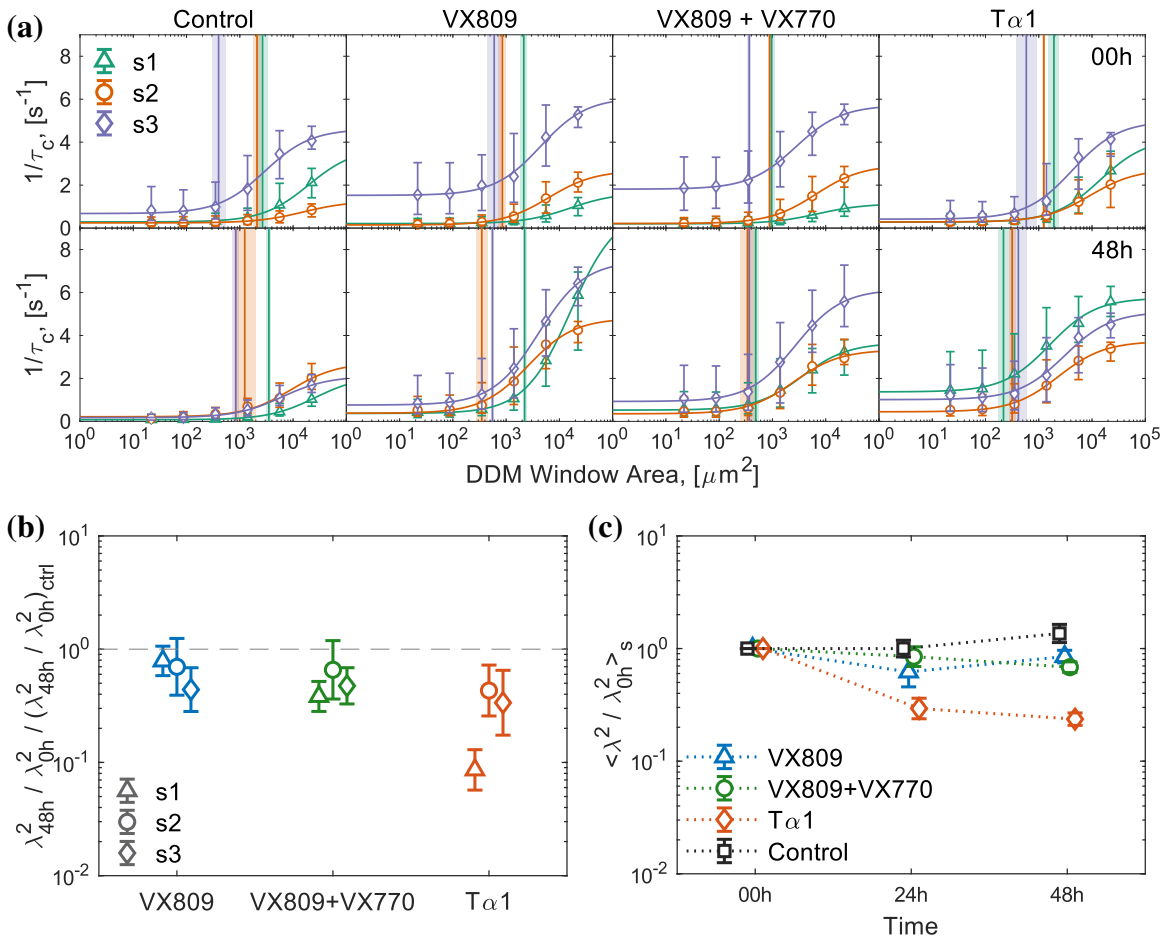

Fig. 4.10 **Effect of CFTR-modulating drugs on ciliary coordination.** Treatment with VX809, VX809 and VX770, and Tα1 not only increases CBF with respect to the control samples, but decreases the coordination length scale, similar to what was observed upon removal of mucus in Figure 4.5 and Figure 4.8. This can be seen in **(a)**, where we plot the sigmoidal curves of the reciprocal of the DDM time constant as a function of the area of the analysed window, at the start of the experiment and after $48\,\mathrm{h}$ of treatment. The vertical line is the coordination length scale squared λ^2 (shaded region marking its uncertainty), measured as the shoulder of the sigmoid (line) obtained fitting the experimental data (markers and whiskers showing median and 25$^{\text{th}}$ and 75$^{\text{th}}$ percentile). **(b)** shows the ratio between λ^2 measured at $48\,\mathrm{h}$ and $0\,\mathrm{h}$ for each subject and treatment separately, normalised by the same λ^2 ratio measured on the control. All data points are below 1 (dashed grey line). For each treatment, every subject showed an improvement in ciliary coordination relative to the control at the same time point. **(c)** The time evolution of the length scale of ciliary coordination showed the greatest response to Tα1, as determined by the ratio between $\lambda^2(t)$ and the initial $\lambda^2(t = 0\,\mathrm{h})$ geometrically averaged over the three donors (whiskers mark the geometric standard deviation) against time.

rare, uncharacterised, and have not been tested for their responsiveness to clinically available CF drugs.

MultiDDM could be a powerful tool to test the efficacy of CFTR modulating drugs, and has several key points to that regard. First, it is based on primary HAECs grown at ALI, which is a relatively simple cell culture method widely used amongst clinicians. Application of multiDDM to assess putative drug treatments would require the culture of HAECs isolated from the subject and application of multiDDM analysis before and after the treatment, which is quite straightforward. Furthermore, and unlike current techniques for analysis of ciliary beating, multiDDM is automated, reducing the need for trained technicians and removing a possible human bias. Finally, multiDDM considers not only CBF but also the spatio-temporal coordination of cilia beating across the entire FOV. This is an important point, as it yields important information regarding collective cilia beating and fluid transport in a clinically-relevant setting.

The analysis of cilia beating beyond the simple CBF is critical in order to gain a more complete picture of how different candidate drug treatments affect mucociliary clearance. An example of this is the data collected on HAECs treated with Tα1, where despite only a modest improvement in CBF with respect to the vehicle-only control we observed a marked improvement in cilia coordination, even greater than that seen in response to the combination of VX-770 and VX-809.

MultiDDM could enrich the tool set available to clinicians in multiple ways. Firstly, it should now be possible to characterise the effect of a wide range of putative CF-treating drugs on HAECs, measuring changes in ciliary beating and coordination over time and respect to a control. *In vivo*, mucociliary clearance is mediated by the beating of thousands of cilia in a coordinated fashion, therefore a quantitative measurement of ciliary coordination would be suited to the testing of drugs that modulate MCC. In particular, it would be useful for those drugs such as mucus hydrators and DNAses/mucus disruptors that do not alter CFTR function and so cannot be tested using a Ussing chamber nor the Forskolin-induced swelling assay [146–148].

A second possible application for multiDDM is in testing CFTR-modulating drugs, as a complementary option to the Ussing chamber assay [146, 147]. Theoretically, restoration of CFTR ion channel function as measured via Ussing chamber should lead to mucus rehydration and increased MCC. However the relationship between the Ussing chamber results and the observed clinical response is not always clear, and the degree of rescued CFTR activity varies across patients. It would be useful to employ multiDDM as an additional step to quantify the response of samples to treatment with a putative drug.

An additional application of multiDDM is to investigate ciliary beating dynamics in diseases other than CF, such as in ciliopathies, where over 187 genes have been associated with a defect in cilia form or function [149]. Characterising ciliary beating in terms both of CBF and coordination in different ciliopathies and in the different tissues affected will help to better understand this broad class of diseases, possibly leading to better diagnostic tools.

4.9 MultiDDM can be a valid help to clinicians

Probing the collective cilia beating dynamics and mucociliary clearance across cells at ALI with multiDDM provides a direct quantitative phenotyping of cilia function and represents a new approach to determine the coordination of cilia and their efficiency in propelling mucus. MultiDDM is not limited to the estimation of the CBF in ALI culture, but crucially also gives information about the coordination and the spatio-temporal correlation of the ciliary beating as well. The ability of multiDDM to probe cilia coordination is key in the study presented in this chapter.

First, we showed how the length scale of cilia coordination is lower in epithelia from healthy samples than from CF samples, as (we hypothesise) the mucus layer acts as an elastic gel raft coupling cilia beating. This difference disappears upon removing the mucus layer, strengthening our hypothesis about the role played by the mucus.

We then checked that the increase in length scale of coordination upon formation of the mucus layer was reproducible by imaging a sample that underwent multiple cycles of mucus wash and re-growth. This experiment confirmed that the length scale of coordination we measure is higher in the presence of the mucus layer.

Lastly, we performed a proof-of-concept work to show how this technique could be used to help gather more information towards a diagnosis. We treated samples from patients affected by the homozygous F508del mutation to the CFTR gene with a CFTR corrector, a combination of CFTR corrector and potentiator, and an anti-inflammatory drug that also rescues CFTR functionality [126], and tracked the temporal evolution of ciliary coordination. We were able to detect an improvement on the condition of the samples upon treatment, to different degrees according to the the type of treatment (as expected). This improvement could be seen as in all samples the treatments lower the length scale of ciliary coordination (compared to a vehicle-only control), thus moving the sample towards a healthy phenotype.

In conclusion, the study presented in this chapter shows how multiDDM can be at the foundation of a straightforward, quantitative assay to characterise and detect changes in ciliary beating and coordination in ciliated epithelia. This can be used, for example, to assess patient responses to putative and existing drug treatments for CF, and may be applied to

CFTR-modulating and non-CFTR-modulating drugs alike. MultiDDM improves on previous methods of ciliary beat analysis in that it is unbiased and automated, and because it captures the spatio-temporal coordination of collective cilia beating which is crucial for mucociliary clearance, and not simply the CBF.

Finally, since multiDDM is ultimately a means to assess cilia beating dynamics, its use is not limited to CF samples, but may be applied to other diseases in which ciliary beating is affected. Application of multiDDM is in fact not limited to human ciliated epithelia at the Air-Liquid interface: it can be deployed to characterise any ciliated epithelium that can be imaged with a microscope and, more generally, any sample that shows multi-scale dynamics.

Chapter 5

Studying Ciliary Beating Pattern to profile Phenotypes of Ciliopathies

5.1 A closer look at the scale of cilia

Studying the motion and coordination of cilia is a feat that needs to be accomplished by investigating different length scales. As discussed in the introduction, our long-term hypothesis and quest is to verify how the macroscopic state depends on the microscopic (single cilium and arrangement) properties.

MultiDDM, that we extensively presented in chapter 3 and tested out in chapter 4, is a very powerful tool for characterising a ciliated epithelium on a large length scale (hundreds of micrometers), being able to measure the distribution of CBF, find metachronal waves, and measure how the phase-locking among cilia is lost over distance. Being such a complete tool, multiDDM can be used to study how ciliated epithelia respond to external stimuli, in particular changes in the mucus rheology (chapter 4).

This chapter treats instead how we approached the task of investigating smaller length scales (tens of micrometers), at the level of waveforms and beating of individual cilia. This is a level of great interest to biologists and clinicians, to understand the way individual cilia assemble and function, and what goes wrong in various genetic diseases. Of course, ultimately, the questions of dynamics at the cilia and inter-cilia scales will need to be addressed jointly.

First, we devised a way to image cilia beating from the side (Figure 5.1), obtaining high speed microscopy videos of very good quality (example frames in Figure 5.2). We then tried two different approaches to analyse the microscopy videos: First, inspired by [59] we attempted to use Particle Image Velocimetry (PIV). PIV proved soon to not be the most appropriate technique to analyse this type of video: cilia have poor contrast, and their contrast

changes in sign as they cross the focal plane. More importantly, given the finite depth of focus of the objective, the microscopy videos show background cilia moving out of phase from cilia in the foreground, potentially leading to an underestimation of motion between frames. Given the shortcomings of PIV on this particular system (more details about this path of analysis are given in Appendix C), we eventually settled for a lower-throughput, more laborious, but more reliable type of analysis, focused on resolving the beating pattern of the single cilium. Here we present such single-cilium-oriented analysis, and we apply it to the characterisation of the beating pattern of cilia both from healthy donors and from patients affected by two variants of Primary Ciliary Dyskinesia. This study was conducted in collaboration with Dr Maurizio Chioccioli, and the groups of Dr Vito Mennella (The Hospital for Sick Children, Toronto, Canada) and of Dr Max Seibold (National Jewish Health, Denver, Colorado, USA).

5.2 Primary Ciliary Dyskinesia

Primary Ciliary Dyskinesia (PCD) is an umbrella term for a phenotypically and genetically heterogeneous disease characterised by abnormal ciliary function. Whilst the structural molecular biology of motile cilia is well understood, the way individual proteins interact to create the reproducible motion that is the ciliary beat pattern (CBP), and how this can adapt to external cues, are still open questions [150, 151].

Given the structural and molecular complexity of motile cilia it is not surprising that PCD has complex genetics, and effects spanning both ciliogenesys and function. So far 37 genes have been shown to be linked to PCD [149], although this was estimated to only represent about $70\,\%$ of all cases [39] The vast majority of PCD cases [152] stem by ultrastructural defects that hinder the function of either the inner, the outer, or both dynein arms, which are the molecular motors that make ciliary motility possible.

5.2.1 PCD variants: DNAH11 and HYDIN

Recently a lot of effort has been put into mapping the genetic defects onto the defects in cilia ultrastructure, however up to $20\,\%$ of PCD cases do not show any ultrastructural defects, but still exhibit abnormal motility [101, 153–156]. An example of a PCD variant with no apparent ultrastructural defect is the one caused by mutations in the dynein axonemal chain 11 (DNAH11) protein. Despite the ciliary ultrastructure being normal, inspection via high speed video microscopy (HSVM) reveals aberrant beating pattern [157–159].

Other PCD variants are characterised by ultrastructural defects so subtle that they can be difficult to detect with standard diagnostic techniques, putting patients at risk of being

misdiagnosed [160, 161]. Mutations in the protein HYDIN, for example, cause a PCD variant in which the CBF is reportedly normal, there are no *situs* anomalies, defects in the axonemes are only rarely seen under transmission electron microscopy (TEM), but the beat pattern is abnormal.

5.2.2 High Speed Video Microscopy for the diagnosis of PCD

Together with the evaluation of the clinical presentation, measurements of nasal nitric oxide levels, transmission electron microscope, genotyping, and immunofluorescence, HSVM is one of several approaches used to characterise PCD, as it allows to record and investigate the ciliary beating pattern [101]. CBP has been linked to particular variants of PCD and/or types of ultrastructural defects [98, 153], however HSVM analyses have so far mostly been qualitative. A more rigorous analysis is needed to characterise fully the parameters of the beating pattern, as these can affect the way cilia synchronise and how successful mucociliary clearance is [32]. A quantitative approach to the analysis of the CBP is thus essential in order to map the genetic mutations onto the variety of defects in cilia motility, and would also help improving diagnosis of PCD, particularly in the case where known genetic mutation or ultrastructural defects are not detected.

5.3 Methods for single cilium analysis

Most of the high speed microscopy videos analysed in this chapter were supplied by the group of Dr Vito Mennella, in The Hospital for Sick Children, Toronto, Canada. In particular, all videos featuring samples affected by PCD were provided by Dr Mennella, together with about half of the healthy control videos presented in this chapter. The remaining half of the healthy control videos were recorded (on samples kindly provided by Dr Max Seibold, NJH, Denver, CO, USA) by me in collaboration with Dr Maurizio Chioccioli, who also performed the first step of the analysis detailed in section 5.3.2 (in particular, the initial tracking of the cilium and the identification of the cell surface).

5.3.1 Culture and imaging of nasal epithelial cells

Samples were isolated from healthy subjects and subjects with PCD (mutations in DNAH11 or HYDIN) as follows. Human primary nasal airway cells were collected from healthy and PCD patients (HYDIN and DNAH11 mutants) with a cytology brush by an experienced nurse at the Hospital for Sick Children. The protocol was approved by Sickkids Ethics Committee. Airway cells were plated on collagen-coated (PurCol, Bovine Collagen Type I,

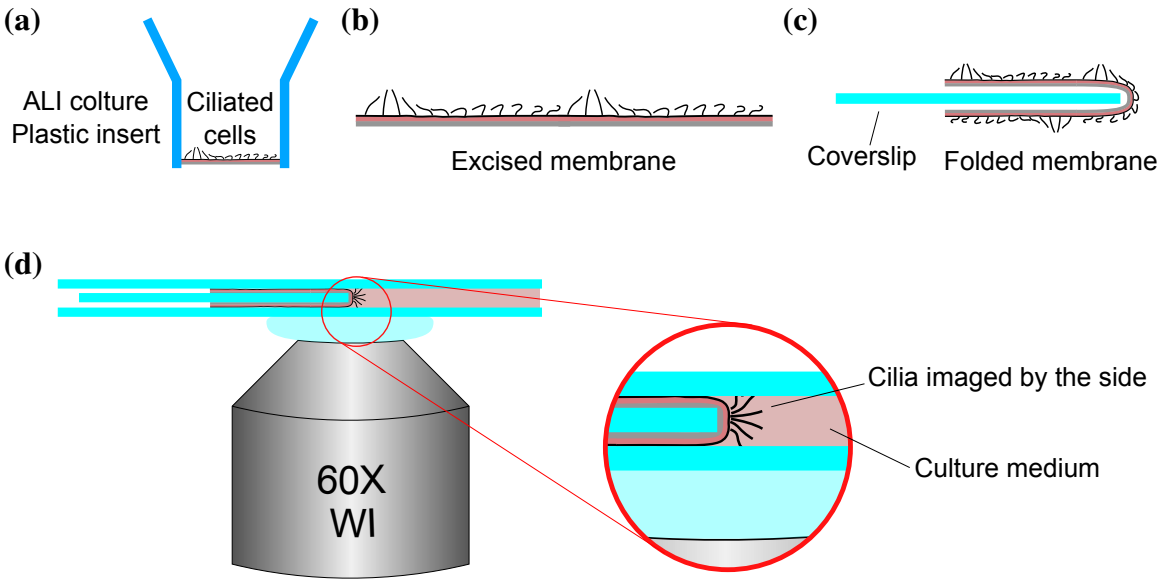

Fig. 5.1 **Imaging cilia from the side.** The plastic insert **(a)** for ALI culture can be manipulated to image the cilia from the side, so to see their beating pattern. First, the porous membrane that supports the ciliated epithelium needs to be carefully excised and removed from the plastic insert **(b)** without damaging the supported epithelium. The membrane is then folded around a glass coverslip **(c)**, and sandwiched with a few µl of medium between two other glass coverslips **(d)**. The imaging chamber thus formed is then placed on an inverted microscope and imaged, as detailed in section 5.3.1.

Advanced BioMatrix) T-25 Primaria flasks (Corning) with PneumaCult-Ex Medium (Stem Cell Technologies) supplemented with ROCK Inhibitor ($5\,\mu$M; Y-27632; Enzo Life Sciences) and hydrocortisol solution ($96\,\mathrm{ng/ml}$; Stem Cell Technologies). Under these conditions, basal (stem) cells were then expanded, seeded on transwells (Corning HTS Transwell-96 and -24 permeable support; $0.4\,\mu\mathrm{m}$ pore size), and differentiated following Stem Cell Technologies protocols using PneumaCult-Ex and PneumaCult-ALI media. This differentiation process spanned over a minimum 35-days period. PneumaCult-Ex and -ALI media were supplemented with the following antibiotics: Vancomycin ($100\,\mu\mathrm{g/ml}$; Bioshop Canada Inc), Tobramycin ($80\,\mu\mathrm{g/ml}$; Bioshop Canada Inc), Gentamicin ($50\,\mu\mathrm{g/ml}$, Thermo Fisher Scientific) and Antibiotic-Antimycotic (1 X; Thermo Fisher Scientific). Human primary nasal cells were cultured at $37\,^{\circ}\mathrm{C}$ with $5\%\,CO_2$. Cilia from each sample type were imaged by placing the filters cell-side down on a 1.5 round coverslip mounted on a holder. HSVM (500 frames per second; 8s videos) was performed using spinning disc confocal microscopy for a total of one (healthy), two (DNAH11) and two (HYDIN) samples. This was conducted in Dr Mennella's lab in Toronto.

The remaining 6 tracked cilia from two healthy donors were instead imaged in house on a Nikon Eclipse Ti-E inverted microscope (Nikon, Japan), equipped with a $60\times$ water immersion objective ($\mathrm{NA} = 1.2$, Nikon, Japan) and a further $1.5\times$ magnification in the optical path ($1\,\mathrm{px} = 0.065\,\mu\mathrm{m}$). The high speed videos were acquired with a CMOS camera (GS3-U3-23S6M-C, FLIR Integrated Imaging Solutions Inc., Canada).

To image the beating cilium from the side, we excised the bottom membrane of the plastic insert supporting the cell epithelium, very carefully folded it around a coverslip, and finally sandwiched, together with some culture medium, between two more coverslip before placing it onto the microscope. This protocol, depicted in Figure 5.1, allowed us to image the cilia on the folded edge.

5.3.2 Tracking and reconstruction of the cilium shape

The protocol detailed in section 5.3.1 yields good quality videos of cilia beating approximately in the focal plane of the microscope. Each ciliated cell has about 200 to 300 cilia [70], and as the cilia move slightly above or below the focal plane their contrast change from positive to negative [162]. Trying to automatically track individual weakly scattering objects of changing contrast in a field of view crowded with extremely similar other objects proved to be too challenging a feat.

I developed a user interface in MATLAB to aid in manually tracking the cilium position over time, and then extracting its evolving mathematical shape. In each pre-recorded frame, the user clicks P points along the cilium shape (with, on average, $P = 7$), obtaining P couples of coordinates (X_i, Y_i), with i being an index that grows from 1 to P from the base to the tip of the cilium. These points need not be exactly evenly spaced. An example is in Figure 5.2a. Cilia clicking was performed by M. Chioccioli on these datasets.

My analysis software then reconstructs a smooth representation of the cilium by fitting the coordinates of the clicked points with two 4$^{\text{th}}$ degree polynomials. First, we measure the Euclidean distance between subsequent couples of points $D_j = \sqrt{(X_j - X_{j-1})^2 + (Y_j - Y_{j-1})^2}$. We then define the parameter S_i, corresponding to the coordinates (X_i, Y_i), as the sum of all the Euclidean distances between the base and the i-th point: $S_i = \sum_{j=1}^{i} D_j$, with $S_1 \coloneqq 0$. The discrete series of data points $[(S_1, X_1), \ldots, (S_P, X_P)]$ and $[(S_1, Y_1), \ldots, (S_P, Y_P)]$ are then fitted with two 4$^{\text{th}}$ degrees polynomials A and B so that $X_i = A(S_i) = \sum_{k=0}^{4} a_k\, S_i^k$ (and likewise Y_i). A much smoother representation of the cilium can then be obtained by evaluating the polynomials on s, a finely spaced variable ranging from 0 (at the base of the cilium) to S_P (at the distal end), resulting, for each frame, in a parametric representation of the cilium as $(x(s), y(s))$, where $x(s) = A(s) = \sum_{k=0}^{4} a_k\, s^k$ and $y(s) = B(s) = \sum_{k=0}^{4} b_k\, s^k$ (Figure 5.2b-e).

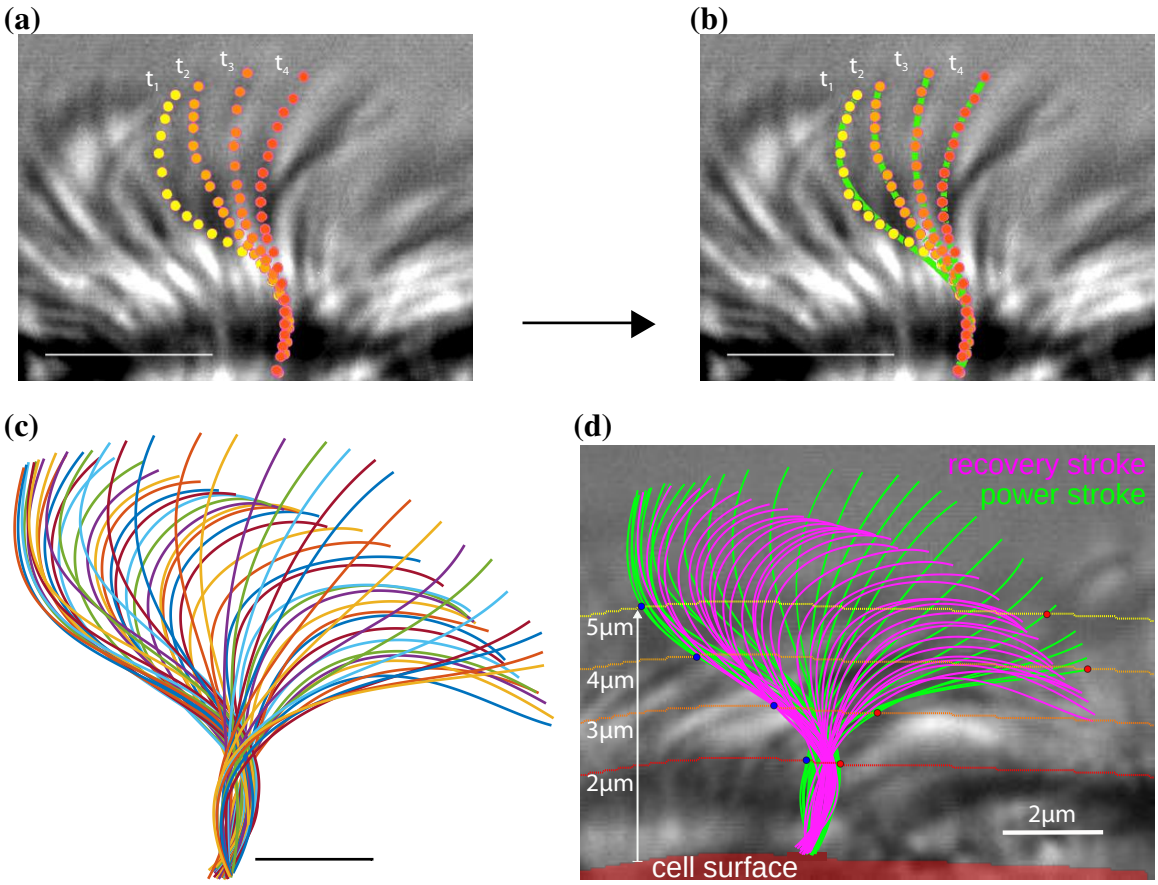

Fig. 5.2 **Reconstructed cilia beating pattern.** To build a smooth function that approximates the shape of the cilium over time we first manually track **(a)** the cilium at different timepoints ($t_1 - t_4$, series of dots) and then interpolate the x and y coordinates of each of the series of points with two 4^{th} degree polynomials **(b)** (green lines), as detailed in section 5.3.2. Scale bars are $5\,\mu\text{m}$. **(c)** shows the reconstructed beating pattern of a single cilium from a healthy patient. Scale bar is $2\,\mu\text{m}$. We then measure the amplitude of the beating pattern at different distances from the cell surface as **(d)** the distance between the intersection points of the cilium with each measuring line that are further apart from each other.

5.3.3 Amplitude and velocity of the ciliary stroke

Having found a smooth representation for the cilium shape at each timepoint, we measure several parameters, explained in this and the following sections. The first two of such parameters are the amplitude of the beating stroke and the average velocity during the power and recovery stroke, typically at different distances from the cell surface.

Still in a custom user interface the user creates a binary mask that closely follows the cell surface. Example of such masks can be seen in Figure 5.2d. The measuring line, for example at a distance h from the cell surface, is found by performing a dilation of the binary mask using a disk of radius h and taking the edge of the dilated mask. The data presented

in this chapter were analysed for amplitude and velocity at 2, 3, 4, and $5\,\mu\mathrm{m}$ from the cell surface (Figure 5.2d). The amplitude of the cilium beat at distance h from the cell surface is measured as the distance between the intersection points of the cilium with the measuring line that are further apart from each other (highlighted in Figure 5.2d).

By taking the intersection points of the cilium in two consecutive frames and measuring the distance between them, and dividing it by the time interval, we measure the instantaneous values of velocity. We then average all velocities measured on displacements towards the power stroke direction ("power stroke velocity") and, separately, towards the recovery stroke direction ("recovery stroke velocity").

5.3.4 Local curvature of the cilium

In each frame, the unsigned curvature of the cilium approximated by the parametric curve $(x(s), y(s))$ is measured as

$$\kappa = \frac{|x'y'' - y'x''|}{(x'^2 + y'^2)^{3/2}},$$

where the derivatives are in the parameter s. To be able to average the curvature across different tracked cilia we express the curvature as a function of the relative length of the cilium, a variable that ranges from 0 (base of the cilium) to 1 (distal end). As the cilium beats its tip moves in and out the focal plane, and is therefore hard to track consistently. To normalise the cilia length we discard very short regions of some tips, assigning the value "1" to the length of the reconstructed cilium that was the shortest during the beating cycle. Cilia shape can sometimes not be determined in some few frames, but we are able to retain analysis of the video as a whole by reconstructing the cilium shape in the missing frame by interpolating the coefficients of the two 4^{th} degrees polynomials $(x = A(s), y = B(s))$ between the previous and following frames, i.e. assuming that the shape of the cilium changes smoothly over time. To address the possibility that using polynomials to reconstruct a smooth mathematical model for the cilium shape might lead to overestimating the curvature at the proximal and distal end of the cilium, we tracked and reconstructed 9 immotile cilia, and measured their curvature along the length of the cilium. We then subtracted the curve obtained averaging across the immotile cilia from each of the active cilia's curvature curves.

5.3.5 Force exerted by the cilium

Resistive Force Theory (RFT) allows us to measure the force exerted by the cilium on the surrounding fluid, based on the method described in [52] and depicted in Figure 5.3.

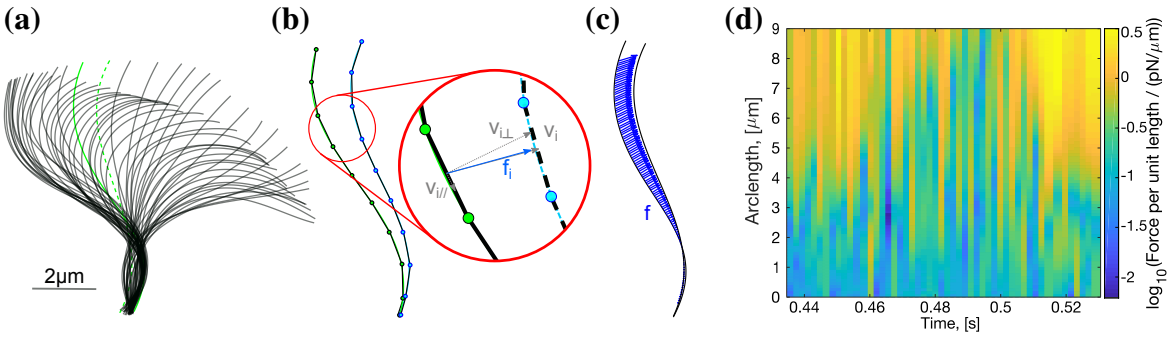

Fig. 5.3 **The force the cilium exerts on the fluid can be estimated by its beating pattern.** By tracking the cilium over time **(a)** and employing Resistive Force theory we can estimate the force exerted by the moving cilium on the surrounding fluid. Consecutive snapshots of the cilium are divided into a series of cylinders approximately $1\,\mu\mathrm{m}$ long. A few non-overlapping cylinders are shown **(b)** as an example. From the velocity at which each cylinder moves we can calculate the force it exerts on the surrounding fluid (details in section 5.3.5). The local force density can thus be measured along the cilium **(c)** and throughout a beating cycle **(d)**.

To measure the force exerted in the time between two frames, first we approximate the reconstructed snapshot in each of the two frames with a series of cylinders about $1\,\mu\mathrm{m}$ long. We then measure the displacement $\Delta\mathbf{r}_i$ of the midpoint of each cylinder between the two frames along the direction parallel and perpendicular to the cylinder itself. We can then define the velocity the cylinder moved at as the ratio between its displacement and the time interval between the two frames.

Given the velocity of the i-th cylinder as $\mathbf{v}_i = \mathbf{v}_{i\parallel} + \mathbf{v}_{i\perp}$, thanks to RFT we can find the force the cylinder exerts on the fluid as

$$\mathbf{f}_i = \mathbf{f}_{i\parallel} + \mathbf{f}_{i\perp} = \left(c_\parallel \mathbf{v}_{i\parallel} + c_\perp \mathbf{v}_{i\perp}\right) l_i,$$

where l_i is the length of the i-th cylinder. The two constants

$$c_\perp = \frac{8\pi\eta}{1 + \log l^2/a^2} \text{ and } c_\parallel = \frac{4\pi\eta}{-1 + \log l^2/a^2}$$

have the units of viscosity and are the drag coefficients of a slender cylinder of length l and radius a. The total force is then found by integrating the force contributions of all the cylinders, taking into account overlapping cylinders.

It is worth noting that this approach only represents a first approximation for our system, as it holds for Newtonian fluids of viscosity η. For the purposes of the analysis presented in this work we used $\eta = 1\,\mathrm{mPa\,s}$. In general however the fluid surrounding the beating cilium can typically be non-Newtonian. The approximation also assumes that the individual cylinder segments are in an unbounded fluid.

5.4 Differentiating between healthy samples and PCD variants

In order to obtain quantitative data on the ciliary beating in HAECs obtained from healthy subjects as well as subjects with PCD, specifically with mutations in DNAH11 and HYDIN (see Fig. 1 and Supplementary methods) we analysed a series of high speed microscopy videos imaging the cilia from the side as detailed in section 5.3.

The reconstructed waveforms for each of the three different conditions are strikingly different, with the most obvious difference being the severely restricted beating amplitude and curvature of the cilium in cells with mutations in either DNAH11 or HYDIN, compared to healthy cells. This is consistent with qualitative data previously reported for these mutations [153, 158, 163]. However, the reconstructed beating pattern also differs between the HYDIN and DNAH11 mutant HAECs: the beating amplitude of the DNAH11 mutant cilia is slightly reduced compared to that of HYDIN, and the curvature appears to be more pronounced. While the reconstructed beating patterns give an excellent overall impression of the differences in the ciliary beating phenotype, they do not yield by themselves any quantitative information into the parameters that drive mucociliary clearance nor how these are affected in the PCD. In order to obtain these data, further processing is required.

5.4.1 Amplitude and velocity of the cilium beat cycle

Reconstructing the cilium shape over time allows us to measure the amplitude of the beating pattern at increasing distances from the cell surface, as detailed in section 5.3.3. As shown in Figure 5.4, the beat amplitude of the cilia increases with a roughly linear dependence on the distance from the cell surface, but, as expected, there is a striking difference between cilia from healthy and PCD samples as healthy cilia sweep a much wider region than PCD cilia. This is captured by the much higher gradient of the healthy data in the amplitude vs distance from cell surface plot. The two variants of PCD differ from each other as well, the beat in HYDIN cilia being approximately twice as ample as in DNAH11. These quantitative data are consistent with descriptions of reduced ciliary beating amplitude previously reported for both the DNAH11 and HYDIN mutant forms of PCD [158, 163].

A measure of the linear velocity of the beating cilium at increasing height is obtained as detailed in section 5.3.3 from the distance travelled across two frames by the intersection point of the cilium with the measuring line. Trivially, the velocity increases with the distance from the cell surface, and we found it to be overall lower in PCD cells compared to healthy cells (Figure 5.5). We next considered whether we could measure a difference between the

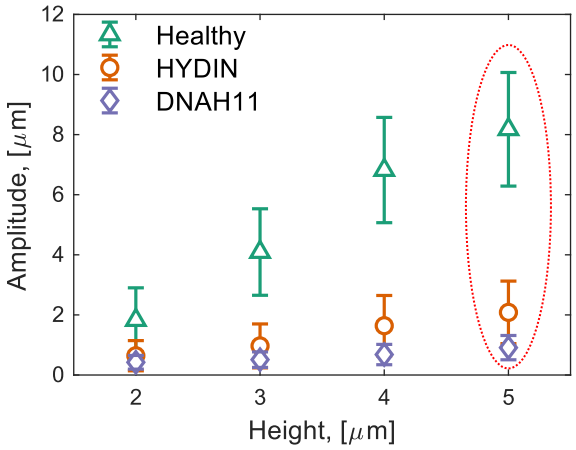

Fig. 5.4 **PCD reduces amplitude of beating pattern.** The average amplitude increases roughly linearly with the increasing distance from the cell surface, with healthy samples showing a much wider stroke compared to HYDIN and DNAH11 mutations. The beating amplitude at $5\,\mu\mathrm{m}$ from the cell surface (red dotted oval) is one of the parameters used to build a "barcode" for the Principal Component Analysis reported in section 5.4.4.

velocity of the power and recovery stroke, and if so, how this evolved at increasing distance from the cell surface. As we show in Figure 5.5 healthy beating cilia exhibit a higher average velocity of the power stroke relative to the recovery stroke, as expected. This is however not the case in the PCD samples: In the HYDIN mutant cells, our data show no detectable difference between the average velocity of the power and recovery stroke at any distance along the cilia. In the DNAH11 mutant cells, the average velocity of the power stroke is higher only at the most distal measurements ($4\,\mu\mathrm{m}$ and $5\,\mu\mathrm{m}$), whereas at the proximal end there appears to be no difference (Figure 5.5). Thus, while we can measure a distinct difference in the velocity of the power and recovery strokes in healthy beating cells, much or all of this difference is lost in cilia from PCD patients with mutations in either DNAH11 or HYDIN.

5.4.2 Curvature of the cilium evolves along the arc length and across the beat cycle

We can measure the local curvature along the reconstructed cilium using eq. (5.3.4) during the entire ciliary beat cycle, and create kymographs that show how the curvature evolves along the cilium and throughout a beating cycle. A few examples are in Figure 5.6, where we show the evolution of the local curvature along the cilium and over time on representative reconstructed cilia from healthy, HYDIN, and DNAH11 samples. In healthy cilia we can see how the kymograph of the curvature shows very obvious patterns in space and time, indicating travelling waves of curvature along the cilium (Figure 5.6a). In contrast to healthy

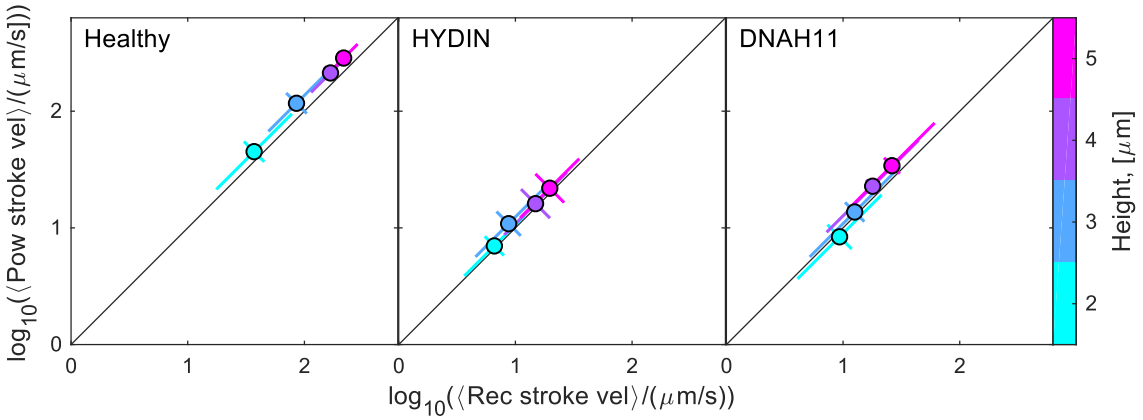

Fig. 5.5 **There is no significant difference in cilium velocity between the power and recovery stroke in PCD samples.** We measure the velocity of each cilium at different distances from the cell surface by dividing the distance between intersection points between the measuring line and the cilium reconstructed at consecutive time points by the time interval. We then average between all the values of velocity in the direction of the power stroke, and all the ones in the direction of the recovery stroke. By plotting the velocity of the power stroke on the y-axis, and of the recovery stroke on the x-axis, it becomes easy to see both a difference between the two velocities (points depart from the $y = x$ line, on the side of the higher velocity) and a general increase in the total velocity of the cilium (lower velocities will be shown as data points closer to the origin of the axes, higher velocities will be shown further from the origin). Here we plot the average (markers) across data points measured on the different tracked cilia at the same distance from the cell surface (increasing from cyan to magenta). The error bars show the standard deviation in the direction parallel and perpendicular to the $y = x$ line (black). This was done because the points averaged formed an elongated cluster oriented along the $y = x$ line. While in the healthy samples the power stroke is on average faster than the recovery stroke, this difference is much less marked in DNAH11 samples and lost in HYDIN samples.

cells, beating cilia from either the DNAH11 or the HYDIN PCD variants do not show distinct, obvious patterns of dynamic curvature. The representative kymographs in Figure 5.6b,c show that the overall curvature is low in both variants, although with some differences: the kymograph for the HYDIN cilium shows a region of extremely low curvature centred at mid-length, while the DNAH11 kymograph is characterised by low, constant curvature in the middle section of the cilium. Finally, the kymographs of the curvature in PCD variants do not highlight an obvious lag-phase - the pause between the end of the power stroke and the beginning of the recovery stroke - unlike in healthy samples (Figure 5.6a).

While the curvature kymographs in Figure 5.6 are informative, they only each represent a single cilium. We analysed cilia from different cells from each of the three genetic background

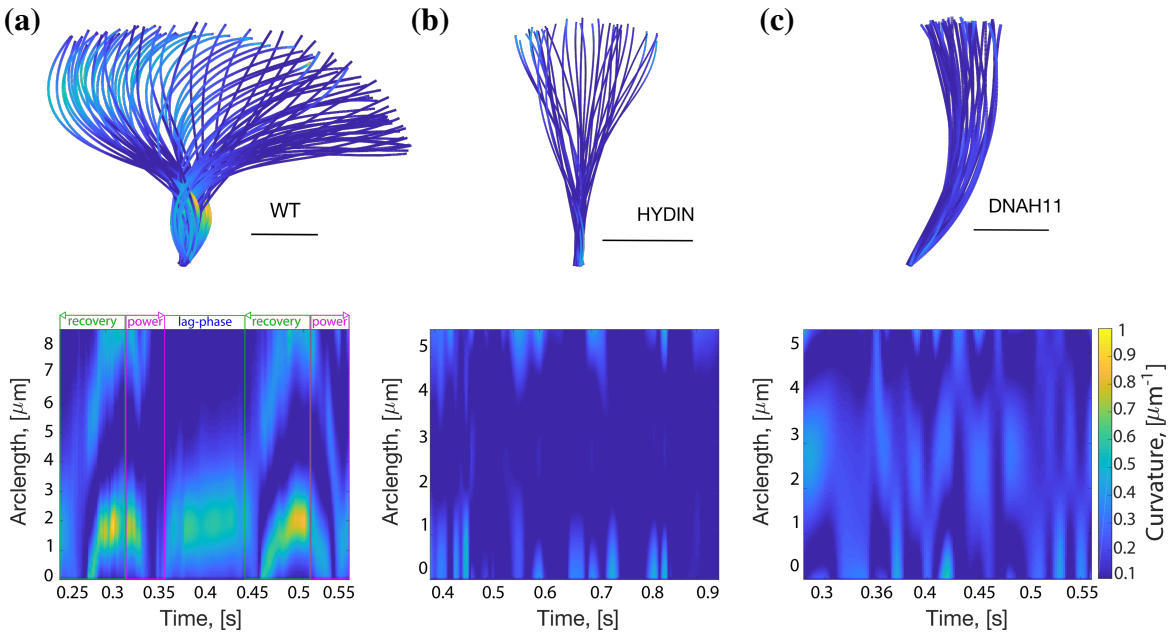

Fig. 5.6 **Representative kymographs of single cilia in healthy and PCD samples highlight very different dynamics of curvature along the cilium.** Reconstructed ciliary beating patterns with the local curvature indicated in colour (top) and curvature kymographs (bottom) show the time evolution of the curvature in representative cilia from **(a)** healthy, **(b)** HYDIN and **(c)** DNAH11 samples. Very obvious patterns show in the healthy samples, where regions of high/low curvature travel from basal to distal end during the recovery stroke, and the curvature is lower overall in the power stroke, during which the cilium moves in an extended configuration. It is also possible to spot a "lag-phase", in which the cilium pauses between the end of a power stroke and the beginning of the recovery stroke. PCD samples do not exhibit such marked features.

(healthy, DNAH11, HYDIN), and pooled together the data of samples within each type to obtain average measurements.

The average curvature (measured as the average within each sample type of the time-averaged curvature) along the cilium is much higher in healthy cells than in both PCD variants, with DNAH11 showing higher curvature than HYDIN at mid-cilium (Figure 5.7a). This is consistent with what shown in the representative tracked cilia in Figure 5.6.

The degree to which the curvature at a given position along the cilium changes throughout the beating cycle can be measured by taking its standard deviation over time. The standard deviation of the curvature is on average lower for PCD samples caused by mutations in both DNAH11 and HYDIN than that observed in healthy cells, and does not vary as markedly along the arc length of the cilium (Figure 5.7b). This is consistent with the reconstructed cilia shown as an example in Figure 5.6.

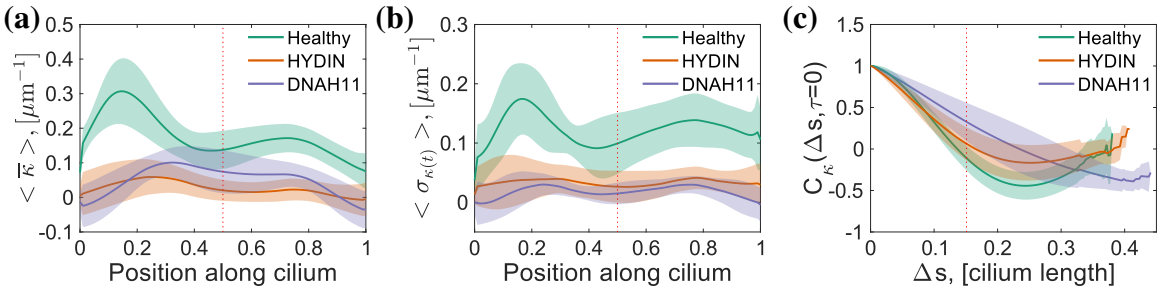

Fig. 5.7 **Curvature captures difference in beating patterns.** **(a)** Time-averaged curvature as a function of the relative position along the cilium, plotted as average across tracked cilia (solid lines) $\pm$ standard deviation (shaded regions). The curves from the different samples are clearly different, and they reflect the differences in beating patterns of the three samples. **(b)** To measure how much the local curvature changes over a beating cycle we plot the standard deviation of the curvature over time as a function of the relative position along the cilium. The solid line shows the average, while the standard deviation across reconstructed cilia is depicted as a shaded region. Again, values for the healthy samples are much higher than for the PCD variants, showing how much the healthy cilia change configuration during the beat. **(c)** The autocorrrelation of the curvature plotted here as average across tracked cilia $\pm$ standard deviation (solid line and shaded region) shows how gradually or suddenly the curvature changes along the cilium. The curves are significantly different: p-value at $\Delta s = 0.15$ is < 0.05 between healthy and HYDIN, < 0.01 between HYDIN and DNAH11, and $\ll 0.01$ between healthy and DNAH11 (unpaired, two-tailed Student's t-test). The red dotted lines throughout the figure highlight a subset of the parameters used to build the "barcode" for Principal Component Analysis as reported in section 5.4.4.

To measure how suddenly or gradually the curvature changes along the cilium we look at the autocorrelation of the curvature over the the arc length. Figure 5.7c shows how the curve obtained from the healthy sample decays faster than both the DNAH11 and HYDIN curves, consistent with the rapid variations of curvature along the cilium that can be seen in Figure 5.6a. The curvature autocorrelation decays the slowest in the DNAH11 variant, compatible with cilia affected by this PCD variants having a low but persistent curvature along their length.

5.4.3 Force exerted by the cilium during the beat cycle

Inspired by [52] we used Resistive Force Theory to calculate the force that a single cilium exerts on the surrounding fluid along its entire length during a single beat cycle (5.3.5, Figure 5.3a-c), and then considered the force per unit length throughout the beat cycle of a single cilium, represented as a kymograph in Figure 5.3d. For all samples the force per unit length exerted by the cilium cilium increases from base to tip, as expected since as the

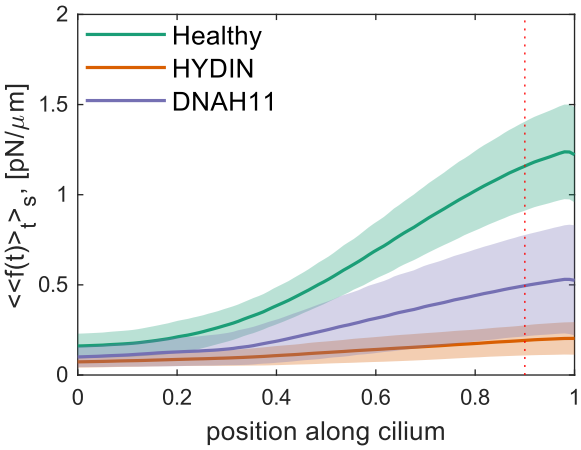

Fig. 5.8 **Force measurements captures differences between healthy and PCD variants.** Time-averaged force density as average across tracked cilia $\pm$ standard deviation (solid line and shaded region) versus the position along the cilium. As expected the force the cilium exerts on the surrounding fluid increases with the distance from the basal end of the cilium, and is much higher for healthy samples than for respectively HYDIN and DNAH11. The force density measured at $9/10$ of the cilium length (red dotted line) is one of the parameters used to build the "barcode" for PCA.

distance from the basal body increases the corresponding point on the cilium must cover increasingly larger amplitudes in the same amount of time (Figure 5.8).

In the population of healthy beating cilia, the force exerted at the distal end is approximately twice as large as the force exerted by cilia from cells with mutations in DNAH11, and approximately five times higher than cilia from cells with mutations in HYDIN. In cilia affected by the PCD variant HYDIN the increase in force along the cilium is minimal, while for DNAH11 mutant cells the force density increases at a higher rate starting from approximately a third of the cilium arc length.

Having measured the force along the cilium during the beat cycle, one can map the position of the "centre of drag" of the cilium over time by calculating the average of the cylinders' positions weighted with the magnitude of the force they exert on the fluid. The motion of the centre of drag has been shown [32] to be important in synchronising cilia dynamics to enable mucociliary clearance. In chapter 6 we study the synchronisation of a model system of two free-phase rotors driven along paths that mimic the trajectory of the centre of drag of cilia.

5.4.4 Principal component analysis discriminates between DNAH11 and HYDIN PCD variants

In the previous sections we showed in detail how the analytical methods described in this chapter allow us to measure several quantities on a tracked cilium shape. We hypothesised that a subset of these values would be sufficient to build a quantitative "barcode" that characterises the sample and that can be used to discriminate between different PCD variants. To test this, we ran Principal Component Analysis (PCA) on the subset of all analysed cilia in which all of the measurements detailed so far in this chapter were undertaken (14 HYDIN cilia, 10 DNAH11 cilia, and 12 healthy cilia). Out of all the measurements taken we chose five specific parameters to build the "barcode" for our samples: i) the amplitude of the beat at $5\,\mu\mathrm{m}$ from the cell surface, ii) the time averaged curvature measured at mid-length, iii) the standard deviation of the curvature over time measured at mid-length, iv) the autocorrelation of the curvature, measured at $\Delta s = 0.15$, and v) the mean force exerted on the fluid, measured at nine tenths of the cilium length.

Our first PCA (Figure 5.9a) demonstrates how the data points, projected on the first 2 principal components (PCs), cluster very obviously according to whether they were collected on healthy or PCD samples. The separation of the data according to their genotype was confirmed by an unsupervised clustering algorithm (k-means by MATLAB), which successfully separated data from healthy and PCD samples based exclusively on the score of the data points along the first two PCs, i.e. their position in the plot in Figure 5.9a. It is worth stressing that neither the PCA algorithm nor the clustering algorithm knew the genotype of the data points.

While the first PCs obtained by PCA on the entire set of measurements are effective in separating healthy from PCD data, they struggle to distinguish between the DNAH11 and HYDIN PCD variant forms. To address this, we ran PCA on a dataset of PCD data only. The PCD data projected on the new set of axes show two non-intersecting clusters (Figure 5.9b), while the data from healthy cilia, projected onto this set of PCs, form a third, separated cluster. Thus, principal components found on the PCD-only dataset can be used to discriminate between the phenotypes of DNAH11, HYDIN, and healthy cilia. It is worth noting however that, in this case, the k-means clustering algorithm was not able to correctly separate the two PCD clusters without prior knowledge of the sample type.

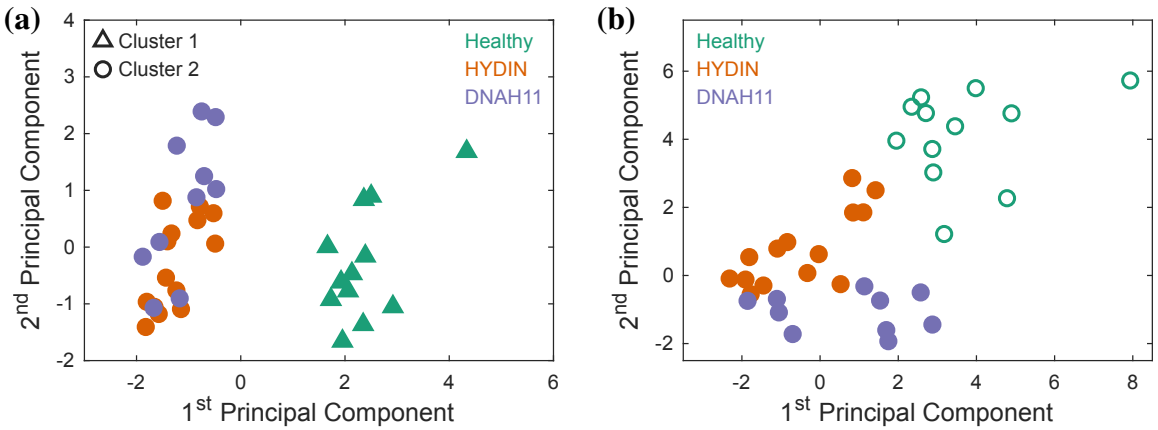

Fig. 5.9 **PCA differentiates between PCD variants.** Having built a smooth representation of the cilium configuration over time, we can extract five parameters (reported in section 5.4.4 and highlighted with red dotted lines throughout Figures 5.4, 5.7, and 5.8) to create a "barcode" that characterises the beating pattern. **(a)** Principal Component Analysis on the "barcode" data highlights the difference in phenotype between Healthy and PCD cilia. Here we plot the projection on the 2 first Principal Components of data from 12 healthy cilia, 14 HYDIN cilia, and 10 DNAH11 cilia. Data from the healthy samples cluster very obviously from data on PCD samples. While the colour of the markers codes the genotype of the samples, the shape of the markers show the clustering obtained by an algorithm that was blind to the sample type of each data point: this clustering algorithm was able to successfully separate the healthy data from the PCD data without any prior knowledge. The separation in PCA shows that the set of measurements described in this work could be useful to discriminate between a healthy sample and a sample affected by DNAH11 and HYDIN. **(b)** Principal Component Analysis furthermore shows the difference in beating pattern between DNAH11 and HYDIN cilia. We plot the projection on the first principal components of data from 14 reconstructed trajectories of HYDIN cilia and 10 reconstructed trajectories of DNAH11 cilia (full symbols). The principal components were obtained by running PCA on the set of 14+10 PCD cilia only. Data points from the two PCD mutations form two different clusters in the plane defined by the first two PCs. The data points from the healthy cilia (empty symbols) form a third cluster when projected on the same PCs.

5.4.5 Supervised machine learning correctly classifies new data

As a sanity check, to try and assess how well the analysis suggested in this chapter can highlight the difference between healthy, DNAH11 and HYDIN cilia, we tried performing a machine learning assisted "diagnosis" of sorts.

Our collaborators in Toronto provided us with additional high speed microscopy videos of samples from the two PCD variants, collected on samples from the same donors as previously, but at a different time point. Our goal was to have the computer classify these new data as DNAH11 or HYDIN samples.

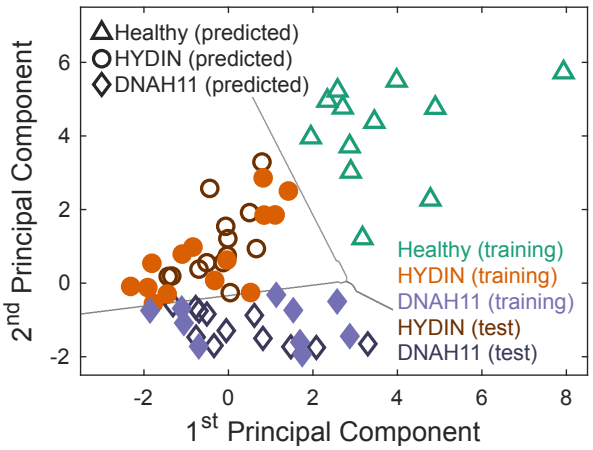

Fig. 5.10 **Supervised machine learning successfully classifies PCD variants.** We used the projection of the dataset featured in this chapter on the first two Principal Components defined by the PCD-only data (full symbols) to train a classifier (`fitcecoc`, by MATLAB). We can see that the training was successful since all training data (light colours show the sample type) have been correctly classified (markers show the classification performed by the trained model). Crucially, when projecting an additional test dataset of HYDIN (dark orange) and DNAH11 (dark violet) reconstructed cilia from the same donors on the same set of Principal Components, the classifier successfully labels them as HYDIN (circles) and DNAH11 (diamonds) without prior knowledge of their genotype. No data point was classified incorrectly. The grey lines show the boundaries of the genotype-specific regions individuated by the classifier.

The base of Principal Components found by running PCA on the PCD-only data analysed so far is effective in separating the two PCD variants from each other and the healthy samples (Figure 5.9b). This prompted us, as a first step, to use the data projected on the first two of these Principal Components as a labelled training dataset for a Multiclass Classification Model (using `fitcecoc` by MATLAB). The model was trained successfully, in that no data point in the training dataset was misclassified. After reconstructing the beating pattern of cilia in the new PCD videos we had the model classify the projection of their "barcodes" onto the same base of Principal Components. The test dataset was classified perfectly: as shown in Figure 5.10 the trained model, without prior knowledge of the phenotype of the new data, did not miscategorise any data point.

While this is not a very meaningful application of machine learning, as the sample size is extremely restricted, it still represents a proof-of-concept of how the reconstruction and analysis of the cilium beat pattern from high speed microscopy videos could be used to aid clinicians in their diagnosis.

5.5 Accurately tracking the cilium shape yields a wealth of yet-unused information

The analysis presented in this chapter enabled a good characterisation of ciliary beating defects observed in PCD and allowed us to assign unique quantitative profiles to specific PCD variants with mutations in either DNAH11 or HYDIN within the analysed samples. This fairly straightforward analysis requires only standard HSVM data as input, and does not require the use of specialised microscopy or experienced clinicians. We anticipate that a quantitative approach to characterising ciliary beating defects will advance both the diagnosis and understanding of PCD, particularly in cases where no ultrastructural defect or causal mutation is detected.

Despite being the most widely-reported parameter about ciliary beating, CBF is not the key parameter behind the physics of ciliary waves [32] and neither it is a very robust metric for the diagnosis and analysis of variant forms of PCD, or even PCD versus non-PCD [154]. An example is the HYDIN variant form of PCD, which is characterised by CBF ranges indistinguishable from healthy cells [153]. In the analysis presented here, however, the HYDIN variant PCD cilia were clearly distinguishable from healthy control on the basis of velocity and amplitude of the beating stroke, and on the curvature of the cilium throughout it. Previous attempts to quantify velocity and amplitude of ciliary beating have been reported [99, 164], however these studies analysed only the movement of the tip of the cilia relative to the base. This basic measurement does not fully capture how the parameters that characterise a beating stroke vary along the cilium length or throughout a beat cycle. Using a more extensive description of the beating pattern is necessary to build an accurate reconstruction of the ciliary waveform and to quantify important differences between PCD DNAH11 and HYDIN variants.

Many cases of PCD are characterised by defects in ciliary bending [153]: both the HYDIN- and DNAH11-causing PCD variants have been described as “bending capacity reduced” (HYDIN; [163]) and “reduced bending/increased stiffness” (DNAH11; [153]). However this qualitative description does little to distinguish between the two forms. Our analysis on the other end found quantitative differences in the local curvature of DNAH11 and HYDIN variant PCD cilia. The two variants also differed in the force the cilia exert on the surrounding fluid. Principal component analysis showed how, taken together, the measurements undertaken can form a quantitative “barcode” that can be used to discriminate between different variant forms of PCD, and between PCD and healthy samples.

5.6 Diagnostic potential of ciliary beat pattern analysis

The analysis presented in this work is quite simple and straightforward, but gives already good results in terms of identifying the beating pattern of cilia, in that data points from different genotypes cluster in different regions of the variables' space. The next logical step to expand this work would be its diagnostic implementation, that would depend on the collection of a much bigger dataset, ideally on all variants of PCD. These data would be used to establish a reference database of ciliary beat "barcodes": an extensive dataset of parameters measured on several patients for each of the PCD variants that could then be used as a training database for a supervised machine learning algorithm. A successful application of machine learning would then be an invaluable help to medical doctors in classifying an "unknown" sample as one of the PCD variant forms (or a healthy sample).

The main limiting factor to achieve this objective would be the reconstruction of the beating pattern, as of now this happens by painstakingly, manually tracking the cilium frame-by-frame. Moreover, while 5 parameters are enough to discriminate between the 3 genotypes analysed in this chapter, a higher dimensional dataset might be necessary to have the same level of success on a wider range of PCD variants. This would not be a problem if the tracking of the cilia were automated, as then one could perform a more sophisticated analysis, possibly employing tools that have already been developed but so far only applied to the study the motion of isolated flagella on single cell eukaryotes [21, 47, 48, 51, 52, 59, 165–167], or the behaviour of model organisms such as *C. elegans* [168].

Many institutions already use HSVM as a primary method to diagnose PCD, however evaluation criteria vary between groups and the data are largely qualitative. Furthermore, current HSVM methods give little insight into the nature of the beating defect itself nor where it manifests on the cilium, nor when it occurs during the beat cycle. A quantitative database of ciliary beat "barcodes" unique to each PCD variant, even obtained without an automated tracking system, would be useful in aiding diagnoses, particularly in cases where no ultrastructural defect or known causal mutation is detected.

Chapter 6

Coarse-graining the ciliary beat pattern to understand strength of synchronisation

6.1 Colloidal rotors as a model system for beating cilia

The problem of how cilia synchronise is a non trivial one, and it can be tackled from different perspectives. The work presented so far studies cilia and their synchronisation with a "top-down" approach: starting from data acquired on a sample fairly similar (from a physicist's point of view) to the airway epithelial tissue, we tried to extract features so that we could take measurements on how cilia interact and beat in a coordinated fashion. The complementary path is the "bottom-up" approach: starting from analysing the behaviour of a very simple model, we try to infer the properties of the more complex situation.

Building on the work done by our group [18, 32, 44–46, 62–64, 169], in this chapter I will model cilia as free-phase oscillators, only coupled via hydrodynamics interactions, and study their synchronisation. In particular, I will coarse-grain the beat pattern of a cilium, characterised following chapter 5, into parameters of a free-phase rotor: a simulated colloidal bead driven along a closed trajectory by a periodically modulated force (Figure 6.1). To achieve free-phase the driving force is set, via a feedback loop, as a function of the position of the bead along its prescribed trajectory (and not as a function of time). The rotor model is powerful because it is possible in principle to calculate properties of the steady state dynamics of coupled rotors analytically. This has been done by Uchida and Golestanian on simpler orbits than the ones employed here [170–172].

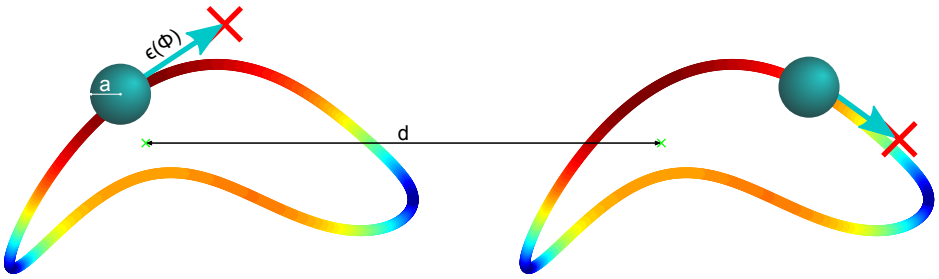

Fig. 6.1 **We model cilia as colloidal rotors.** Using Resistive Force Theory we coarse-grain the parameters of the ciliary beat into the trajectory of free-phase colloidal rotors (see section 6.3 and 5.3.5). Each rotor is driven along a closed path by a modulated driving force, implemented as a harmonic potential (a "trap") with the minimum placed at a tunable distance $\epsilon(\Phi)$ ahead of the rotor (red cross). The driving force (colour coded, increasing from blue to red) only depends on the phase (i.e. the angular position) along the trajectory. The two orbits are shown very close here for display purposes.

Section 6.2 will briefly go over the physics of hydrodynamic interactions between spherical objects at low Reynolds number, section 6.3 will explain how the ciliary beat pattern is coarse-grained into the closed trajectory of a rotor, while section 6.4 will report measurements of the strength of synchronisation between two rotors.

6.2 Hydrodynamics of colloidal beads at low *Re*

At the scale of cells or bacteria, hydrodynamics is very different than the fluid dynamics of macroscopic systems. This is well captured by the Reynolds number, the dimensionless ratio between the inertial forces and the viscous forces of a system with typical size L and flow velocity u:

$$Re = \frac{F_{\text{inertial}}}{F_{\text{viscous}}} = \frac{\rho u L}{\eta}, \tag{6.1}$$

where ρ is the density of the fluid and η its viscosity.

For an airway cilium of $L \sim 10\,\mu\text{m}$, beating in medium of $\rho = 10^3\,\text{kg}^3/\text{m}$ and $\eta = 10^{-3}\,\text{Pa}\,\text{s}$ after having washed the mucus, its tip moving at a typical velocity of $u \sim 200\,\mu\text{m}/\text{s}$, the Reynolds number is $\sim 10^{-3}$. In comparison, a human swims at $Re \sim 10^4$.

This affects dramatically the way swimmers propel themselves: in the words of Edward Purcell, for low Re swimmers "inertia is totally irrelevant. *We* know that $F = ma$, but they could scarcely care less" [19]. At low Re, as soon as a swimmer stops deforming its body, the surrounding fluid stops moving instantaneously, and no propulsive force is maintained by inertia. This also means that a swimmer, to have net propulsion over time, needs a cyclic

deformation of its body that is *non reciprocal* [19]. An example of this is the way the airway cilia deform over time.

6.2.1 Hydrodynamic coupling

As mentioned in the introduction, in this chapter we are going to approximate the cilium with a driven, simulated colloidal bead of radius a, and we are going to study how two of these rotors synchronise. In a system of n driven beads coupled via hydrodynamic interactions the velocity of each bead depends on the driving force acting on it, but also on the velocity of the other beads, and on Brownian noise [169]:

$$\mathbf{v}_i = \sum_{j=1}^{n} \boldsymbol{\mu}_{i,j} \left(\mathbf{F}_j + \mathbf{f}_j \right), \tag{6.2}$$

where $\mathbf{v}_i$ is the velocity of the bead i, and $\mathbf{F}_j$ is the driving force acting on the bead j. $\boldsymbol{\mu}_{i,j}$ represents the mobility matrix, that in our model system implements the dynamics of two particles in a viscous fluid accounting for their distance from a solid surface with no-slip boundary conditions (a "wall"). $\mathbf{f}_i$ is the stochastic Brownian noise acting on bead i, characterised by zero mean $\langle \mathbf{f}(t) \rangle = 0$ and correlation $\langle \mathbf{f}_i(t) \mathbf{f}_j(t') \rangle = 2 k_B T \boldsymbol{\mu}_{i,j}^{-1} \delta(t - t')$ [45].

Blake's mobility matrix

The diagonal terms of the mobility matrix $\boldsymbol{\mu}_{i,j}$ are given by the viscous drag coefficient of the bead. In bulk, the viscous drag is simply the Stokes drag, so that $\boldsymbol{\mu}_{i,i} = \frac{\mathbf{I}}{6\pi\eta a}$. Close to a wall we can instead add corrections to the Stokes drag as terms of a series expansion in a/z_i [173], with z_i the distance of the i-th bead from the wall:

$$\mu_{i,i}^{x,x} = \mu_{i,i}^{y,y} = \frac{1}{6\pi\eta a} \left[1 - \frac{9a}{16 z_i} + \frac{1}{8} \left(\frac{a}{z_i} \right)^3 - \frac{1}{16} \left(\frac{a}{z_i} \right)^5 \right] \tag{6.3a}$$

$$\mu_{i,i}^{z,z} = \frac{1}{6\pi\eta a} \left[1 - \frac{9a}{8 z_i} + \frac{1}{2} \left(\frac{a}{z_i} \right)^3 - \frac{1}{8} \left(\frac{a}{z_i} \right)^5 \right] \tag{6.3b}$$

$$\mu_{i,i}^{\alpha,\beta} = 0 \text{ for } \alpha \neq \beta \tag{6.3c}$$

As the simulations carried out in this work are conducted far enough from the wall, only the first order correction to Stokes drag was implemented in the code.

To find the non-diagonal terms of the mobility matrix $\boldsymbol{\mu}_{i,j}$ $(i \neq j)$ Blake suggested in [174] to describe the flow created by a Stokeslet (a point-like delta force) near a surface with an

image method. The no-slip boundary condition of the wall is implemented by describing the effect of the wall as equivalent to an infinite fluid, but with an "image Stokeslet" at the mirror position of the first Stokeslet and with an opposite force. This yields the following expression for the off-diagonal terms of the mobility matrix $\boldsymbol{\mu}_{i,j}$ [63, 174]:

$$\boldsymbol{\mu}^B_{i,j} = \frac{1}{8\pi\eta}\left[\mathbf{G}^S(\mathbf{r}_i - \mathbf{r}_j) - \mathbf{G}^S(\mathbf{r}_i - \bar{\mathbf{r}}_j) + 2z_j^2\mathbf{G}^D(\mathbf{r}_i - \bar{\mathbf{r}}_j) - 2z_j\mathbf{G}^{SD}(\mathbf{r}_i - \bar{\mathbf{r}}_j)\right]. \quad (6.4)$$

In this equation $\mathbf{r}_i = (x_i, y_i, z_i)$ is the position of the i-th Stokeslet, $\bar{\mathbf{r}}_i = (x_i, y_i, -z_i)$ the position of the image Stokeslet, and the wall is at $z = 0$. $\mathbf{G}^S$, $\mathbf{G}^D$, $\mathbf{G}^{SD}$ are respectively the contribution of a Stokeslet, source doublet, and Stokeslet doublet, and are defined in [63, 171, 174] as:

$$\mathbf{G}^S_{\alpha,\beta}(\mathbf{r}) = \frac{\delta_{\alpha,\beta}}{r} + \frac{r_\alpha r_\beta}{r^3} \quad (6.5a)$$

$$\mathbf{G}^D_{\alpha,\beta}(\mathbf{r}) = (1 - 2\delta_{\beta,z})\frac{\partial}{\partial r_\beta}\left(\frac{r_\alpha}{r^3}\right) \quad (6.5b)$$

$$\mathbf{G}^{SD}_{\alpha,\beta}(\mathbf{r}) = (1 - 2\delta_{\beta,z})\frac{\partial}{\partial r_\beta}\mathbf{G}^S_{\alpha,z}(\mathbf{r}) \quad (6.5c)$$

with $\alpha, \beta \in \{\text{'}x\text{'}, \text{'}y\text{'}, \text{'}z\text{'}\}$, $\mathbf{r} = (r_x, r_y, r_z)$ and δ the Kronecker delta.

6.2.2 Numerical simulations

The simulations in this thesis are carried out using a C++ program that implements the Brownian dynamics Ermak McCammon algorithm to integrate the equations of motion (eq. 6.2) of N interacting particles with hydrodynamically coupled Brownian fluctuations [175].

The C++ program was initially written by Loïc Damet in 2010, and has been modified by Dr Nicolas Bruot during his PhD. It was initially able to simulate systems of either rowers (oscillators moving back and forth along a line) or rotors moving along a circular trajectory. My updates enable the simulation of rotors along a closed, non circular, non self-intersecting, analytically defined trajectory.

6.3 From cilia to rotors

In chapter 5, and in particular in section 5.3.5, we reported our efforts to measure the force exerted by the cilium onto the fluid during its beat cycle. Briefly, we divide the cilium into cylinders, and track the displacement of each cylinder between consecutive frames. Resistive Force Theorem gives us the coefficients of anisotropic drag $c_\parallel$ and $c_\perp$ needed

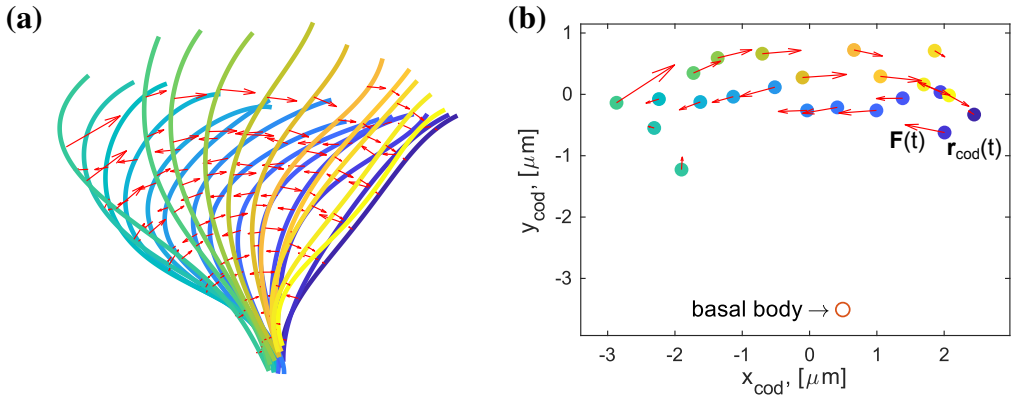

Fig. 6.2 **We use Resistive Force Theory to find the centre of drag of the cilium. (a)** As detailed in section 5.3.5 we find the force per unit length (red arrows) exerted by the cilium on the fluid over time (colours, from blue to yellow) using Resistive Force Theory. **(b)** At each time (colours) we then find the centre of drag of the cilium by averaging the positions of the small cylinders used to measure the force, weighted by their contribution to the total force (red arrows).

to link the velocity of the i-th cylinder $\mathbf{v}_i = \mathbf{v}_{i\parallel} + \mathbf{v}_{i\perp}$ to the force it exerts on the fluid $\mathbf{f}_i = (c_\parallel \mathbf{v}_{i\parallel} + c_\perp \mathbf{v}_{i\perp}) l_i$, with l_i the length of the cilium. Repeating this for all cylinders along the cilium and for all the snapshots of the cilium configuration over time we obtain a measurement for the force density throughout the beat cycle (Figures 6.2a and 5.3).

In this section I present how these data are used to determine a trajectory and a modulated driving force for a colloidal rotor that coarse-grains the cilium.

6.3.1 How to coarse-grain the cilium as a rotor moving along the trajectory of its effective centre of mass

Having found the force density we can then define an effective centre of mass of the cilium, that we will call "centre of drag", as the average of the positions of the cylinders weighted with the magnitude of the force they exert on the fluid: At time t, with the cilium split in N cylinders at position $\mathbf{r}_i = \mathbf{x}_i + \mathbf{y}_i$, each of them exerting a force of magnitude f_i on the fluid, the centre of drag will be located at

$$\mathbf{r}_{cod} = \frac{\sum_{i=1}^{N} f_i \mathbf{r}_i}{\sum_{i=1}^{N} f_i}. \tag{6.6}$$

The natural choice to coarse grain the parameters of the ciliary beat pattern into a colloidal rotor is then to have the latter follow the trajectory of the centre of drag $\mathbf{r}_{cod}(t)$ over time (Figure 6.2b).

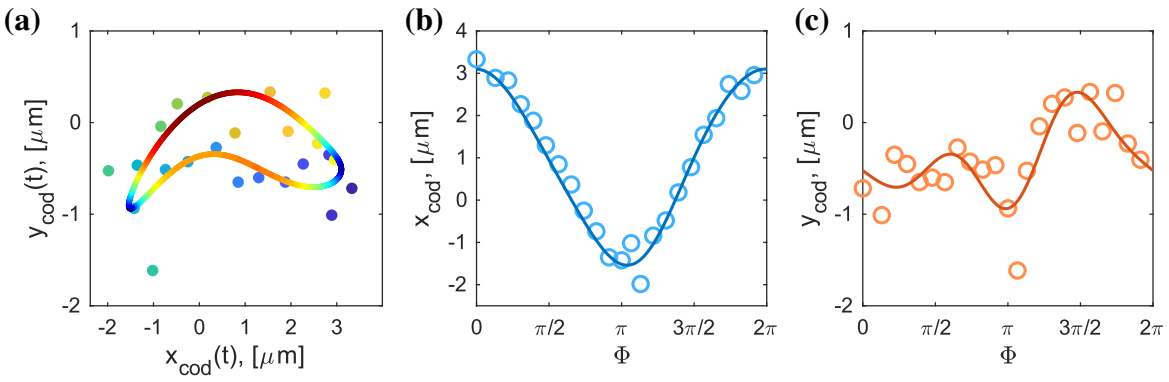

Fig. 6.3 **Fourier series yield an analytical description of the trajectory of the centre of drag. (a)** The experimental trajectory of the centre of drag (dots, time increases from blue to yellow) needs to be approximated by an analytical function. This is achieved by taking the Fourier transform of the dependence of the x- and y-coordinate (circles) with the phase along the cycle, and only keeping the first few modes **(b, c)**. The continuous lines show the analytical description of the x- and y-coordinates given by a Fourier series truncated at mode $n = 3$.

6.3.2 Fourier Transform yields an analytical description for the trajectory

The trajectory of the centre of drag obtained by analysing the experimental data needs to be written in an analytical form to be used for simulations. The simulations will eventually need the trajectory, and the driving force along it, to be an analytical function of a phase variable Φ. The first step towards this goal is to find an analytical form for the trajectory as a function of the time t (rescaled on the cilia beating period T). A very effective way to do so is to use Fourier Transforms. In particular, each of the components of the trajectory $\mathbf{r}_{cod}(t) = x_{cod}(t)\hat{\mathbf{i}} + y_{cod}(t)\hat{\mathbf{j}}$ is Fourier transformed independently. An analytical description for the two components is then achieved by inverting the Fourier Transform while selecting only the first modes (up to n included). This effectively applies a low-pass filter to the trajectory, and it is necessary to reduce the noise given by the experimental error on the final reconstructed trajectory (Figure 6.3).

Given a discrete signal $x(\Phi)$ with N data points, the Matlab implementation of the N-points `fft` will yield a $\{\hat{x}_0 ... \hat{x}_N\}$ array which has again N entries. The coefficients of the low Fourier modes are at the beginning and the end of the array, and the very first entry (mode 0) only encodes the average $\langle x(\Phi)\rangle_t$. So, to only keep the modes up to n we set to 0 all entries with index $\in [n+1, N-n+1]$ and then invert via `ifft` the resulting array.

Analytically, this corresponds to taking the Fourier series of the initial signal $x(\Phi)$ only up to mode n:

$$\tilde{x}(\Phi) = \frac{2}{N} \sum_{k=0}^{n} \mathrm{Re}(\hat{x}_k) \cos(k\Phi) - \mathrm{Im}(\hat{x}_k) \sin(k\Phi) \,. \tag{6.7}$$

By applying this method to the time series of the centre of drag position along the x- and y- coordinates we obtain an analytical description for the trajectory as a function of a phase variable Φ that grows from 0 to 2π during the beat cycle:

$$\tilde{\mathbf{r}}_{cod}(\Phi) = \tilde{x}_{cod}(\Phi)\hat{\mathbf{i}} + \tilde{y}_{cod}(\Phi)\hat{\mathbf{j}} \tag{6.8}$$

This new variable Φ can be thought of as a rescaling of the time in the experimental data $\Phi = 2\pi t/T$. In the simulations Φ is simply a phase variable, that indexes the position of the bead along the prescribed trajectory.

Modulated driving force

The linear velocity of the centre of drag in the experimental data is not constant over time: it is higher during the power stroke than during the recovery stroke, and slowest during the transitions between the two. This is conserved in the analytical reconstruction of its trajectory, as its velocity along the trajectory $|\frac{\mathrm{d}}{\mathrm{d}\Phi}\tilde{\mathbf{r}}_{cod}(\Phi)|$ changes in magnitude with Φ.

The modulation in the velocity of the centre of drag translates naturally in a modulation of the driving force of the rotor: the driving force along the trajectory will simply be

$$\mathbf{F}(\Phi) \propto \gamma \left(\frac{\mathrm{d}}{\mathrm{d}\Phi}\tilde{x}_{cod}(\Phi)\hat{\mathbf{i}} + \frac{\mathrm{d}}{\mathrm{d}\Phi}\tilde{y}_{cod}(\Phi)\hat{\mathbf{j}} \right), \tag{6.9}$$

where $\gamma = 6\pi\eta a$ is the Stokes drag. Since the evolution of the x- and y-coordinate with Φ is simply a sum of sine and cosine terms we obtain an analytical expression for the driving force as well.

The method employed throughout this work, that only employs the velocity of the centre of drag to calculate the driving force, is a first approximation. A more refined approach would take into account the change of drag coefficient of the cilium throughout the beat cycle.

6.3.3 Finding the phase of the rotor along its prescribed trajectory

A key point of our simulations is that we do not impose the phase of the rotor. The driving force only depends on the position of the rotor along its trajectory (its phase Φ), rather than on time. This is implemented via a feedback loop: at each time-step (or at the time-step in which

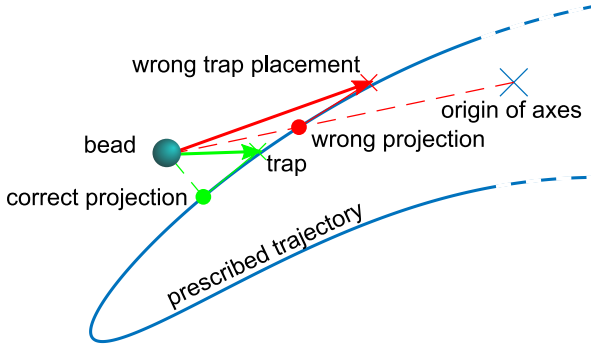

Fig. 6.4 **Finding the correct phase of the bead is fundamental for accurately applying the driving force.** The driving force of the rotor only depends on the position of the rotor along its trajectory. When the bead is displaced by its path (e.g. because of thermal noise, or interaction with the other rotor) it is crucial to project it onto the prescribed trajectory in the correct fashion. In red we show how the "naive" approach that works in case of circular trajectories is not suitable for non-circular ones. In green the correct approach.

we want to update the driving force) the program finds the position of each bead along its trajectory and applies the correct driving force. The prescribed trajectory is not infinitely rigid, and several factors contribute to displacing the bead from it, namely its relaxation towards the minimum of the driving potential, the displacements due to the fluid flow caused by the other bead, and thermal noise. The bead is kept close to the trajectory by a harmonic restoring force acting perpendicularly to the prescribed path. The C++ program implements the tangential driving force by placing the minimum of a harmonic potential (a "trap") a modulated distance ahead of the projection of the bead onto the trajectory: correctly projecting the bead onto the trajectory is thus necessary to ensure the driving force applied to the bead follows eq. (6.9).

Since the prescribed trajectory is effectively a limit cycle for our system, choosing a procedure for the projection of a bead onto the trajectory effectively prescribes a dynamics around the limit cycle. To be consistent to previous experiments in our group, we chose the projection to simply be perpendicular to the prescribed trajectory. Given the position $\mathbf{r}^b$ of a bead its projection is then just its closest point on the analytically defined trajectory $\tilde{\mathbf{r}}_{cod}(\Phi)$ centred in the origin of the axes, which means we need to find the phase Φ_0 that minimises the distance $\left|\mathbf{r}^b - \tilde{\mathbf{r}}_{cod}(\Phi)\right|$.

This is an easy feat in the case of circular trajectories, where the driving force is defined as a function of the angle ϑ^b between $\mathbf{r}^b$ and the horizontal axis, as in this case the projection of the bead onto the trajectory happens along $\mathbf{r}^b$ itself.

In our more general case (Figure 6.4) the most conceptually simple approach to find the position Φ_0 along the trajectory would be using a minimising routine, and actually solving the

problem of finding the value of phase Φ_0 that minimises the distance $\left|\mathbf{r}^b - \tilde{\mathbf{r}}_{cod}(\Phi)\right|$. While this would be the most accurate approach it is also the slowest, as the minimisation routine would be invoked hundreds of thousands of times in each simulation. I devised a faster approach that finds Φ_0 by interpolating between values of a lookup table. Details of this approach can be found in Appendix E.

6.4 Synchronisation of two cilia-modelling rotors

In the previous sections we have given a brief overview of the hydrodynamics of driven rotors, and explained how we coarse-grain the properties of the ciliary beat into a rotor. This section presents instead the results of simulations of two such model rotors, independently driven along identical trajectories with modulated force. The two rotors interact via hydrodynamics only, and their phase is free: the driving force only depends on where they are along their trajectory, and not on an external clock. The fluid flow generated by one of the rotors thus perturbs the motion of the second, and vice-versa. In these simulations, the centres of the rotors' trajectories are separated by a distance d and both lie along the x-axis. The simulations are run using the C++ program introduced in section 6.2.2. The parameters used to run the simulations are given in detail in Appendix E.

6.4.1 An effective potential drives the time-evolution of the phase difference between two hydrodynamically coupled rotors.

The evolution of the phase difference $\Delta(t) = \Phi_2(t) - \Phi_1(t)$ between the two rotors can be seen as driven by an effective potential. Previous work by our collaborators [170, 171] and our group [172] showed that it is possible to calculate such effective potential $V(\Delta)$ based on the temporal evolution of the phase difference, $\dot{\Delta}(t)$. In our simulations, $\dot{\Delta}(t)$ is defined as:

$$\dot{\Delta}(t) = \frac{\Delta(t + T_0) - \Delta(t)}{T_0} \tag{6.10}$$

where T_0 is the period of an unperturbed rotor.

By running several simulations starting from different initial conditions one builds a distributions of $\dot{\Delta}$ for each value of Δ. After averaging, the effective potential can then be calculated as:

$$V(\Delta) = -\int_0^{\Delta} \dot{\Delta} \mathrm{d}\Delta. \tag{6.11}$$

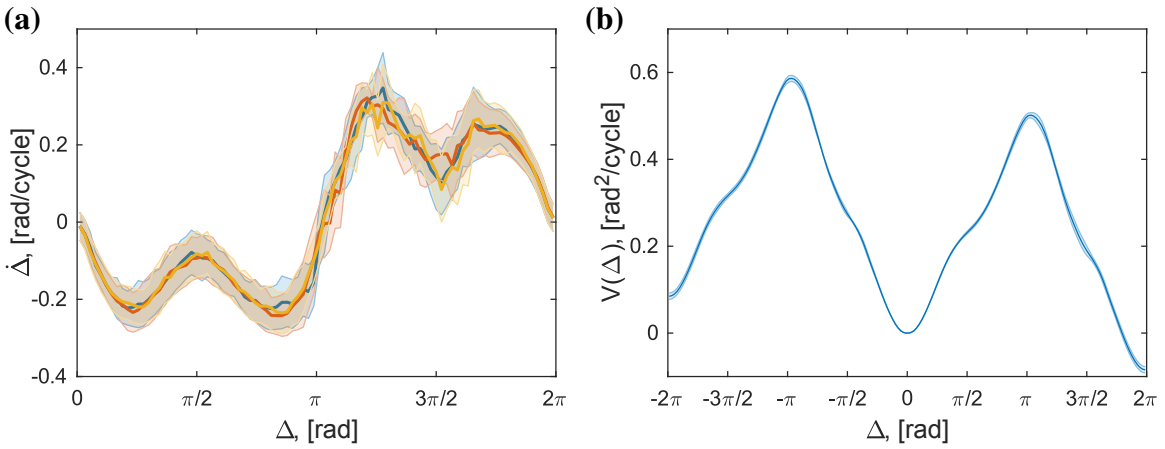

Fig. 6.5 **An effective potential drives the evolution of the phase difference.** The effective potential can be calculated starting from the time evolution of the phase difference **(a)**, by integrating it over the phase difference: $V(\Delta) = -\int_0^{\Delta} \dot{\Delta} \mathrm{d}\Delta$. In this case, the potential drives towards in-phase synchronisation **(b)**. Note that for display clarity the potential is plotted over two periods of the phase difference Δ. The depth of the well of the potential can then be used as a measure of the synchronisation strength between the beads.

The position of the minimum of the potential shows at what phase difference the rotors are phase-locked, as in the minimum $\frac{\mathrm{d}}{\mathrm{d}\Delta} V = -\dot{\Delta}(t) = 0$. For the purpose of this work, we will use the depth of the potential well as a measure of the synchronisation strength (Figure 6.5).

6.4.2 Synchronisation strength between two hydrodynamically coupled rotors on cilia-mimicking trajectories.

Following section 6.3.2 we coarse-grained the parameters of 10 healthy cilia and 5 cilia of patients affected by PCD (in particular, by a mutation in the gene that codes for the protein HYDIN) that we had already tracked for the analysis in chapter 5 into closed, analytically described trajectories, shown in Figure 6.6. For each of said trajectories we ran a series of simulations exploring a complete range of initial phase difference Δ_0, and were thus able to measure the effective potential that drives the time evolution of the phase difference between the two rotors following the procedure described in section 6.4.1.

The most striking aspect of the measured effective potentials, shown in Figure 6.6, is how much they depend on the shape of the trajectory, for what concerns the depth of the potential wells (i.e. the synchronisation strength) but also the number of minima: In several cases, the prescribed trajectories lead to local minima in the potential that reflect the existence of meta-stable states of the phase difference Δ. The location of the potential wells is not fixed either, with a few couples of rotors locked in anti-phase (with a phase difference $\Delta = \pi$). A

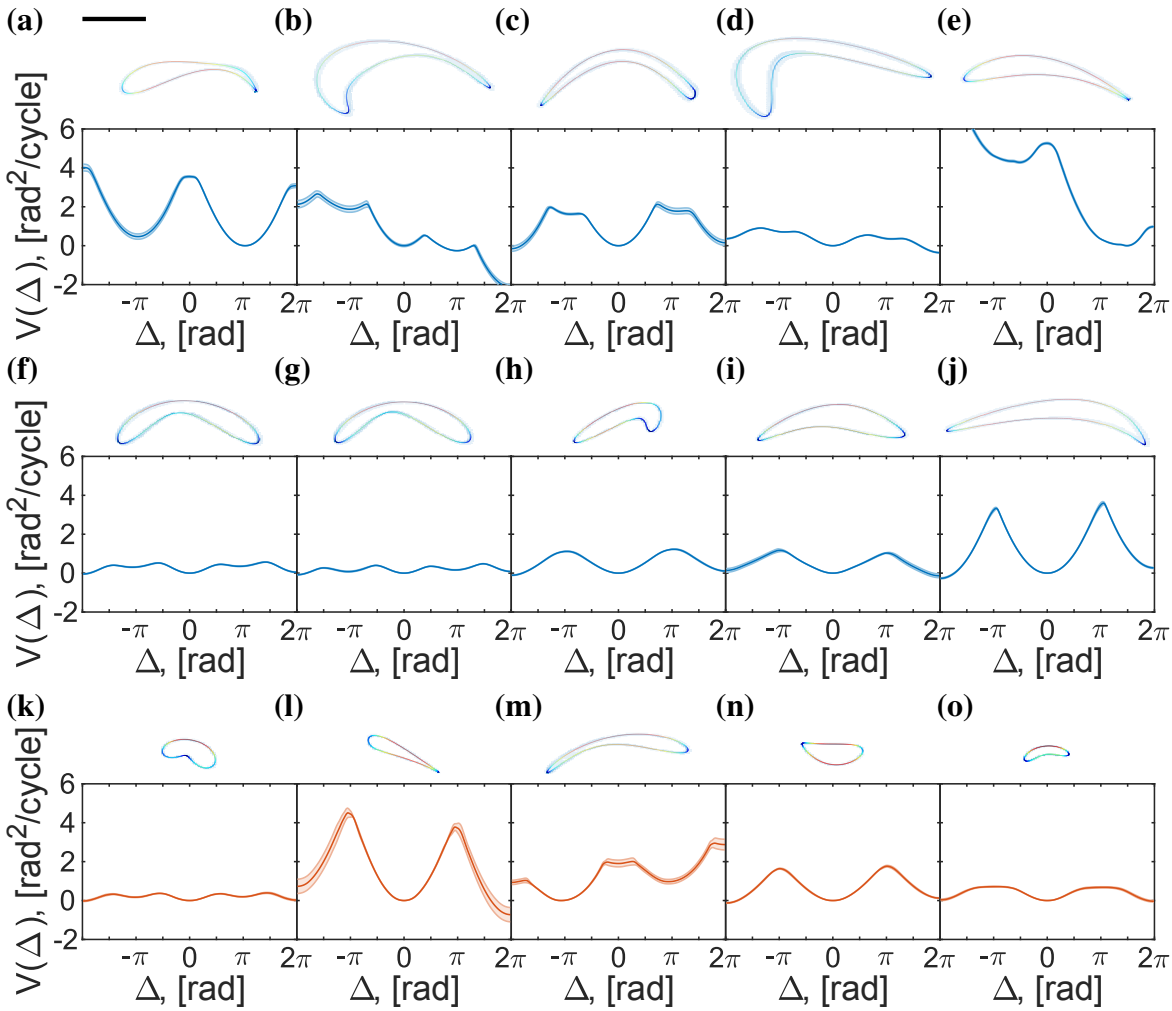

Fig. 6.6 **The effective potential is heavily influenced by the shape of the rotors' trajectory.** In each panel we plot the trajectory of the rotors **(top)**, and the effective potential we found driving their phase difference **(bottom)**. **(a-j)** show trajectories obtained by the tracking of healthy cilia, and the corresponding effective potentials, while in **(k-o)** are the trajectories obtained from cilia of patients affected by PCD (in particular, with mutation in the gene coding for the HYDIN protein). The coloured line shows the prescribed trajectory, with the velocity increasing from blue to red, and is superimposed to a heat map of the positions of one of the two rotors throughout the simulations (density increasing from light blue to dark blue). The centres of the two rotors' trajectories lie on the x-axis and are separated by a distance $d = 15\,\mu\text{m}$. Scale bar is $2\,\mu\text{m}$. The potentials are plotted over two periods of the phase difference Δ as this improves the readability of the graphs.

further important characteristic of the potentials shown in Figure 6.6 is that they are tilted, allowing for biased phase slips between the two rotors [29].

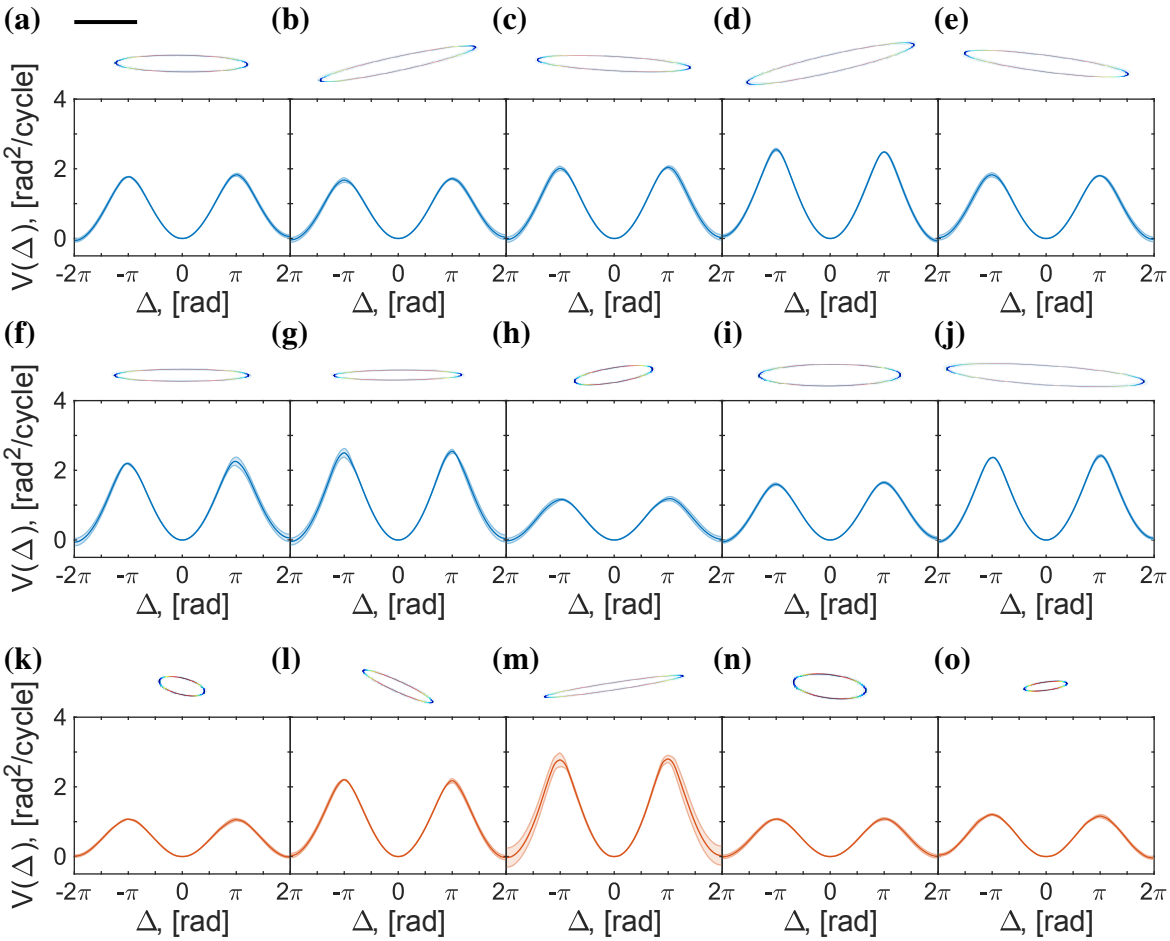

Fig. 6.7 **Cilia can be coarse-grained further as rotors driven along elliptical trajectories.** By only keeping the terms up to mode 1 in the procedure described in section 6.3.2 we approximate the trajectory of the centre of drag of the cilium with an ellipse. In each panel we show the prescribed trajectory (top, coloured lines, with velocity increasing from blue to red), the positions of one of the two rotors throughout the simulation (top, heat map, density increasing from light to dark blue), and the effective potential driving the time evolution of the phase difference (bottom), either in the case of healthy cilia **(a-j)** or in cilia from patients affected by a mutation in the gene that codes for the HYDIN protein **(k-o)**. Here we plot only the elliptical approximation of the same cilia as in Figure 6.6 for symmetry purposes. The centres of the two rotors' trajectories lie on the x-axis and are separated by a distance $d = 15\,\mu\text{m}$. Scale bar is $2\,\mu\text{m}$. The potentials are plotted against two periods of the phase difference Δ as this improves the readability of the graphs.

6.4.3 Synchronisation strength between elliptical rotors.

As reported in the previous section, the effective potentials driving the synchronisation of rotors on coarse-grained orbits are varied and seemed to be strongly influenced by the shape of the trajectory. To simplify the model further, the trajectory of the centre of drag of a

cilium can be coarse-grained by only taking up to mode $n = 1$ in eq. (6.7) for both x- and y-coordinates, effectively approximating it with an ellipse.

This approach allowed us to coarse-grain a few more tracked cilia than in the previous section (7 PCD cilia and 11 cilia from healthy patients), because it avoids one of the limitations of the current simulation software: by keeping higher modes in eq. (6.7) the coarse-graining trajectory can intersect itself, and this is a situation not handled by the simulation software. A self-intersecting trajectory would lead to ambiguity in the process described in Appendix E to find the phase of the rotor during the simulation, leading to unpredictable and unwanted behaviours. However, this approach also leads to an extremely simplified model in which, by definition, the force driving the bead is the same in opposite points along the ellipse, and it is maximal at low-curvature points of the orbit. In the future we plan to overcome this limitation, by decoupling the prescribed force from the description of the trajectory in our simulation program.

The effective potentials driving the temporal evolution of the phase difference Δ show a less rich variety of behaviours in the case of rotors on an elliptical trajectory, as displayed in Figure 6.7. Here all couples of rotors evolve towards an in-phase configuration, there are no metastable states, and the potentials are considerably less tilted. In the near future we plan to investigate the reason for such a stark difference in the effective potentials between the elliptical trajectories in Figure 6.7 and the more structured ones in Figure 6.6.

By plotting the synchronisation strength against the amplitude of the modulation of the velocity of the rotors along their trajectories (i.e. the difference between the maximum and minimum velocity along the cycle) we can see how these two quantities are strongly correlated (Figure 6.8). This is in agreement with what theoretically predicted [171] and previously observed [45] in the case of rotors driven along circular trajectories with a modulated force, where the strength of the synchronisation depended on the amplitude of the modulation of the driving force.

6.5 Colloidal rotors are a powerful model system to study synchronisation at low *Re*

This chapter presents a way to coarse-grain the parameters of the beating pattern onto a free-phase oscillator, in particular a simulated colloidal particle driven along a closed trajectory by a periodically modulated force. The phase of the oscillator is left free by implementing the driving force via a feedback loop, so that the driving force is only dependent on the position of the particle along its trajectory, and not on an external clock. This allow two such

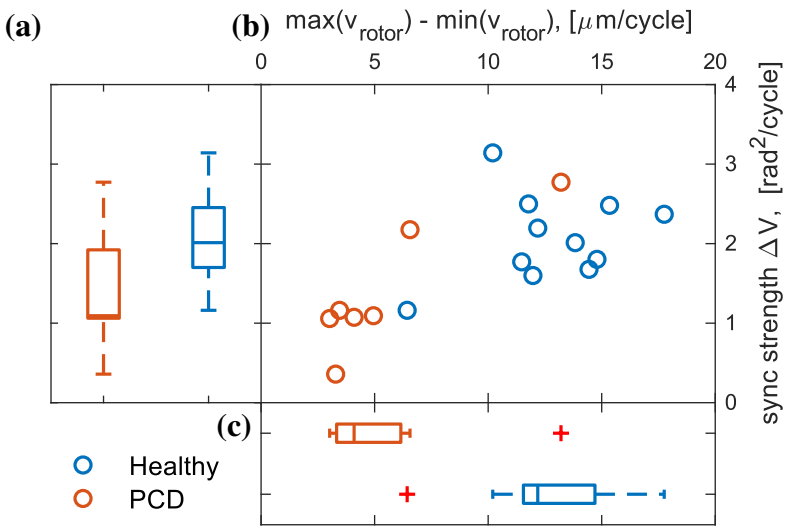

Fig. 6.8 **Synchronisation strength correlates with the velocity modulation.** After measuring the effective potential that drives the phase difference between rotors on elliptical trajectories, here we show how the synchronisation strength is correlated with the modulation of the velocity of the rotors. **(a)** shows box plots of the synchronisation strength, highlighting how this is on average lower in the elliptical trajectories derived from PCD cilia (red) than in those obtained from healthy cilia (blue). In **(b)** instead the plot of the synchronisation strength of each couple of rotors against the amplitude of the modulation of their velocity highlights how the two quantities are correlated. **(c)** shows how on average the difference between the highest and lowest value of the velocity of a rotor driven along the trajectories obtained from PCD cilia (red) is smaller than in "healthy" trajectories (blue).

oscillators, if close enough to one another, to interact via hydrodynamic coupling, and to achieve phase-locking.

A system of free-phase rotors had already been realised by our group in the past [32, 45, 60, 172], but while the driving force could be modulated, the rotors had to be driven along a circular trajectory. The method proposed in this chapter allows for a more realistic model. The key point is that the trajectory of the driven oscillator is obtained from experimental data: after tracking the cilium shape over time in a microscopy video, we find the centre of drag of the cilium throughout its beating cycle. Using Fourier series we then find a relatively simple analytically described closed curve that approximates the experimental trajectory of the centre of drag. The stable and metastable states of the system can be effortlessly identified by calculating, on the basis of the simulation data, an effective potential that drives the time evolution of the phase difference between the two interacting rotors.

This more realistic model system can be used to investigate how different beating patterns lead to different synchronisation strengths, or different stable states. While this chapter does feature a proof-of-concept in this direction, the possibility of a more methodical study would

rely on the ability to track a great amount of cilia, from good quality microscopy videos, in order to extract the trajectory of the centre of drag.

From a more physics-oriented point of view, the ability to simulate rotors driven along customisable trajectories can help understand what parameters influence the phase-locking of the system. In particular, it could be interesting to gradually modify the shape of the trajectory exploring, for example, the transition from a circular trajectory to an ellipse with very high eccentricity, extrapolating then the behaviour towards a 1D oscillator. This would be an effective way to link the two model systems for free-phase oscillators that have been studied extensively via experiments, simulations, and theory, by our group: the 1D "rowers" [44, 64, 65, 169] and the circular rotors [32, 45, 60, 172].

Exploiting instead the possibility of driving the rotors along more complicated trajectory, in the future we plan on exploring the transition from an elliptical trajectory to a more structured "bean-shaped" trajectory. This would help us investigate what triggers the transition between the simple effective potentials that in my work constantly yield in-phase synchronisation in the elliptical case (Figure 6.7), and the more varied effective potentials found in Figure 6.6. More importantly, studying the transition between such different regimes would give insight into motile cilia synchronisation, as it could help identify regions in the parameter space where small changes in the driving parameters yield little variations in the effective potential (a scenario that would be desirable in carpets of synchronised cilia) and also regions where the driving potential is extremely susceptible to small changes in the driving parameters. The ability of a system to achieve considerable changes in its synchronisation state via small variations in its driving parameters would be desirable in some scenarios, and could help explaining for example the large scale changes of the cilia-driven flow in the brain during sleep [151], or the transition between the different synchronisation states of the two flagella of *Chlamydomonas* during the "run" and "tumble" phases of its motion [29, 47, 48].

Chapter 7

Conclusions and outlook

The problem of how cilia synchronise and coordinate to yield long range coordination when arranged in an epithelium is a complex one, that has implication for and requires tools and skill sets from several different fields. Within cell biology, the field is active in studying the metabolic path in ciliary motion, and the molecular structures involved in their assembly and function. Physicists are instead interested in how an efficient beating pattern is achieved to maximise fluid displacement, and, on a tissue scale, in how the collective phenomena, coordinated on a large scale, emerge starting only from local rules, and without a central organising node. Questions are still open regarding the importance of the cilia arrangement in a tissue, of their density and orientation, and of the rheological properties of the fluid surrounding them. Expanding our knowledge in this field would yield immediate applications that transcend from basic science, as the medical community is interested in exploring the link between cilia malfunction and various pathologies.

During my PhD I have studied the synchronisation of cilia in two ways: First, using a "top-down" approach, I have studied the large scale synchronisation of cilia in *in vitro* ciliated epithelia, by means of analysis of high speed microscopy videos. In the second part, on a smaller scale, I have studied the beating pattern of the single cilium, and how it is affected by ciliopathies. Finally, I have been working on a way to map the ciliary beat pattern onto a simple model system of free-phase oscillators.

In the first part of my PhD I have successfully applied Differential Dynamic Microscopy to characterise ciliated epithelia, demonstrating how it is possible to extract a wealth of often-overlooked information from microscopy videos: DDM allows to measure the ciliary beat frequency, the direction along which cilia are aligned, and the parameters of metachronal waves when present in the sample.

Extending on DDM I have developed a new approach, called multiscale DDM, that allows to measure the coordination length scale of a system: in this case, a characteristic length scale

over which cilia lose their phase-locking. This tool is particularly useful in examining *in vitro* ciliated epithelia, where cilia are usually not aligned on very large scales (but only locally), and metachronal coordination is not evident.

As a first and natural application of multiDDM, we have employed it to assess how the coordination of cilia in an *in vitro* epithelium is affected by changes in the rheology of the fluid they beat within. We show evidence that epithelia covered in thicker, more elastic, gel-like mucus, as the one covering the ciliated epithelia of patients affected by Cystic Fibrosis, are characterised by a larger coordination length scale. This property was then exploited to show that multiDDM can measure the effect of established and putative drugs on *in vitro* Cystic Fibrosis ciliated epithelia. In particular, novel information is unlocked by fully exploiting the multiscale nature of multiDDM: the coordination length scale measured on treated CF samples decreases, compared to an untreated CF control, partially recovering towards a healthy phenotype. This is also supported by the information obtained by monitoring the CBF, which is seen to increase in treated CF samples relative to untreated CF control samples. These results are really encouraging, hopefully paving the way to a widespread use of multiDDM as a tool for assessing the efficiency of new candidate medications.

In the second part of my PhD I moved towards the single-cilium scale, with the goal of linking the beating pattern of the cilia with a minimal model to study synchronisation. The idea was to build the tools needed to investigate how the shape of the beating pattern affects the coordination of cilia. As a first step, I developed an approach to quantitatively describe the beating pattern of single cilia. This part of the project is interesting in and of itself, as while high speed microscopy videos are routinely used in clinics to assess whether or not cilia in a sample beat with a normal pattern, the assessment tends to be a qualitatively or semi-quantitative one, that needs to be conducted by a trained physician. Accurately measuring the parameters of the beating pattern would help standardising the process, and highlight small differences and variations in the beating pattern that can be missed upon visual inspection and qualitative description. This application is explored in this thesis, as we track cilia from healthy individuals and from patients affected by two variants of PCD, obtaining a quantitative description of the beating pattern that yields a very complete information. We then show how by selecting a few meaningful, summary parameters (a "barcode" of the beat pattern), we can accurately discriminate between different mutations within Primary Ciliary Dyskinesia.

Finally, I worked towards linking the experimental data collected by accurately tracking the ciliary beat pattern with a minimal model that our group have been using to investigate hydrodynamic synchronisation. Such minimal model consists of two "rotors": simulated colloidal particles driven along a circular trajectory with a position dependent force. The phase

of each rotor is left free, and the two rotors are only coupled by hydrodynamic interactions. In this work I expanded on this existing model by finding a way to coarse-grain the parameters of the ciliary beat pattern onto the details of how the rotors are driven. This was achieved by calculating the trajectory of the "centre of drag" of the cilium throughout its beating cycle based on the experimental data, and approximating it with a closed, analytically described, parametric curve. The improved model system of "cilia-mimicking" rotors is then realised by driving the rotors along the analytical representation of the experimentally determined trajectory of the centre of drag. By running simulations on cilia-mimicking rotors based off several different experimental cilia both from healthy individuals and PCD patients, we show how the state of synchronisation of the rotors strongly varies with the shape of the driving trajectory.

The different tools I developed during my PhD, and the preliminary findings they allowed, can be used as starting points for future work in several directions. First and foremost, multi-DDM, the technique proposed in the first part of this thesis, is a superior tool to characterise ciliated epithelia, as it is a completely automatic analysis technique that yields a very complete information about how the cilia beat, their alignment, how their coordination decays with distance, and about metachronal waves. MultiDDM can be an extremely useful tool for all scientists and clinicians studying ciliated epithelia. For example multiDDM can be used to study how the alignment of the cilia, either *in vitro* on in a tissue, evolve during development. Clinicians, as we have demonstrated, can exploit the power of multiDDM in the context of assessing the effectiveness of candidate medications. Another possible application is to assess the structural and functional integrity of ciliated tissues, and if and how ciliated airways can recovery after being damaged, for example, by a blast wave which could lead to patchy loss of cilia. Coupled with an endoscope, multiDDM could even be used to conduct this type of assessments on *in vivo* ciliated epithelia.

The ability of multiDDM of extracting the characteristic scale of the dynamics of a system makes it a very general tool, that is not restricted to motile cilia. If a system is characterised by a scale for coherent or collective motion, this spatial scale will be highlighted by the process of comparing the dynamics across different tilings of the field of view. This is the main reason multiDDM is a good candidate for probing a variety of dynamically heterogeneous systems, both on a microscopic and macroscopic scale.

At the single-cilium level the quantitative analysis of the cilium beat pattern presented in this thesis, despite being quite straightforward and not extremely refined, already gives good results in terms of providing the user with a low dimensional, quantitative "barcode" of the beating pattern that captures the differences between different phenotypes. The obvious application for this analysis technique would be its refinement and implementation for diag-

nostic purposes: By building a large reference database of beating patterns upon imaging of cilia from patients with various ciliopathies we could train a supervised machine learning algorithm, that would then be able to help clinicians to correctly classify an "unknown" new sample. This diagnostic implementation would however realistically rely on the development of a software for the automatic tracking of cilia.

The colloidal oscillators, while a very simple and powerful model to study hydrodynamic synchronisation, can still be developed further to include other parameters, as of now not studied, that could be crucial for understanding synchronisation. For example viscoelasticity of the fluid should be implemented, as cilia in the airways beat in a non-Newtonian fluid. Moreover, the model of rotors used in this work is only accurate in approximating cilia in the far field, which is, when they are separated by a larger distance than their size. This is clearly not the case for the ciliated epithelia in the airways, where cilia are very densely packed. A much more detailed approach would require modelling elongated filaments. Such models, coupled with our quantitative assessment of the ciliary beat pattern, would also yields insights into the works of the molecular motors that power and regulate the bending of the cilium throughout its beating cycle.

The study of coordination of airway cilia conducted in my PhD both on a large and on a single-cilium scale, via experiments and simulations, has brought new insights, and new, powerful tools, towards understanding how the collective dynamics of motile cilia emerge. This remains however an extremely rich and complicated system, with many yet-unanswered questions, that still require the concerted efforts of researchers from different fields to be fully understood.

Appendix A

Testing DDM on synthetic datasets

In order to conclusively demonstrate the power of DDM to extract spatio/temporal correlation, its use is explored here on datasets (synthetic videos) that have known characteristics. In particular, it is interesting to understand what can contribute to a decay of the Image Structure Function with the lag time τ.

A.1 Phase drift yields decay of the Image Structure Function with the lag time

To investigate the cause of the ISF decay with the lag time we ran the DDM algorithm on synthetic videos of oscillators. Tweaking the properties of the individual oscillators, we are able to get an insight into the decay mechanism.

A.1.1 Perfectly phase-locked movement

In particular, we first create a synthetic video with phase-locked oscillators, that start off a random phase. To do so, a simple synthetic movie was devised to prove that the DDM algorithm, if run on a video of phase-locked oscillators, yields an Image Structure Function $I(q, \tau)$ that does not decay as a function of the lag-time τ. The DDM algorithm was thus run on a greyscale image with pixels changing their grey level (or "intensity") as a function of time. The image is a 480×480 matrix, and the pixel intensity is an 8-bit unsigned integer variable (between 0 and 255). The intensity $M_{i,j}$ of the i, j-th pixel at time t is given by

$$M_{i,j}(t) = 127 + 127 \sin(2\pi\nu_0 t + \varphi_{i,j}), \tag{A.1}$$

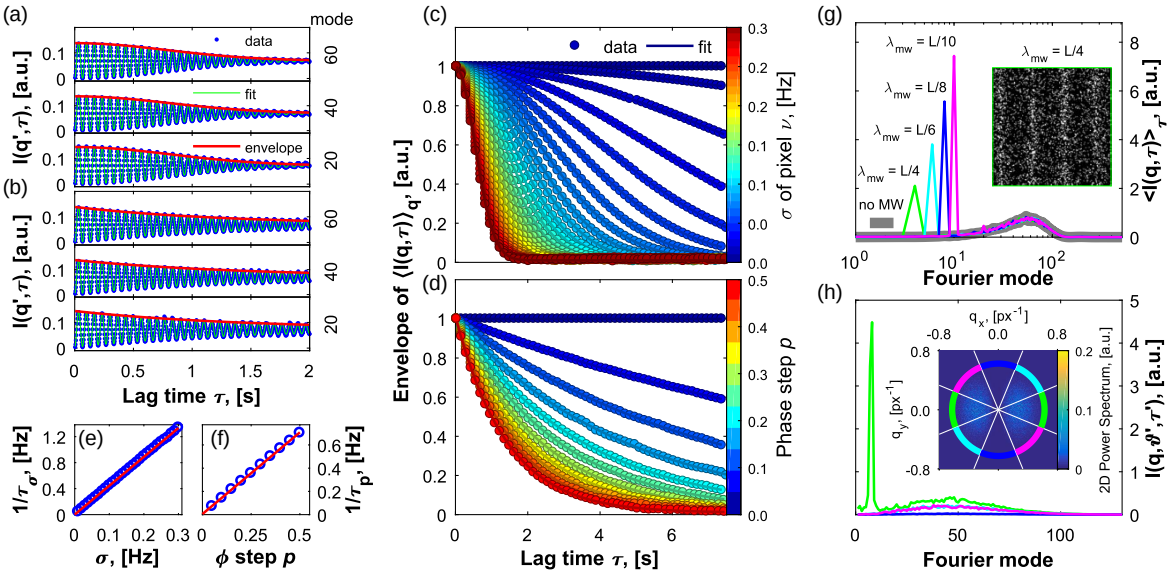

Fig. A.1 **Image Structure Function gives access to information on phase coherence and anisotropy in the sample's dynamics. (a-f)** We simulate here (see section A.1) oscillators that are not completely phase-locked. The envelopes of the Fourier mode amplitudes decay with a timescale τ. In **(a, c, e)**, the frequencies of the oscillators are drawn from a distribution of finite width σ. In **(b, d, f)** instead all the oscillators have the same frequency but their phase undergoes a random walk with step probability p. In both cases the lack of any special length scale in the simulated data yields no q-dependence in the DDM output. **(a, b)** Behaviour with τ of the amplitude of three Fourier modes: $I(q', \tau)$ curves are fitted (green line) with the models in eq. (A.3) and eq. (A.6). Information about the decay can be obtained simply by fitting the envelopes (red lines) of the $I(q', \tau)$ curves with eq. (A.4) and eq. (A.7). **(c)** The same type of simulation as in **(a)** was repeated changing the width σ of the frequency distribution. Here the envelope of $\langle I(q, \tau) \rangle_q$ is drawn (dots) for various values of σ. The data are then fitted (continuous lines) with eq. (A.4). **(e)** The decay time τ_σ was found to be $\propto 1/\sigma$. **(d)** Similarly, the envelopes of $\langle I(q, \tau) \rangle_q$ obtained by changing the phase-step probability p are plotted (dots), and fitted (continues lines) with eq. (A.7). **(f)** The decay time τ_p was found to be $\propto 1/p$. **(g-h)** DDM was run on synthetic data, generated so to have a travelling longitudinal wave moving leftwards (see section A.2). **(g)** A travelling wave shows up as a sharp peak in the DDM signal. Changing the periodicity of the metachronal wave in the simulations (see section A.2) reflects in a change of the spatial frequency of the peak, while the broader maximum of the spectrum (due to the oscillating dots) is not affected. The inset shows a still frame from the synthetic videos. **(h)** Each curve is the average of the 2D power spectrum over the angles labelled with the corresponding colour in the inset. The peak signature of the metachronal wave shows only in the spectrum obtained averaging the sector with $\vartheta \in \left[-\frac{\pi}{8}, +\frac{\pi}{8}\right]$, ϑ being the angle between $\mathbf{q}$ and the horizontal axis. The amplitude of the broader signal due to the oscillation of the dots has a maximum in this sector as well, and it goes to zero in the perpendicular direction.

where $\varphi_{i,j}$, the phase, is for each pixel a random number between 0 and 2π, while $\nu_0 = 15\,\mathrm{Hz}$ is the frequency, constant across all pixels. The time t is a multiple of the simulation time step $\Delta t = 1/300\,\mathrm{s}$. The intensity of all pixels therefore oscillates between 0 and 254 as a sine function with the same period, and the phase difference between pixels is constant in time. In this case, there is no q-dependence: as all pixels start off a randomly distributed phase there is no spatial periodicity or particular length scale in the differential images to yield a structured power spectrum. This synthetic video, with perfectly phase-locked oscillators, was seen to yield no decay of the ISF: as the correlation between oscillators does not decay, neither does $I(q', \tau)$.

A.1.2 Phase drift due to spatial heterogeneity

The second type of synthetic video is used to investigate whether, as hypothesised in section 3.3.1, the ISF decays because cilia within the same field of view beat with slightly different frequencies. We implement oscillators with frequencies drawn from a normal distribution centred in ν_0, and with standard deviation σ, starting off at a random phase. The simulation is still based on a 480×480 greyscale matrix with pixels changing intensity over time, except that in this case the intensity $M_{i,j}$ of the i, j-th pixel follows

$$M_{i,j}(t) = 127 + 127\sin(2\pi\nu_{i,j}t + \varphi_{i,j}), \tag{A.2}$$

where the frequency $\nu_{i,j}$ is drawn for each pixel from a normal distribution peaked at $15\,\mathrm{Hz}$ and with standard deviation $\sigma = 0.2\,\mathrm{Hz}$. The randomness in the starting phase yields again no appreciable q-dependence of the $I(q, \tau)$ signal. On the other hand introducing a finite width in the distribution of the frequencies does affect the behaviour of $I(q', \tau)$ that oscillates and decays exponentially with the second power of τ. In particular, as shown in Figure A.1, the oscillating signal can be fitted with

$$I(q', \tau) = A\left(1 - \cos(2\pi\nu\tau)\mathrm{e}^{-\tau^2/\tau_\sigma^2}\right) + B. \tag{A.3}$$

The frequency as calculated from the fit is, unsurprisingly, $\nu = \langle\nu_{i,j}\rangle_{i,j}$.

The simulation was repeated for several values of the standard deviation σ of the frequency distribution. As the $I(q, \tau)$ signal consistently showed no appreciable trend with q, the decay time τ_σ was calculated by fitting the envelope of the average $\langle I(q, \tau)\rangle_q$ of the $I(q', \tau)$ curves as

$$E(\tau) = A\mathrm{e}^{-\tau^2/\tau_\sigma^2} + B. \tag{A.4}$$

As shown in Figure A.1e the decay time τ_σ is inversely proportional to the width σ of the frequency distribution, hence the larger the spread in the frequencies of the oscillators in the field of view, the faster the amplitude of the oscillations in the $I(q', \tau)$ signal decays.

A.1.3 Phase drift due to phase noise

To test our second hypothesis for the decay of the ISF, which is that there is some drift in the phase of each cilium (imperfect coherence, expected not at least due to thermal noise), a third type of synthetic video was devised. The oscillators here beat with the same base frequency ν_0, but their phase undergoes a random walk with step probability p.

The simulation to test this hypothesis is still based on a 480×480 matrix of 8-bit unsigned integer pixels, the intensity of which changes in time as a sine function with frequency $\nu_0 = 15\,\mathrm{Hz}$, same for all pixels. Unlike in the previous simulations, the phase of each pixel intensity is not a constant in time. In fact, at each step of the simulation (i.e. at each Δt, so $\frac{1}{\Delta t}\frac{1}{\nu} = 20$ times per cycle) the phase can take a step of $\pm\pi/32$ with probability p (also called a "phase-step"). In other words, the intensity of pixels will be

$$M_{i,j}(t) = 127 + 127\sin(2\pi\nu_0 t + \varphi_{i,j}(t)), \tag{A.5}$$

where the phase $\varphi_{i,j}(t)$ undergoes a (one-dimensional) random walk with probability p centred at the starting point $\varphi_{i,j}(t = 0)$ that simulates a phase noise.

The output of the DDM analysis on this simulation bears some similarities to the one in section A.1.2: no q-dependence and $I(q', \tau)$ oscillating and decaying with the lag time τ. But while in section A.1.2 $I(q', \tau)$ would decay due to heterogeneity following eq. (A.3) i.e. as a negative exponential with τ^2, here the data show a linear decay envelope

$$I(q', \tau) = A\left(1 - \cos(2\pi\nu\tau)\mathrm{e}^{-\tau/\tau_p}\right) + B, \tag{A.6}$$

and consequently, as shown in Figure A.1d, the envelopes of the $I(q', \tau)$ curves are fitted by

$$E(q', \tau) = A\mathrm{e}^{-\tau/\tau_p} + B, \tag{A.7}$$

retrieving $\nu = \nu_0$. In order to understand how the characteristic time τ_p depends on the phase-step probability p the simulation was repeated for different values of p. As shown in Figure A.1f τ_p is inversely proportional to p: the less the oscillation of each pixel is regular, the faster the $I(q', \tau)$ signal decays with the lag time τ.

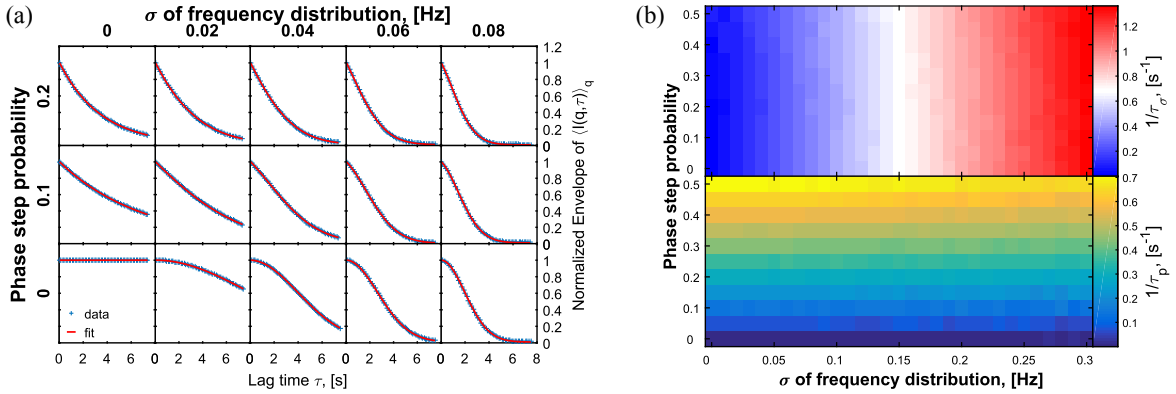

Fig. A.2 **Different contributions to the phase drift affect the Image Structure Function in different ways. (a)** Each sub-plot shows the envelope (dots) of the $\langle I(q,\tau)\rangle_q$ for the simulations explained in section A.1.4. The parameters of the simulations change along the rows and columns of the figure: the distribution from which the pixel frequencies are drawn broadens from left to right, and the probability of phase-steps increases from the bottom to the top. The red curves are fits of the data following eq. (A.9). The statistical error on the data is of the same size of the markers. **(b)** Heat maps of the decay times for the simulations described in section A.1.4. From this panel it is clear that the two contributions to the decay of the $\langle I(q,\tau)\rangle_q$ curves are independent: τ_σ only depends on the spread σ of the frequency distribution, while τ_p only on the probability p of a phase-step.

A.1.4 How contributions to the decay combine

Having established that at least two factors can affect the decay of the ISF, the next step is understanding how the two contributions combine. The DDM algorithm is thus run on a synthetic video of oscillators with frequencies drawn from a normal distribution around ν_0 with standard deviation σ, and whose phase undergoes a random walk with step probability p.

In more detail, the DDM algorithm was run on a 480×480 matrix of 8-bit unsigned integer pixels, the intensity $M_{i,j}(t)$ of which changes in time according to

$$M_{i,j}(t) = 127 + 127\sin(2\pi\nu_{i,j}t + \varphi_{i,j}(t)), \tag{A.8}$$

where each pixel frequency $\nu_{i,j}$ is drawn from a normal distribution centred at $\nu_0 = 15\,\mathrm{Hz}$ with width σ, and the phase $\varphi_{i,j}(t)$ undergoes a (one-dimensional) random walk with probability p centred at the starting point $\varphi_{i,j}(t=0)$, which is a random number between 0 and 2π.

This simulation was run several times, changing the two parameters σ and p. Results are shown in Figure A.2a. As the goal of these simulation was to better understand the decay with τ, and as the $I(q,\tau)$ signal showed no q-dependence, only the envelope of the $\langle I(q,\tau)\rangle_q$

curve is plotted for each combination of values for σ, p. Each envelope curve is then fitted as

$$E_{\sigma,p}(\tau) = A\mathrm{e}^{-(\tau^2/\tau_\sigma^2)-(\tau/\tau_p)} + B, \tag{A.9}$$

meaning that the two contributions affect the decay independently. This claim is substantiated by Figure A.2b, in which the reciprocals of the decay times τ_σ and τ_p are shown in a heat map as a function of the two simulation parameters $\sigma$and p. As the figure shows, changing one of the two parameters only affects the corresponding decay time, but not the other.

A.2 Metachronal wave detection

As we saw in section 3.3.3, DDM is well suited to detect metachronal waves. A simple synthetic dataset was used to demonstrate in depth how DDM based approach can recover metachronal wave dynamics. The synthetic videos feature finite-size oscillating dots whose initial phases are assigned so to have a longitudinal wave along the x-axis. In detail, 4096 dots of $8\,\mathrm{px}$ diameter whose initial positions are randomly assigned on a 1024×1024 matrix are made to oscillate along the x-axis following a sine function. The frequency ν_0 is the same for all the dots. The time step of the simulation is $\Delta t = 1/200\,\mathrm{s}$. The simulation runs for 2000 time steps Δt. The metachronal wave is implemented by giving the oscillating dots an initial phase directly proportional to their x coordinate. The position of the i-th dot at time t is thus given by

$$\begin{cases} x_i(t) = x_i^0 + A\sin(2\pi\nu_0 t + \varphi_i) \\ y_i(t) = y_i^0 \end{cases} \tag{A.10}$$

with the initial phase $\varphi_i \propto x_i^0$. The DDM algorithm is run on the whole 1024×1024 field of view.

The Image Structure Function $I(q, \tau)$, unsurprisingly, oscillates with τ. More interestingly, the metachronal wave sets a spatial length scale that is highlighted by the Fourier transform. This is particularly evident when plotting the lag-time averaged 1D power spectrum (Figure A.1g): apart from the broad maximum caused by the dots oscillating, there is also a sharp peak at smaller Fourier modes. The simulation was run changing the wavelength of the metachronal wave, and the power spectra are shown in Figure A.1g. The grey thick line is obtained by having the oscillating dots to start off a random phase. This yields no metachronal wave, and it shows in the power spectrum $I(q, \tau')$ as there is only one broad maximum. The green, light blue, navy and magenta lines are the result of runs in which the metachronal wave has a wavelength of respectively $1/4$, $1/6$, $1/8$ and $1/10$ the size L of the field of view. These spectra, in addition to the broad maximum, show a sharp peak each, at

mode respectively 4, 6, 8 and 10, that correspond to the metachronal wave wavelengths. This shows that the peaks are the signature of the metachronal waves.

A.3 Length scale of synchronisation: numerical data

Further proof of the ability of the DDM algorithm in finding an estimate for the length scale of synchronisation comes from the analysis of another specific simulation. As in sections A.1 and A.2 this synthetic dataset is used to demonstrate in very controlled conditions how the multiscale-DDM approach works. The simulation is based on a greyscale matrix of pixels with intensity oscillating in time as a sine starting off at a random phase. The matrix is divided in hexagonal tiles, and all pixels within the same tile oscillate with the same frequency. Pixels in different tiles can have different frequencies. Tile frequencies are drawn from a normal distribution peaked at $\nu_0 = 15\,\mathrm{Hz}$ and with standard deviation $\sigma = 0.2\,\mathrm{Hz}$. As with real data, the simulated video is divided in regions (windows) of decreasing size, and for each size all regions are analysed with the DDM algorithm. For each region the very same analysis as in section A.1.2 applies, yielding a single value of the decay time τ_σ. Values of τ_σ measured from different windows of the same size are averaged. Figure 3.7a shows that, as in real data, the decay time τ_σ diverges as the size of the DDM window becomes smaller than the size of the tile. The transition is not sharp because of the mismatch in shape between the square DDM window and the hexagonal frequency tile (i.e. each square window can probe pixels belonging to at least two different tiles). The simulation could have been carried out with square frequency tiles, but the hexagonal tiles were chosen to make the simulation closer to the real conditions, where it is highly probable that a square DDM window chosen *a priori* will probe cilia belonging to multiple cells.

A.4 Anisotropic dynamics

One of the approximations made when explaining the algorithm in section 3.3 was to analyse the sample as if it were isotropic, thus taking a radial average of the 2D Fourier transform of differential images. This allows to have a power spectrum that only depends on the spatial frequency, which is the magnitude of the scattering vector, discarding the direction of the latter. In a slightly more sophisticated analysis, one might want to maintain information about anisotropy in the sample when using the DDM algorithm. Let ϑ be the angle between the scattering vector $\mathbf{q}$ and the horizontal axis. An easy way of keeping the information about anisotropy is to bin ϑ and to do a radial average only within each bin. Changing the bins allows to tune the resolution in ϑ, or to pick the signal only for certain ranges of ϑ [104, 111].

An example of using DDM maintaining the angular information is in Figure A.1h, which shows a sample image from the DDM algorithm run on the simulation described in section A.2. The direction of oscillation of the dots, and more importantly the direction of propagation of the metachronal wave, are successfully retrieved.

Appendix B

Metachronal waves in *in vitro* samples

In section 3.3.3 it is explained how DDM can provide a completely automated measurement of the wavelength of a metachronal wave. The result thus obtained was cross-checked manually, as per the following video analysis procedure.

B.1 Manual measurement of metachronal wave on *in vitro* samples

The high speed video B.1 was processed by taking algebraic differences between subsequent frames, and then calculating the local standard deviation of each differential frame. This type of processing highlights areas with more movement and suppresses the static contributions to the signal given by the background (Video B.2). Eleven measuring lines, parallel to each other and separated by a distance of $1\,\mathrm{px}$ were selected along the direction of propagation of the wave, and used to define as many cross-sections of the processed video. Averaging across the cross-sections yielded the kymograph shown in Figure 3.6b. This is a particularly straightforward, albeit cumbersome, fashion of manually measuring the wave's parameters: to obtain the wave velocity c from the kymograph one only has to take the reciprocal of the slope of the bright regions. Knowing the CBF ν the wavenumber was then obtained by $q_{wave} = 2\pi\nu/c$ and found to be consistent with the location of the q-peak in the Image Structure Function.

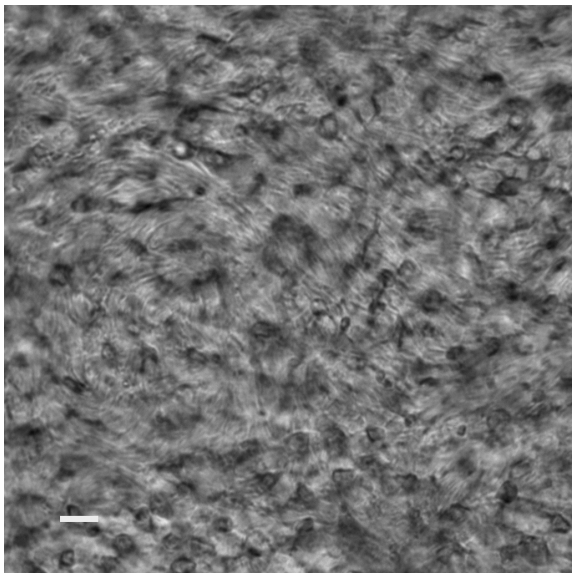

Fig. B.1 **Metachronal coordination in an *in vitro* sample.** Raw microscopy video of cilia beating, slowed down by a factor of 5, showing metachronal coordination. Scale bar is $10\,\mu\mathrm{m}$. The video can either be accessed by clicking on the preview above, or as part of the Supporting Materials of [143].

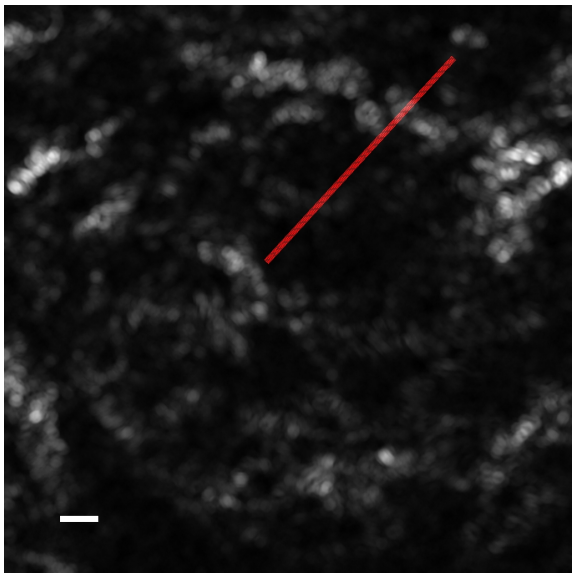

Fig. B.2 **Manual measurement of a metachronal wave.** Movie processed to highlight the metachronal wave: First we take the algebraic difference of each couple of subsequent frames of Video B.1. Each frame of the differential video is then filtered using a local standard deviation filter. Areas of Video B.1 with the most movement are thus highlighted to have a high signal (white) in the processed video. The measuring lines for the procedure described in section B.1 are shown here in red. Scale bar is $10\,\mu\mathrm{m}$. The video can either be accessed by clicking on the preview above, or as part of the Supporting Materials of [143].

Appendix C

Optical flow analysis of High Speed Microscopy Videos of motile cilia

MultiDDM is a very powerful tool to characterise ciliated epithelia on a large scale, but high speed microscopy videos imaging a few cells from the side need to be analysed in a different way (Figure 5.1, Figure C.1 for example images). While chapter 5 presents a single-cilium-oriented analysis, focused on reconstructing the ciliary beating pattern by tracking a moving cilium, here we report an alternative method we used in the attempt of studying the coordinated motion - in particular metachronal waves - of motile cilia. Inspired by [59] we attempted to employ an optical flow algorithm to measure the velocity field of moving cilia. Crucially, we didn't use a suspension of tracer colloidal particles near the ciliated epithelium, but we employed the optical flow algorithm on the cilia themselves, somewhat similar to what previously done in [79].

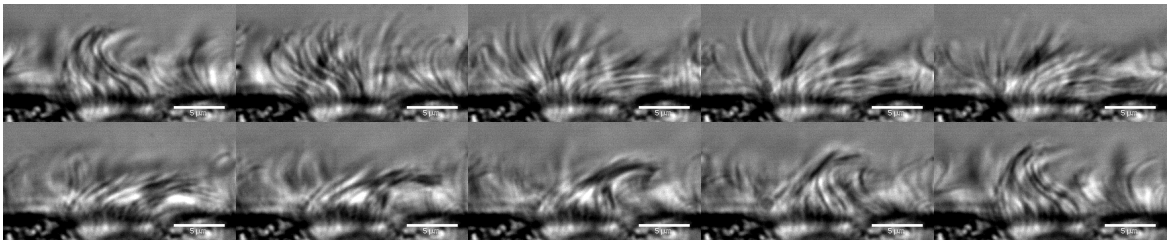

Fig. C.1 **Cilia imaged from the side.** Power **(top row)** and recovery **(bottom row)** stroke in a healthy sample imaged from the side, as sketched in Figure 5.1. Scale bar is $5\,\mu\mathrm{m}$.

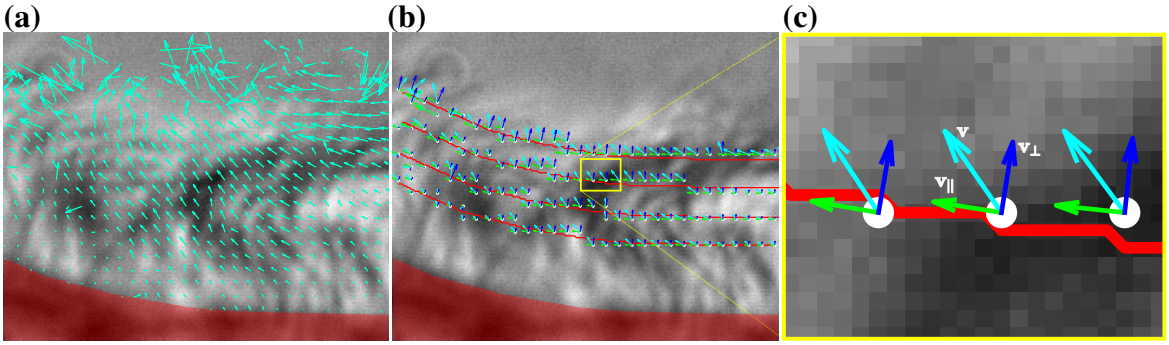

Fig. C.2 **Extracting information from optical flow algorithm results.** Out of all the vectors of the velocity field (cyan) output of PIVlab **(a)** we select the ones closest to the measuring lines **(b)**. The measuring lines (red lines) are selected so to be parallel to the cell surface (red mask) at increasing distances from it (here at 2.5, 3.5, 4.5, and 5.5 µm). **(b, c)** Each of the velocity vectors $\mathbf{v}$ is decomposed onto the local reference system defined by the measuring line in its two components $\mathbf{v}_{\parallel}$ (green) and $\mathbf{v}_{\perp}$ (blue).

C.1 Short primer on optical flow

The common element of optical flow algorithms is that they measure a displacement field between two consecutive frames of a video [79]. This goal can then be achieved in several ways, but here I will only report one of the most common methods that is used in the software we employed in this work (PIVlab, [176]).

First the images in the video are pre-processed, to maximise their contrast and improve readability in general, and the first image in a pair is divided into several small subregions. Each subregion (the "template") is in turn looked for in the second frame (or a subregion of it - the "interrogation area") by the algorithm. This is achieved by calculating, either in the direct or Fourier space, the cross-correlation of the template and the interrogation area. The position of the peak of the cross-correlation yields the displacement of the template between the two frames examined. Finally, the vector field thus obtained is post-processed: vectors are validated by setting a threshold for a maximum displacement, the vector field is interpolated where the outliers fail the validation, and the result is smoothed to reduce the noise [176].

C.2 Data exploration

After Dr Chioccioli had processed the microscope videos using PIVlab we analysed the results using a custom MATLAB software.

The software was developed with the goal of measuring parameters of the cilia beating at different distances from the cell surface. To do so, the cell surface is first identified by the user and covered by a binary mask (red region in C.2). The binary mask is dilated (`imdilate`,

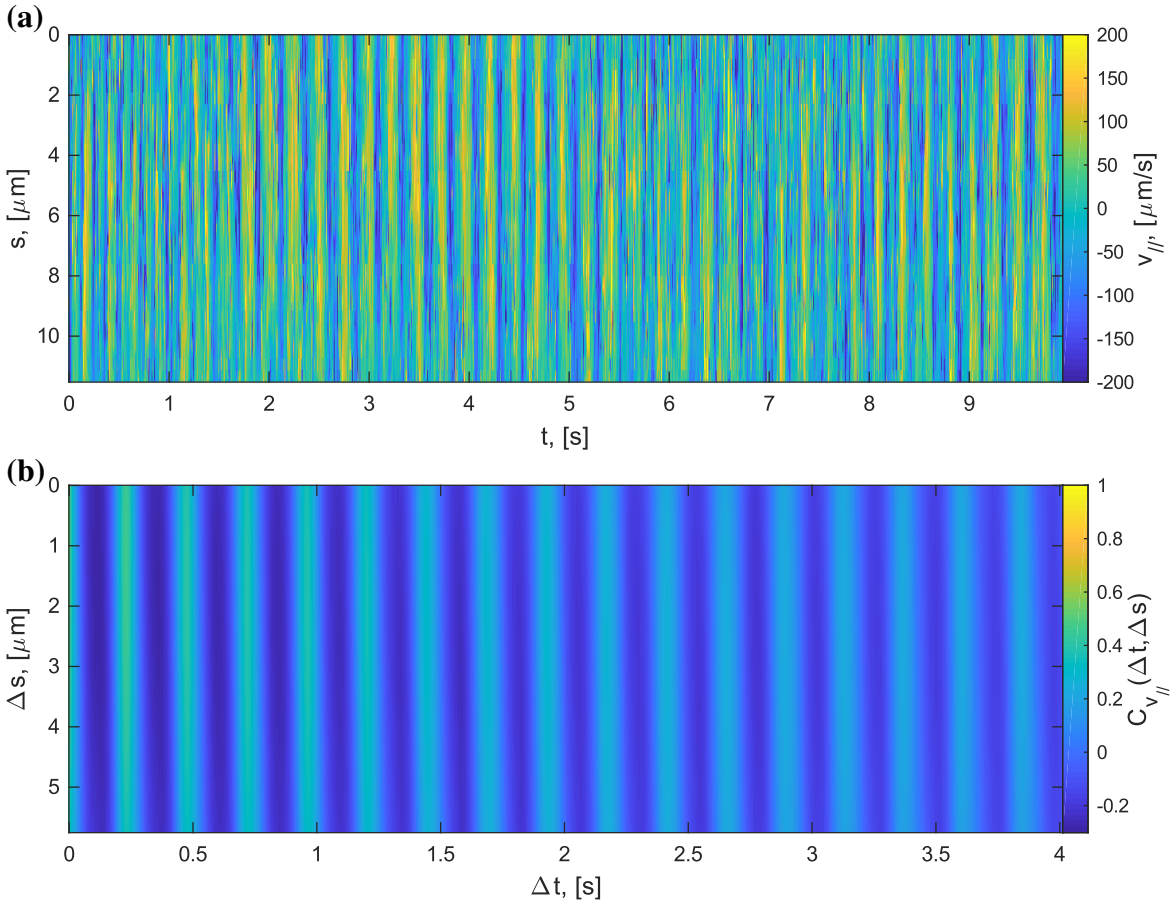

Fig. C.3 **Optical flow algorithm measures CBF. (a)** Kymograph of $\mathbf{v}_{\|}$. To get a cleaner signal we take its autocorrelation **(b)**, from which we can measure the CBF and, if the video showed a metachronal wave, its wavelength.

MATLAB), using a disk of radius h as structuring element. A "measuring line", parallel to the cell surface and at a constant distance h from it, is obtained by taking the edge of the dilated mask.

As the focus is on analysing the velocity of cilia parallel to the cell surface, the values of the velocity field obtained by PIVlab are decomposed in their components in the set of axes defined locally by the measuring line (Figure C.2). PIVlab works on a grid with spacing of a few pixels, so the values of $\mathbf{v}_{\|}$ need to be interpolated to have a smooth quantity all along the measuring line: at each point, the interpolated value is the average, weighted with the distance from the point, of the two closest values of $\mathbf{v}_{\|}$ measured on the PIV grid. This is tantamount to a linear interpolation, but deals with the fact that the points where PIVlab evaluated the velocity might not lie on the measuring line. The values of $\mathbf{v}_{\|}$ along each measuring line, and for each couple of frames, create a kymograph (Figure C.3a).

To further clean the data we take the autocorrelation of the velocity kymograph (Figure C.3b) over space and time. The CBF can then be measured as the frequency of the very clear oscillations in time. If the video captured a section of a metachronal wave then this translates into slanted ridges in the autocorrelation of the velocity kymograph, and the wave number can be obtained by measuring their slope.

C.3 Considerations about the optical flow analysis of cilia

We encountered a series of problems when analysing side-view videos of cilia beating with the optical flow algorithm. Most notably the cilia have poor contrast, and their contrast changes sign as they cross the focal plane, with the cilium going from darker than the background to brighter. This can be a problem for optical flow algorithms, as they are based on the assumption that intensity variations in the image are only caused by movement of the objects, meaning that the objects in the field of view should have constant brightness (at least on short time intervals) [79].

Another important problem is caused by the finite depth of field of the microscope objective, as often a microscopy video featured cilia in the background moving out-of-phase with cilia in the foreground. This can lead to underestimating the displacements, and in general to a poorer match of the "template" with the "interrogation area" in the following frame.

Despite these issues we did manage to obtain very reliable measurements of the CBF from the side-view videos, although as the samples are imaged at room temperature and CBF is temperature-dependent [177] these values are not very informative.

We eventually settled on working with multiDDM and reconstruction of the beat pattern: multiDDM is superior in reliability, throughput, wealth of information yielded, and statistics, and is therefore the natural choice for many-cilia analysis. For the single cilium the reconstruction of the beating pattern, that we initially tried only as a way to validate optical flow measurements, actually yields more complete information.

It could however be worth it in the future to try a different approach to this challenge: many laboratories work with nasal brushings, in which cilia are seen from the side [178–181], and the analysis described in this Appendix is less taxing than the pattern reconstruction detailed in chapter 5. Analysis with a different optical flow algorithm [79–81, 83, 182] coupled with better preprocessing of the image and a temperature-controlled imaging chamber could in our opinion yield interesting results.

Appendix D

Fluid transport in the Periciliary Layer

The seminal work of Button and collaborators shed light on the composition of the periciliary layer (PCL) showing how the latter is occupied by mucins grafted to the surface of the cilia that create a brush with mesh size increasing with the distance from the cell surface [43]. How the liquid trapped in this brush is propelled by the cilia is however still an open question: earlier studies have measured the displacement of fluorescent dyes localised in the PCL [183], but haven't managed to study how the displacement varies, within the PCL, with the distance from the apical surface of the epithelium. Moreover, while [183] found extremely reduced fluid transport after removal of the mucus layer, the same result was not observed in a more recent study [184] that used tracer particles on mucus-washed epithelial tissues.

In this Appendix we present very preliminary experiments that could yield some insight into how the PCL is moved (if at all) by the coordinated beating of cilia. Briefly, as shown in Figure D.1, we image cilia from the side, photoactivate a fluorescent dye in a localised region within the PCL, and follow the displacement of the dye over time.

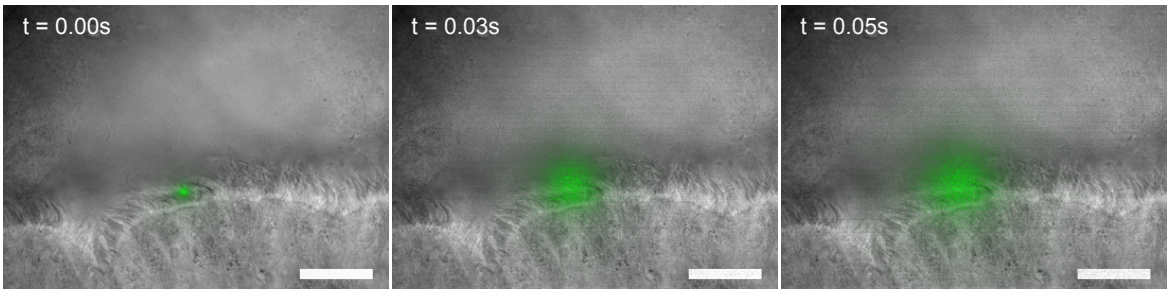

Fig. D.1 **Measurement of PCL transport with photoactivated fluorescent dye.** After being photoactivated, the fluorescent dye diffuses and is transported by the cilia beating. Scale bar is $20\,\mu\mathrm{m}$.

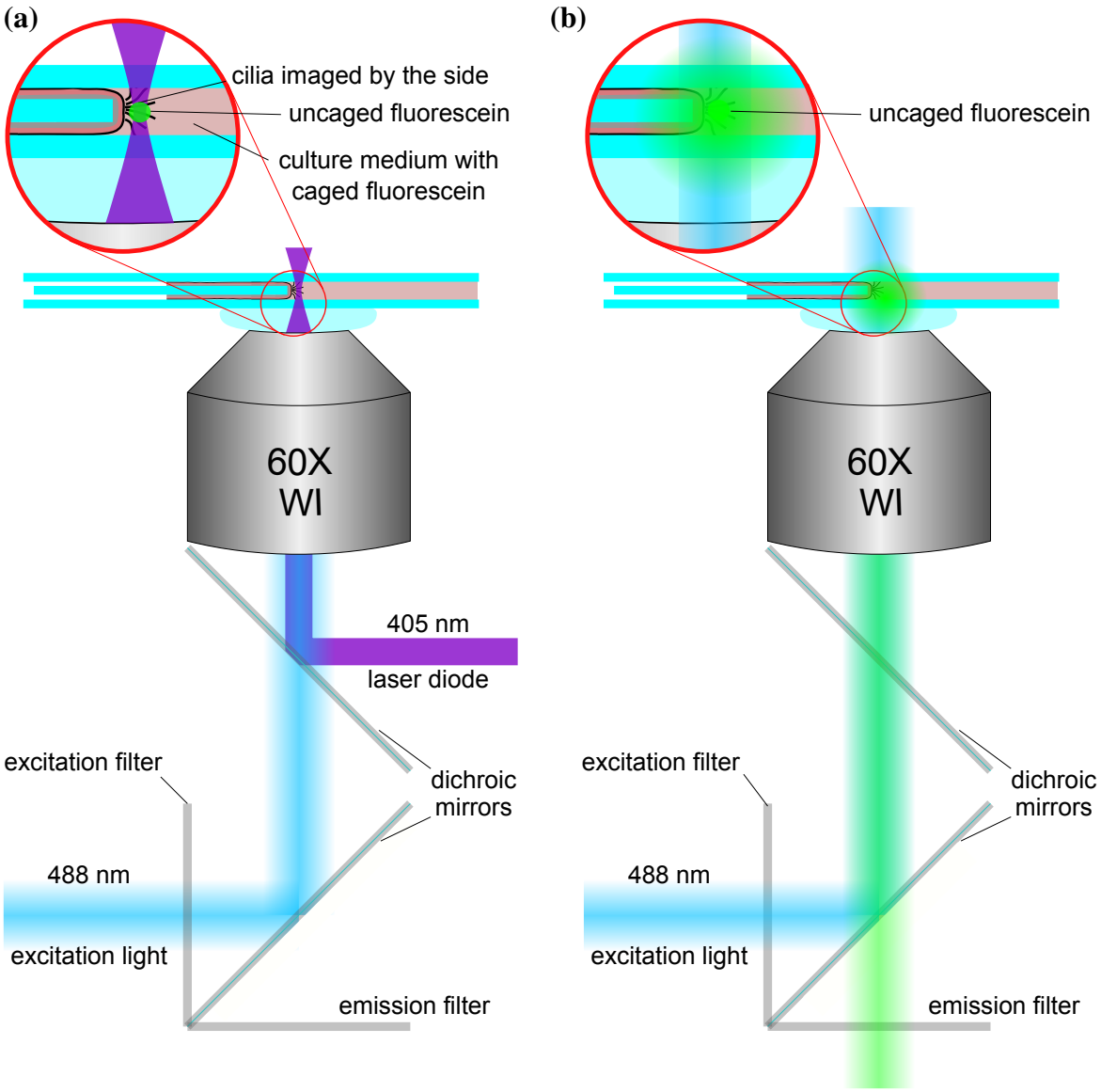

Fig. D.2 **Schematic representation of the experimental set-up. (a)** A $16\,\mathrm{ms}$ pulse of collimated $405\,\mathrm{nm}$ light from a laser diode, focused by the objective onto a $\sim 1.5\,\mu\mathrm{m}$ radius spot activates the caged fluorescent dye. **(b)** After the pulse we image how the activated fluorescent dye diffuses and is moved by the cilia.

D.1 Experimental methods

The optical set-up was designed and purpose-built by Dr Jurij Kotar (Figure D.2), and the experiments were conducted in collaboration with him and Dr Maurizio Chioccioli.

A Healthy Human Airway Epithelium reconstituted *in vitro* (MucilAir™) was purchased from Epithelix (Epithelix Sàrl, Geneva, Switzerland) and maintained following the protocol provided by the company.

To image the cells from the side we excised the membrane supporting the epithelium and folded it between two coverslips as detailed in Figure 5.1, together with some culture medium and photoactivated fluorescent dye (F7103, Thermo Fisher Scientific, Waltham, Massachusetts, USA) in PBS (final concentration $\sim 1\,\mathrm{mM}$).

We used a $16\,\mathrm{ms}$ pulse of $405\,\mathrm{nm}$ collimated light from a $200\,\mathrm{mW}$ laser diode (SLD3237VF, Sony, Tokyo, Japan) focused through the objective to uncage the fluorescent dye in a $\sim 1.5\,\mu\mathrm{m}$ radius spot within the PCL.

Photoactivation and imaging was done on a Nikon Eclipse Ti-E inverted microscope (Nikon, Japan), equipped with a $60\times$ water immersion objective ($\mathrm{NA} = 1.2$, Nikon, Japan) and a further $1.5\times$ magnification in the optical path ($1\,\mathrm{px} = 0.065\,\mu\mathrm{m}$). Videos were acquired using a CMOS camera (GS3-U3-23S6M-C, FLIR Integrated Imaging Solutions Inc., Canada), with frame rate set at $100\,\mathrm{fps}$.

D.2 Image Analysis

After photoactivating the fluorescent dye in a localised spot in the PCL we measure how the fluorescent patch moves along the ciliated epithelium.

First, we define a "measuring line". This is at the moment implemented in two ways: for an almost completely automated analysis the PCL is identified with minimal user input as the region of the field of view where movement is detected (e.g. red shaded region in Figure D.3a), and then fitted with a parametric line (the measuring line). In the alternative and slightly more hands-on approach the user needs to trace the boundary of the cell surface obtaining a binary mask, and then to dilate it until its edge (the measuring line) is at the desired distance from the cell surface. Ideally, the measuring line is chosen so that it passes through the photoactivating light spot.

The measuring line is dilated into a $20\,\mathrm{px}$ thick "measuring strip" for better statistics: the quantities that we measure in a point will be averaged over the small region of space perpendicular to the measuring line at that point. The measuring strip is orientated by the user so that its arclength increases (coloured thin region, from blue to yellow, in Figure D.3a) in the direction of the power stroke.

In each frame after the activation of the dye we measure the fluorescence intensity along the measuring strip and fit it with a Gaussian curve

$$f(s) = A\mathrm{e}^{-\frac{1}{2}\left(\frac{s-s_0}{\sigma}\right)^2} + c.$$

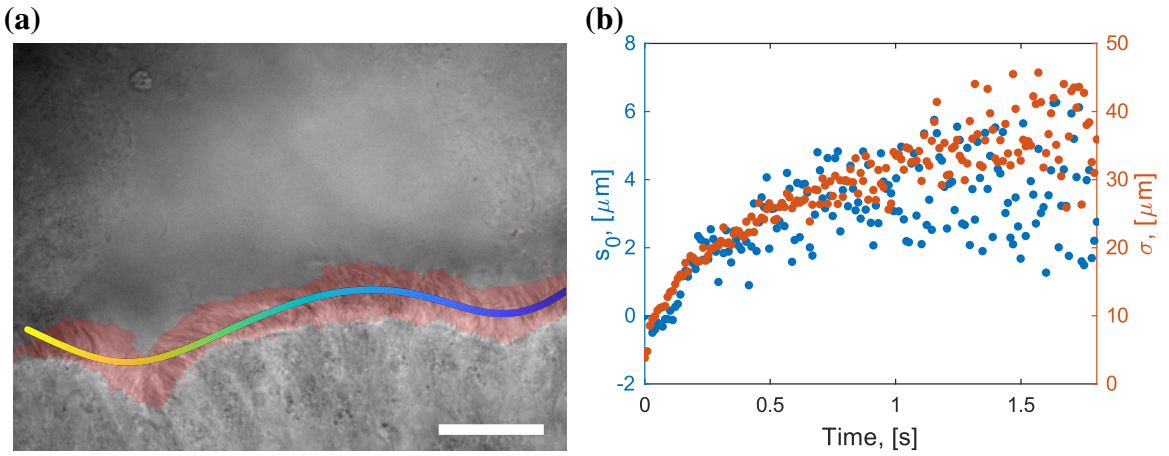

Fig. D.3 **Tracking of the fluorescent dye measures PCL transport. (a)** We measure the fluorescent intensity profile along a "measuring strip" orientated (blue to yellow) in the direction of the power stroke. The measuring strip in this figure is found automatically as dilation of a parametric line that fits the PCL region, detected with a motion detection algorithm. Scale bar is $20\,\mu\mathrm{m}$. **(b)** The mean (blue dots) and width (red dots) of the Gaussian profile fitted to the fluorescence intensity along the measuring strip show respectively how the fluorescent dye is transported in the direction of the power stroke and diffuses over time.

Its mean $s_0(t)$ and width $\sigma(t)$ yield respectively the displacement of the centre of the fluorescent patch and its spread along the measuring line over time (Figure D.3b).

D.3 Considerations and outlook

The experimental set-up and analysis presented in this Appendix represent a step forward towards understanding how the PCL is moved by the cilia beating.

The preliminary experiments carried out during my PhD showed us that it is possible to localise a caged fluorescent compound into the PCL, and that by activating the dye and tracking it we can measure the PCL transport. However, in order to get definitive results to compare with the existing literature about experiments [183, 184] and numerical simulations [185] on PCL transport more experiments and some refinement to the analysis are needed.

Experiments-wise, more videos need to be taken both in the presence and absence of mucus, to study how the layer of mucus affects the PCL transport. Moreover, while the procedure of folding the membrane supporting the ciliated epithelium and imaging its edge is quick and delivers good quality videos, it often yields unexpected geometries in how the epithelium itself is arranged, and this could affect the validity of the experiments. Alternative assays or imaging set-ups in which side-view high-speed videos of the PCL can be recorded in more controlled conditions would be invaluable towards obtaining meaningful results.

Tracers (e.g. colloidal beads) could be added to the medium as well, in order to measure the fluid flow outside of the region where the fluorescence dye diffuses - this would give us a measurement of the transport both of the PCL and of the fluid above the cilia (either mucus or culture medium) at the same time. The assay could also be used to study the effect of drugs and stimulants on the beating cilia.

For what concerns the analysis, an obvious improvement could be to have multiple measuring lines, all strictly parallel to the cell surface and at increasing distances from it, so to measure the transport as a function of the position within the PCL.

In conclusion, in this Appendix we presented preliminary experiments and analysis to measure fluid transport within the PCL, and suggested possible ways to further improve on the experimental set-up and analysis. The approach presented should yield interesting results and, possibly in conjunction with numerical simulations, help to give insight into the hydrodynamics of ciliated epithelia.

Appendix E

Details of the colloidal rotors simulations

This Appendix gives a few extra details in how the simulations of the colloidal rotors are realised. The first section details the procedure implemented to find the phase of a rotor along its prescribed trajectory. As explained in chapter 6, in particular in section 6.3, when dealing with trajectories of general shape and non constant driving force this is not a trivial feat to achieve without slowing down the simulation considerably. A second section reports the parameters used to run the simulations featured in this thesis.

E.1 Projection of a rotor onto its prescribed trajectory

Given a bead at position $\mathbf{r}^b$, typically not lying on its prescribed trajectory $\tilde{\mathbf{r}}_{cod}(\Phi)$, we need to find a value of the phase Φ^* that minimises the distance $|\mathbf{r}^b - \tilde{\mathbf{r}}_{cod}(\Phi)|$. I found it efficient to store in the memory of the simulation a lookup table. The lookup table links an array of N values of phase, $\{\Phi_0 ... \Phi_N\}$, to an array of couples of coordinates $\{(X_0, Y_0) ... (X_n, Y_n)\}$, evaluated at $\{\Phi_0 ... \Phi_N\}$ so that $X_i = \tilde{x}_{cod}(\Phi_i)$ and $Y_i = \tilde{y}_{cod}(\Phi_i)$.

The first step is to find the point (X_j, Y_j) in the lookup table that is closest to the bead. We then need to find whether the projection of the bead will fall on the segment joining (X_{j-1}, Y_{j-1}) and (X_j, Y_j) ('left' segment), or between (X_j, Y_j) and (X_{j+1}, Y_{j+1}) ('right' segment). To do this we calculate the projections

$$l_l = d\cos\theta_l = \frac{L_l^2 + d^2 - d_l^2}{2L_l} \tag{E.1a}$$

$$l_r = d\cos\theta_r = \frac{L_r^2 + d^2 - d_r^2}{2L_r} \tag{E.1b}$$

of the bead onto the left and right segment (symbols refer to Figure E.1), and select the one where the projection is maximum. Then we find a good approximation for Φ^* by interpolating

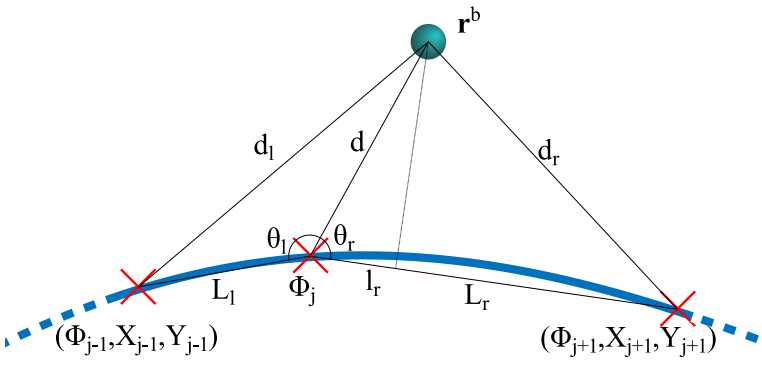

Fig. E.1 **Efficient projection of a bead onto its prescribed trajectory.** The phase of the bead along the trajectory is found by interpolating its position between entries of a lookup table. First we find between which two entries of the lookup table the bead projection will fall: in the case in the figure, the projection of the bead falls on the segment that links point j and $j+1$. We then estimate the phase of the projection of the bead along the trajectory as $\Phi^* = \Phi_j + \frac{l_r}{L_r}(\Phi_{j+1} - \Phi_j)$.

between Φ_j and the $\Phi_{j\pm1}$ (according to whether we selected the left or right segment):

$$\Phi^* = \Phi_j + \frac{l_\alpha}{L_\alpha}(\Phi_{j\pm1} - \Phi_j),$$

where $\alpha = `l', `r'$. Finally, our estimate for the projection of the bead along its trajectory is $\tilde{\mathbf{r}}_{cod}(\Phi^*)$.

E.2 Simulation parameters

As mentioned in section 6.2.2, the simulations in this thesis are realised using a C++ program that implements the Brownian Dynamics Ermak McCammon algorithm in order to integrate the equations of motion of N interacting particles, with hydrodynamically coupled Brownian fluctuations (eq. 6.2) [175].

The C++ code implements the driving force by placing the minimum of a harmonic potential a certain distance $\epsilon(\Phi)$ tangentially ahead of the projection of the bead on the prescribed trajectory (see Figure 6.4). At each time the bead i is thus subject to a driving force

$$\mathbf{F}_i = \mathbf{F}_{i,\parallel} + \mathbf{F}_{i,\perp} = k_\parallel \epsilon(\Phi)\hat{\mathbf{e}}_{i,\parallel} - k_\perp \left|\mathbf{r}^b - \tilde{\mathbf{r}}_{cod}(\Phi)\right| \hat{\mathbf{e}}_{i,\perp}. \tag{E.2}$$

The tangential component $\mathbf{F}_{i,\parallel}$ is the one that propels the bead along its orbit, while the perpendicular component $\mathbf{F}_{i,\perp}$ is a restoring force that keeps the bead on the prescribed trajectory. In the simulations featured in this work, $k_\parallel = k_\perp = k = 3\,\mathrm{pN/\mu m}$.

The simulated beads have radius $a = 1\,\mu\mathrm{m}$ and orbit along trajectories whose centres lie on the x-axis, separated by a distance $d = 15\,\mu\mathrm{m}$. The viscosity of the surrounding fluid is set to $\eta = 10^{-3}\,\mathrm{Pa\,s}$, and the temperature of the system is $T = 10\,\mathrm{K}$.

The frequency of an unperturbed rotor is set at $\nu_0 = T_0^{-1} = 15\,\mathrm{Hz}$, and we chose the integration time step (the fundamental unit of time of the simulation) so to have 6000 steps in one revolution of the bead. The integration time step is therefore $\mathrm{d}t = \frac{T_0}{6000} = 1.11 \times 10^{-5}\,\mathrm{s}$. The position of the harmonic potential is updated at every iteration, while the position of the beads and of the harmonic potentials is outputted every 10 iteration, so every $1.11 \times 10^{-4}\,\mathrm{s}$.

References

[1] R. L. Stavis and R. Hirschberg, "Phototaxis in Chlamydomonas Reinhardtii," *Journal of Cell Biology*, vol. 59, no. 2, pp. 367–377, 11 1973.

[2] J. J. Breunig, J. I. Arellano, and P. Rakic, "Cilia in the brain: going with the flow." *Nature neuroscience*, vol. 13, no. 6, pp. 654–655, 6 2010.

[3] R. A. Lyons, E. Saridogan, and O. Djahanbakhch, "The reproductive significance of human Fallopian tube cilia," *Human Reproduction Update*, vol. 12, no. 4, pp. 363–372, 3 2006.

[4] R. Bayly and J. D. Axelrod, "Pointing in the right direction: new developments in the field of planar cell polarity," *Nature Publishing Group*, vol. 12, no. 6, pp. 385–391, 6 2011.

[5] A. A. Smith, T. D. Johnson, D. J. Smith, and J. R. Blake, "Symmetry breaking cilia-driven flow in the zebrafish embryo," *Journal of Fluid Mechanics*, vol. 705, pp. 26–45, 8 2012.

[6] H. C. Berg, "Chemotaxis in bacteria." *Annual review of biophysics and bioengineering*, vol. 4, no. 00, pp. 119–36, 6 1975.

[7] M. Fliegauf, T. Benzing, and H. Omran, "When cilia go bad: cilia defects and ciliopathies." *Nature reviews. Molecular cell biology*, vol. 8, no. 11, pp. 880–93, 11 2007.

[8] Darthmouth College, "Darthmouth Electron Microscope Facility."

[9] B. Albert, J. Alexander, J. Lewis, M. Raff, K. Roberts, and P. Walter, *Molecular Biology of the Cell*. Garland Publishing, 11 2002.

[10] F. Zhou and S. Roy, "SnapShot: Motile Cilia," *Cell*, vol. 162, no. 1, pp. 224–224, 2015.

[11] G. J. Pazour and G. B. Witman, "The vertebrate primary cilium is a sensory organelle," *Current Opinion in Cell Biology*, vol. 15, no. 1, pp. 105–110, 2 2002.

[12] P. Satir and S. T. Christensen, "Overview of structure and function of mammalian cilia." *Annual review of physiology*, vol. 69, pp. 377–400, 1 2007.

[13] M. Delling, A. A. Indzhykulian, X. Liu, Y. Li, T. Xie, D. P. Corey, and D. E. Clapham, "Primary cilia are not calcium-responsive mechanosensors," *Nature*, vol. 531, no. 7596, pp. 656–660, 3 2016.

[14] T. Ishikawa, "Axoneme structure from motile cilia," *Cold Spring Harbor Perspectives in Biology*, vol. 9, no. 1, p. a028076, 1 2017.

[15] B. H. Gibbons, B. Baccetti, and I. R. Gibbons, "Live and reactivated motility in the 9 + 0 flagellum of Anguilla sperm," *Cell Motility*, vol. 5, no. 4, pp. 333–350, 1985.

[16] H. Ishikawa and W. F. Marshall, "Ciliogenesis: building the cell's antenna," *Nature Reviews Molecular Cell Biology*, vol. 12, no. 4, pp. 222–234, 4 2011.

[17] B. Guirao and J.-F. Joanny, "Spontaneous creation of macroscopic flow and metachronal waves in an array of cilia." *Biophysical journal*, vol. 92, no. 6, pp. 1900–1917, 3 2007.

[18] N. Bruot and P. Cicuta, "Emergence of polar order and cooperativity in hydrodynamically coupled model cilia." *Journal of the Royal Society, Interface / the Royal Society*, vol. 10, no. 87, p. 20130571, 7 2013.

[19] E. M. Purcell, "Life at low Reynolds number," *Am.J.Phys.*, vol. 45, no. 1, pp. 1–11, 1977.

[20] S. Vogel, *Life's Devices: The Physical World of Animals and Plants*, 1988.

[21] P. V. Bayly, B. L. Lewis, P. S. Kemp, R. B. Pless, and S. K. Dutcher, "Efficient spatiotemporal analysis of the flagellar waveform of Chlamydomonas reinhardtii," *Cytoskeleton*, vol. 67, no. 1, pp. 56–69, 1 2010.

[22] P. Bayly, B. Lewis, E. Ranz, R. Okamoto, R. Pless, and S. Dutcher, "Propulsive Forces on the Flagellum during Locomotion of Chlamydomonas reinhardtii," *Biophysical Journal*, vol. 100, no. 11, pp. 2716–2725, 6 2011.

[23] B. M. Friedrich, I. H. Riedel-Kruse, J. Howard, and F. Julicher, "High-precision tracking of sperm swimming fine structure provides strong test of resistive force theory," *Journal of Experimental Biology*, vol. 213, no. 8, pp. 1226–1234, 4 2010.

[24] C. B. Lindemann and K. A. Lesich, "Flagellar and ciliary beating: the proven and the possible." *J Cell Sci*, vol. 123, no. Pt 4, pp. 519–528, 2 2010.

[25] I. H. Riedel-Kruse, A. Hilfinger, J. Howard, and F. Jülicher, "How molecular motors shape the flagellar beat." *HFSP journal*, vol. 1, no. 3, pp. 192–208, 9 2007.

[26] J. R. Blake and a. T. Chwang, "Fundamental singularities of viscous flow," *Journal of Engineering Mathematics*, vol. 8, no. 1, pp. 23–29, 1 1974.

[27] D. M. Woolley and G. G. Vernon, "A study of helical and planar waves on sea urchin sperm flagella, with a theory of how they are generated." *The Journal of experimental biology*, vol. 204, no. Pt 7, pp. 1333–45, 4 2001.

[28] M. Salathe, "Regulation of mammalian ciliary beating." *Annual review of physiology*, vol. 69, no. 1, pp. 401–422, 1 2007.

[29] R. E. Goldstein, M. Polin, and I. Tuval, "Noise and Synchronization in Pairs of Beating Eukaryotic Flagella," *Physical Review Letters*, vol. 103, no. 16, p. 168103, 10 2009.

[30] M. J. G. Gage, "Mammalian sperm morphometry," *Proceedings of the Royal Society B: Biological Sciences*, vol. 265, no. 1391, pp. 97–103, 1 1998.

[31] D. Bray, *Cell Movement, From Molecules to Motility, 2nd Ed*. Garland Publishing, 2001.

[32] N. Bruot and P. Cicuta, "Realizing the physics of motile cilia synchronization with driven colloids," *Annual Review of Condensed Matter Physics*, vol. 7, no. 1, pp. 323–348, 10 2015.

[33] H. Guo and E. Kanso, "Evaluating efficiency and robustness in cilia design," *Physical Review E*, vol. 93, no. 3, p. 033119, 3 2016.

[34] J. L. Stubbs, E. K. Vladar, J. D. Axelrod, and C. Kintner, "Multicilin promotes centriole assembly and ciliogenesis during multiciliate cell differentiation." *Nature cell biology*, vol. 14, no. 2, pp. 140–7, 2 2012.

[35] E. K. Vladar, R. D. Bayly, A. M. Sangoram, M. P. Scott, and J. D. Axelrod, "Microtubules enable the planar cell polarity of airway cilia," *Current Biology*, vol. 22, no. 23, pp. 2203–2212, 12 2012.

[36] B. W. Bisgrove and H. J. Yost, "The roles of cilia in developmental disorders and disease." *Development (Cambridge, England)*, vol. 133, no. 21, pp. 4131–4143, 11 2006.

[37] C. J. Fowler, "Identification of a ciliary defect associated with pulmonary nontuberculous mycobacterial," Ph.D. dissertation, University of Cambridge, 2013.

[38] A. Benmerah, B. Durand, R. H. Giles, T. Harris, L. Kohl, C. Laclef, S. M. Meilhac, H. M. Mitchison, L. B. Pedersen, R. Roepman, P. Swoboda, M. Ueffing, and P. Bastin, "The more we know, the more we have to discover: an exciting future for understanding cilia and ciliopathies." *Cilia*, vol. 4, p. 5, 2015.

[39] A. Horani and T. W. Ferkol, "Primary ciliary dyskinesia and associated sensory ciliopathies," *Expert Rev Respir Med*, vol. 10, no. 5, pp. 569–576, 5 2016.

[40] A. R. Shields, B. L. Fiser, B. A. Evans, M. R. Falvo, S. Washburn, and R. Superfine, "Biomimetic cilia arrays generate simultaneous pumping and mixing regimes." *Proceedings of the National Academy of Sciences of the United States of America*, vol. 107, no. 36, pp. 15 670–5, 9 2010.

[41] S. Sareh, J. Rossiter, A. Conn, K. Drescher, and R. E. Goldstein, "Swimming like algae: biomimetic soft artificial cilia." *Journal of the Royal Society, Interface / the Royal Society*, vol. 10, no. 78, pp. 20 120 666–, 10 2012.

[42] A. Hilfinger, A. K. Chattopadhyay, and F. Jülicher, "Nonlinear dynamics of cilia and flagella," *Physical Review E - Statistical, Nonlinear, and Soft Matter Physics*, vol. 79, no. 5, p. 051918, 5 2009.

[43] B. Button, L.-H. Cai, C. Ehre, M. Kesimer, D. B. Hill, J. K. Sheehan, R. C. Boucher, and M. Rubinstein, "A Periciliary Brush Promotes the Lung Health by Separating the Mucus Layer from Airway Epithelia," *Science (New York, N.Y.)*, vol. 337, no. 6097, pp. 937–41, 8 2012.

[44] N. Bruot, J. Kotar, F. De Lillo, M. Cosentino Lagomarsino, and P. Cicuta, "Driving potential and noise level determine the synchronization state of hydrodynamically coupled oscillators," *Physical Review Letters*, vol. 109, no. 16, p. 164103, 10 2012.

[45] J. Kotar, L. Debono, N. Bruot, S. Box, D. Phillips, S. Simpson, S. Hanna, and P. Cicuta, "Optimal hydrodynamic synchronization of colloidal rotors," *Physical Review Letters*, vol. 111, no. 22, p. 228103, 11 2013.

[46] L. Damet, G. M. Cicuta, J. Kotar, M. C. Lagomarsino, and P. Cicuta, "Hydrodynamically synchronized states in active colloidal arrays," *Soft Matter*, vol. 8, no. 33, p. 8672, 2012.

[47] K. Y. Wan, K. C. Leptos, and R. E. Goldstein, "Lag, lock, sync, slip: the many 'phases' of coupled flagella," *Journal of The Royal Society Interface*, vol. 11, no. 94, pp. 20 131 160–20 131 160, 2 2014.

[48] M. Polin, I. Tuval, K. Drescher, J. P. Gollub, and R. E. Goldstein, "Chlamydomonas swims with two "gears" in a eukaryotic version of run-and-tumble locomotion," *Science (New York, N.Y.)*, vol. 325, no. 5939, pp. 487–90, 7 2009.

[49] B. M. Friedrich and F. Jülicher, "Flagellar Synchronization Independent of Hydrodynamic Interactions," *Physical Review Letters*, vol. 109, no. 13, p. 138102, 9 2012.

[50] V. F. Geyer, F. Jülicher, J. Howard, and B. M. Friedrich, "Cell-body rocking is a dominant mechanism for flagellar synchronization in a swimming alga," *Proceedings of the National Academy of Sciences*, vol. 110, no. 45, pp. 18 058–18 063, 11 2013.

[51] K. Y. Wan and R. E. Goldstein, "Coordinated beating of algal flagella is mediated by basal coupling," *Proceedings of the National Academy of Sciences*, vol. 113, no. 20, p. 201518527, 5 2016.

[52] D. R. Brumley, K. Y. Wan, M. Polin, and R. E. Goldstein, "Flagellar synchronization through direct hydrodynamic interactions," *eLife*, vol. 3, p. e02750, 7 2014.

[53] L. B. Wong, I. F. Miller, and D. B. Yeates, "Nature of the mammalian ciliary metachronal wave." *Journal of applied physiology (Bethesda, Md. : 1985)*, vol. 75, no. 1, pp. 458–67, 7 1993.

[54] M. Cosentino Lagomarsino, P. Jona, and B. Bassetti, "Metachronal waves for deterministic switching two-state oscillators with hydrodynamic interaction." *Physical review. E, Statistical, nonlinear, and soft matter physics*, vol. 68, no. 2 Pt 1, p. 021908, 8 2003.

[55] T. Niedermayer, B. Eckhardt, and P. Lenz, "Synchronization, phase locking, and metachronal wave formation in ciliary chains," *Chaos*, vol. 18, no. 3, p. 037128, 9 2008.

[56] J. Elgeti and G. Gompper, "Emergence of metachronal waves in cilia arrays." *Proceedings of the National Academy of Sciences of the United States of America*, vol. 110, no. 12, pp. 4470–5, 3 2013.

[57] N. Osterman and A. Vilfan, "Finding the ciliary beating pattern with optimal efficiency." *Proceedings of the National Academy of Sciences of the United States of America*, vol. 108, no. 38, pp. 15 727–32, 9 2011.

[58] S. Gueron, K. Levit-Gurevich, N. Liron, and J. J. Blum, "Cilia internal mechanism and metachronal coordination as the result of hydrodynamical coupling," *Proceedings of the National Academy of Sciences*, vol. 94, no. 12, pp. 6001–6006, 6 1997.

[59] D. R. Brumley, M. Polin, T. J. Pedley, and R. E. Goldstein, "Metachronal waves in the flagellar beating of Volvox and their hydrodynamic origin," *Journal of The Royal Society Interface*, vol. 12, no. 108, p. 20141358, 7 2015.

[60] D. R. Brumley, N. Bruot, J. Kotar, R. E. Goldstein, P. Cicuta, and M. Polin, "Long-range interactions, wobbles, and phase defects in chains of model cilia," *Physical Review Fluids*, vol. 1, no. 8, p. 081201, 12 2016.

[61] Y. Iwadate, "Department of Functional Molecular Biology, Yamaguchi University."

[62] R. Lhermerout, N. Bruot, G. M. Cicuta, J. Kotar, and P. Cicuta, "Collective synchronization states in arrays of driven colloidal oscillators," *New Journal of Physics*, vol. 14, no. 10, p. 105023, 10 2012.

[63] N. Bruot, "Hydrodynamic coupling and synchronization of colloidal oscillators," Ph.D. dissertation, University of Cambridge, 2013.

[64] N. Bruot, L. Damet, J. Kotar, P. Cicuta, and M. C. Lagomarsino, "Noise and synchronization of a single active colloid," *Physical Review Letters*, vol. 107, no. 9, p. 094101, 8 2011.

[65] E. Hamilton, N. Bruot, and P. Cicuta, "The chimera state in colloidal phase oscillators with hydrodynamic interaction," *Chaos: An Interdisciplinary Journal of Nonlinear Science*, vol. 27, no. 12, p. 123108, 12 2017.

[66] J. V. Fahy and B. F. Dickey, "Airway mucus function and dysfunction." *The New England journal of medicine*, vol. 363, no. 23, pp. 2233–2247, 12 2010.

[67] J. A. Whitsett and T. Alenghat, "Respiratory epithelial cells orchestrate pulmonary innate immunity." *Nature immunology*, vol. 16, no. 1, pp. 27–35, 12 2015.

[68] A. G. Beule, "Physiology and pathophysiology of respiratory mucosa of the nose and the paranasal sinuses." *GMS current topics in otorhinolaryngology, head and neck surgery*, vol. 9, p. Doc07, 1 2010.

[69] W. Hofmann and B. Asgharian, "The effect of lung structure on mucociliary clearance and particle retention in human and rat lungs," *Toxicological Sciences*, vol. 73, no. 2, pp. 448–456, 6 2003.

[70] A. E. Tilley, M. S. Walters, R. Shaykhiev, and R. G. Crystal, "Cilia dysfunction in lung disease." *Annual review of physiology*, vol. 77, pp. 379–406, 2015.

[71] J. H. Sisson, J. A. Stoner, B. A. Ammons, and T. A. Wyatt, "All-digital image capture and whole-field analysis of ciliary beat frequency," *Journal of Microscopy*, vol. 211, no. 2, pp. 103–111, 2003.

[72] T. Dalhamn and R. Rylander, "Frequency of Ciliary Beat measured with a Photo-sensitive Cell," *Nature*, vol. 196, no. 4854, pp. 592–593, 11 1962.

[73] H. Teichtahl, P. L. Wright, and R. L. G. Kirsner, "Measurement of in vitro ciliary beat frequency: A television-video modification of the transmitted light technique," *Medical & Biological Engineering & Computing*, vol. 24, no. 2, pp. 193–196, 3 1986.

[74] C. O'Callaghan, K. Smith, M. Wilkinson, D. Morgan, and K. Priftis, "Ciliary beat frequency in newborn infants." *Archives of Disease in Childhood*, vol. 66, no. 4 Spec No, pp. 443–444, 4 1991.

[75] M. A. Chilvers and C. O'Callaghan, "Analysis of ciliary beat pattern and beat frequency using digital high speed imaging: comparison with the photomultiplier and photodiode methods," *Thorax*, vol. 55, no. 4, pp. 314–317, 2000.

[76] M. A. K. Olm, J. E. Kögler, M. Macchione, A. Shoemark, P. H. N. Saldiva, and J. C. Rodrigues, "Primary ciliary dyskinesia: evaluation using cilia beat frequency assessment via spectral analysis of digital microscopy images," *Journal of Applied Physiology*, vol. 111, no. 1, pp. 295–302, 7 2011.

[77] O. Meste, F. Brau, and A. Guyon, "Robust estimation of the motile cilia beating frequency," *Medical and Biological Engineering and Computing*, vol. 53, no. 10, pp. 1025–1035, 10 2015.

[78] C. M. Smith, J. Djakow, R. C. Free, P. Djakow, R. Lonnen, G. Williams, P. Pohunek, R. A. Hirst, A. J. Easton, P. W. Andrew, and C. O'Callaghan, "ciliaFA: a research tool for automated, high-throughput measurement of ciliary beat frequency using freely available software." *Cilia*, vol. 1, no. 1, p. 14, 1 2012.

[79] E. Parrilla, M. Armengot, M. Mata, J. M. Sánchez-Vílchez, J. Cortijo, J. L. Hueso, J. Riera, and D. Moratal, "Primary ciliary dyskinesia assessment by means of optical flow analysis of phase-contrast microscopy images," *Computerized Medical Imaging and Graphics*, vol. 38, no. 3, pp. 163–170, 4 2014.

[80] M. Figl, M. Lechner, T. Werther, F. Horak, J. Hummel, and W. Birkfellner, "Automatic analysis of ciliary beat frequency using optical flow," in *Proc. SPIE 8314, Medical Imaging 2012: Image Processing*, D. R. Haynor and S. Ourselin, Eds., vol. 8314, 2 2012, p. 831453. [Online]. Available: http://proceedings.spiedigitallibrary.org/proceeding.aspx?doi=10.1117/12.911616

[81] W. Kim, T. H. Han, H. J. Kim, M. Y. Park, K. S. Kim, and R. W. Park, "An automated measurement of ciliary beating frequency using a combined optical flow and peak detection," *Healthcare Informatics Research*, vol. 17, no. 2, pp. 111–119, 2011.

[82] G. Mantovani, M. Pifferi, and G. Vozzi, "Automated software for analysis of ciliary beat frequency and metachronal wave orientation in primary ciliary dyskinesia," *Eur Arch Otorhinolaryngol*, vol. 267, no. 6, pp. 897–902, 6 2010.

[83] S. P. Quinn, M. J. Zahid, J. R. Durkin, R. J. Francis, C. W. Lo, and S. C. Chennubhotla, "Automated identification of abnormal respiratory ciliary motion in nasal biopsies," *Science Translational Medicine*, vol. 7, no. 299, pp. 124–299, 2015.

[84] D. Eshel and Z. Priel, "Characterization of metachronal wave of beating cilia on frog's palate epithelium in tissue culture." *The Journal of Physiology*, vol. 388, no. 1, pp. 1–8, 7 1987.

[85] L. Gheber and Z. Priel, "Synchronization between beating cilia," *Biophysical Journal*, vol. 55, no. 1, pp. 183–191, 1 1989.

[86] L. Gheber and Z. Priel, "Metachronal activity of cultured mucociliary epithelium under normal and stimulated conditions," *Cell Motility and the Cytoskeleton*, vol. 28, no. 4, pp. 333–345, 1994.

[87] L. Gheber, A. Korngreen, and Z. Priel, "Effect of viscosity on metachrony in mucus propelling cilia," *Cell Motility and the Cytoskeleton*, vol. 39, no. 1, pp. 9–20, 1998.

[88] W.-J. Yi, K.-S. Park, C.-H. Lee, C.-S. Rhee, and S.-W. Nam, "Directional disorder of ciliary metachronal waves using two-dimensional correlation map." *IEEE transactions on bio-medical engineering*, vol. 49, no. 3, pp. 269–73, 3 2002.

[89] M. Ryser, A. Burn, T. Wessel, M. Frenz, and J. Rička, "Functional imaging of mucociliary phenomena: High-speed digital reflection contrast microscopy," *European Biophysics Journal*, vol. 37, no. 1, pp. 35–54, 11 2007.

[90] G. Schätz, M. Schneiter, J. Rička, K. Kühni-Boghenbor, S. Tschanz, M. Doherr, M. Frenz, and M. Stoffel, "Ciliary Beating Plane and Wave Propagation in the Bovine Oviduct," *Cells Tissues Organs*, vol. 198, no. 6, pp. 457–469, 2013.

[91] P. R. Sears, K. Thompson, M. R. Knowles, and C. W. Davis, "Human airway ciliary dynamics." *American journal of physiology. Lung cellular and molecular physiology*, vol. 304, no. 3, pp. 170–83, 2013.

[92] L. Liu, K. K. Chu, G. H. Houser, B. J. Diephuis, Y. Li, E. J. Wilsterman, S. Shastry, G. Dierksen, S. E. Birket, M. Mazur, S. Byan-Parker, W. E. Grizzle, E. J. Sorscher, S. M. Rowe, and G. J. Tearney, "Method for Quantitative Study of Airway Functional Microanatomy Using Micro-Optical Coherence Tomography," *PLoS ONE*, vol. 8, no. 1, pp. 1–8, 2013.

[93] M. J. Sanderson and M. A. Sleigh, "Ciliary Activity of Cultured Rabbit Tracheal Epithelium: Beat Pattern and Metachrony," *J. Cell Sci*, vol. 47, pp. 331–347, 1981.

[94] K. C. Leptos, K. Y. Wan, M. Polin, I. Tuval, A. I. Pesci, and R. E. Goldstein, "Antiphase Synchronization in a Flagellar-Dominance Mutant of Chlamydomonas," *Physical Review Letters*, vol. 111, no. 15, p. 158101, 10 2013.

[95] P. V. Bayly and K. S. Wilson, "Analysis of unstable modes distinguishes mathematical models of flagellar motion," *Journal of The Royal Society Interface*, vol. 12, no. 106, pp. 20 150 124–20 150 124, 4 2015.

[96] D. I. Barlow and M. A. Sleigh, "Freeze substitution for preservation of ciliated surfaces for scanning electron microscopy," *Journal of Microscopy*, vol. 115, no. 1, pp. 81–95, 1 1979.

[97] D. Cui, K. K. Chu, B. Yin, T. N. Ford, C. Hyun, H. M. Leung, J. A. Gardecki, G. M. Solomon, S. E. Birket, L. Liu, S. M. Rowe, and G. J. Tearney, "Flexible, high-resolution micro-optical coherence tomography endobronchial probe toward in vivo imaging of cilia," *Optics Letters*, vol. 42, no. 4, p. 867, 2 2017.

[98] M. A. Chilvers, A. Rutman, and C. O'Callaghan, "Ciliary beat pattern is associated with specific ultrastructural defects in primary ciliary dyskinesia." *The Journal of allergy and clinical immunology*, vol. 112, no. 3, pp. 518–24, 2003.

[99] J.-F. Papon, L. Bassinet, G. Cariou-Patron, F. Zerah-Lancner, A.-M. Vojtek, S. Blanchon, B. Crestani, S. Amselem, A. Coste, B. Housset, E. Escudier, and B. Louis, "Quantitative analysis of ciliary beating in primary ciliary dyskinesia: a pilot study," *Orphanet Journal of Rare Diseases*, vol. 7, no. 1, p. 78, 10 2012.

[100] B. P. O'Sullivan and S. D. Freedman, "Cystic fibrosis," *The Lancet*, vol. 373, no. 9678, pp. 1891–1904, 5 2009.

[101] J. S. Lucas, A. Barbato, S. A. Collins, M. Goutaki, L. Behan, D. Caudri, S. Dell, E. Eber, E. Escudier, R. A. Hirst, C. Hogg, M. Jorissen, P. Latzin, M. Legendre, M. W. Leigh, F. Midulla, K. G. Nielsen, H. Omran, J.-F. Papon, P. Pohunek, B. Redfern, D. Rigau, B. Rindlisbacher, F. Santamaria, A. Shoemark, D. Snijders, T. Tonia, A. Titieni, W. T. Walker, C. Werner, A. Bush, and C. E. Kuehni, "European Respiratory Society guidelines for the diagnosis of primary ciliary dyskinesia," *European Respiratory Journal*, vol. 49, no. 1, p. 1601090, 1 2017.

[102] R. Cerbino and V. Trappe, "Differential dynamic microscopy: Probing wave vector dependent dynamics with a microscope," *Physical Review Letters*, vol. 100, no. 18, p. 188102, 5 2008.

[103] F. Giavazzi and R. Cerbino, "Digital Fourier microscopy for soft matter dynamics," *Journal of Optics*, vol. 16, no. 8, p. 083001, 8 2014.

[104] F. Giavazzi, S. Crotti, A. Speciale, F. Serra, G. Zanchetta, V. Trappe, M. Buscaglia, T. Bellini, and R. Cerbino, "Viscoelasticity of nematic liquid crystals at a glance," *Soft Matter*, vol. 10, no. 22, pp. 3938–3949, 6 2014.

[105] F. Ferri, A. D'Angelo, M. Lee, A. Lotti, M. C. Pigazzini, K. Singh, and R. Cerbino, "Kinetics of colloidal fractal aggregation by differential dynamic microscopy," *European Physical Journal: Special Topics*, vol. 199, no. 1, pp. 139–148, 12 2011.

[106] L. G. Wilson, V. A. Martinez, J. Schwarz-Linek, J. Tailleur, G. Bryant, P. N. Pusey, and W. C. K. Poon, "Differential dynamic microscopy of bacterial motility," *Physical Review Letters*, vol. 106, no. 1, p. 018101, 1 2011.

[107] F. Giavazzi, D. Brogioli, V. Trappe, T. Bellini, and R. Cerbino, "Scattering information obtained by optical microscopy: Differential dynamic microscopy and beyond," *Physical Review E - Statistical, Nonlinear, and Soft Matter Physics*, vol. 80, no. 3, p. 031403, 9 2009.

[108] B. J. Berne and R. Pecora, *Dynamic Light Scattering*, R. Pecora, Ed. Boston, MA: Springer US, 1985.

[109] V. A. Martinez, R. Besseling, O. A. Croze, J. Tailleur, M. Reufer, J. Schwarz-Linek, L. G. Wilson, M. A. Bees, and W. C. K. Poon, "Differential dynamic microscopy: A high-throughput method for characterizing the motility of microorganisms," *Biophysical Journal*, vol. 103, no. 8, pp. 1637–1647, 10 2012.

[110] R. Cerbino and P. Cicuta, "Perspective: Differential dynamic microscopy extracts multi-scale activity in complex fluids and biological systems," *The Journal of Chemical Physics*, vol. 147, no. 11, p. 110901, 9 2017.

[111] M. Reufer, V. A. Martinez, P. Schurtenberger, and W. C. K. Poon, "Differential dynamic microscopy for anisotropic colloidal dynamics," *Langmuir*, vol. 28, no. 10, pp. 4618–4624, 3 2012.

[112] A. Dehaoui, B. Issenmann, and F. Caupin, "Viscosity of deeply supercooled water and its coupling to molecular diffusion," *Proceedings of the National Academy of Sciences*, vol. 112, no. 39, pp. 12 020–12 025, 9 2015.

[113] J. D. C. Jacob, K. He, S. T. Retterer, R. Krishnamoorti, and J. C. Conrad, "Diffusive dynamics of nanoparticles in ultra-confined media," *Soft Matter*, vol. 11, no. 38, pp. 7515–7524, 2015.

[114] P. J. Lu, F. Giavazzi, T. E. Angelini, E. Zaccarelli, F. Jargstorff, A. B. Schofield, J. N. Wilking, M. B. Romanowsky, D. A. Weitz, and R. Cerbino, "Characterizing concentrated, multiply scattering, and actively driven fluorescent systems with confocal differential dynamic microscopy," *Physical Review Letters*, vol. 108, no. 21, p. 218103, 5 2012.

[115] M. Drechsler, F. Giavazzi, R. Cerbino, and I. M. Palacios, "Active diffusion and advection in Drosophila oocytes result from the interplay of actin and microtubules," *Nature Communications*, vol. 8, no. 1, p. 1520, 12 2017.

[116] T. Sentjabrskaja, E. Zaccarelli, C. De Michele, F. Sciortino, P. Tartaglia, T. Voigtmann, S. U. Egelhaaf, and M. Laurati, "Anomalous dynamics of intruders in a crowded environment of mobile obstacles," *Nature Communications*, vol. 7, p. 11133, 4 2016.

[117] M. S. Safari, R. Poling-Skutvik, P. G. Vekilov, and J. C. Conrad, "Differential dynamic microscopy of bidisperse colloidal suspensions," *npj Microgravity*, vol. 3, no. 1, p. 21, 12 2017.

[118] Y. Gao, J. Kim, and M. E. Helgeson, "Microdynamics and arrest of coarsening during spinodal decomposition in thermoreversible colloidal gels," *Soft Matter*, vol. 11, no. 32, pp. 6360–6370, 2015.

[119] F. Giavazzi, C. Haro-Pérez, and R. Cerbino, "Simultaneous characterization of rotational and translational diffusion of optically anisotropic particles by optical microscopy," *Journal of Physics: Condensed Matter*, vol. 28, no. 19, p. 195201, 5 2016.

[120] D. M. Wulstein and R. McGorty, "Point-spread function engineering enhances digital Fourier microscopy," *Optics Letters*, vol. 42, no. 22, p. 4603, 11 2017.

[121] P. Edera, D. Bergamini, V. Trappe, F. Giavazzi, and R. Cerbino, "Differential dynamic microscopy microrheology of soft materials: A tracking-free determination of the frequency-dependent loss and storage moduli," *Physical Review Materials*, vol. 1, no. 7, p. 073804, 12 2017.

[122] N. Otsu, "A Threshold Selection Method from Gray-Level Histograms," *IEEE Transactions on Systems, Man, and Cybernetics*, vol. 9, no. 1, pp. 62–66, 1 1979.

[123] J. L. Devalia, R. J. Sapsford, C. W. Wells, P. Richman, and R. J. Davies, "Culture and comparison of human bronchial and nasal epithelial cells in vitro." *Respiratory medicine*, vol. 84, no. 4, pp. 303–12, 7 1990.

[124] C. Horrocks, "Blast Injuries: Biophysics, Pathophysiology and Management Principles," *Journal of the Royal Army Medical Corps*, vol. 147, no. 1, pp. 28–40, 2 2001.

[125] G. R. Cutting, "Cystic fibrosis genetics: From molecular understanding to clinical application," *Nature Reviews Genetics*, vol. 16, no. 1, pp. 45–56, 2015.

[126] L. Romani, V. Oikonomou, S. Moretti, R. G. Iannitti, M. C. D'Adamo, V. R. Villella, M. Pariano, L. Sforna, M. Borghi, M. M. Bellet, F. Fallarino, M. T. Pallotta, G. Servillo, E. Ferrari, P. Puccetti, G. Kroemer, M. Pessia, L. Maiuri, A. L. Goldstein, and E. Garaci, "Thymosin $\alpha 1$ represents a potential potent single-molecule-based therapy for cystic fibrosis," *Nature Medicine*, vol. 23, no. 5, pp. 590–600, 4 2017.

[127] C. Ehre, C. Ridley, and D. J. Thornton, "Cystic fibrosis: An inherited disease affecting mucin-producing organs," *The International Journal of Biochemistry & Cell Biology*, vol. 52, pp. 136–145, 7 2014.

[128] R. C. Boucher, "Airway Surface Dehydration in Cystic Fibrosis: Pathogenesis and Therapy," *Annual Review of Medicine*, vol. 58, no. 1, pp. 157–170, 2 2007.

[129] J. F. Dekkers, G. Berkers, E. Kruisselbrink, A. Vonk, H. R. de Jonge, H. M. Janssens, I. Bronsveld, E. A. van de Graaf, E. E. S. Nieuwenhuis, R. H. J. Houwen, F. P. Vleggaar, J. C. Escher, Y. B. de Rijke, C. J. Majoor, H. G. M. Heijerman, K. M. de Winter–de Groot, H. Clevers, C. K. van der Ent, and J. M. Beekman, "Characterizing responses to CFTR-modulating drugs using rectal organoids derived from subjects with cystic fibrosis," *Science Translational Medicine*, vol. 8, no. 344, pp. 84–344, 6 2016.

[130] S. K. Lai, Y.-Y. Wang, D. Wirtz, and J. Hanes, "Micro- and macrorheology of mucus," *Advanced Drug Delivery Reviews*, vol. 61, no. 2, pp. 86–100, 2 2009.

[131] B. Demouveaux, V. Gouyer, F. Gottrand, T. Narita, and J.-L. Desseyn, "Gel-forming mucin interactome drives mucus viscoelasticity," *Advances in Colloid and Interface Science*, vol. 252, pp. 69–82, 2 2018.

[132] G. Tomaiuolo, G. Rusciano, S. Caserta, A. Carciati, V. Carnovale, P. Abete, A. Sasso, and S. Guido, "A New Method to Improve the Clinical Evaluation of Cystic Fibrosis Patients by Mucus Viscoelastic Properties," *PLoS ONE*, vol. 9, no. 1, p. e82297, 1 2014.

[133] D. B. Hill, P. A. Vasquez, J. Mellnik, S. A. McKinley, A. Vose, F. Mu, A. G. Henderson, S. H. Donaldson, N. E. Alexis, R. C. Boucher, and M. G. Forest, "A Biophysical Basis for Mucus Solids Concentration as a Candidate Biomarker for Airways Disease," *PLoS ONE*, vol. 9, no. 2, p. e87681, 2 2014.

[134] M. Sedaghat, M. Shahmardan, M. Norouzi, M. Nazari, and P. Jayathilake, "On the effect of mucus rheology on the muco-ciliary transport," *Mathematical Biosciences*, vol. 272, pp. 44–53, 2 2016.

[135] A. G. Henderson, C. Ehre, B. Button, L. H. Abdullah, L.-H. Cai, M. W. Leigh, G. C. DeMaria, H. Matsui, S. H. Donaldson, C. W. Davis, J. K. Sheehan, R. C. Boucher, and M. Kesimer, "Cystic fibrosis airway secretions exhibit mucin hyperconcentration and increased osmotic pressure," *Journal of Clinical Investigation*, vol. 124, no. 7, pp. 3047–3060, 7 2014.

[136] G. A. Duncan, J. Jung, A. Joseph, A. L. Thaxton, N. E. West, M. P. Boyle, J. Hanes, and J. S. Suk, "Microstructural alterations of sputum in cystic fibrosis lung disease," *JCI Insight*, vol. 1, no. 18, 11 2016.

[137] F. Van Goor, S. Hadida, P. D. J. Grootenhuis, B. Burton, J. H. Stack, K. S. Straley, C. J. Decker, M. Miller, J. McCartney, E. R. Olson, J. J. Wine, R. A. Frizzell, M. Ashlock, and P. A. Negulescu, "Correction of the F508del-CFTR protein processing defect in vitro by the investigational drug VX-809," *Proceedings of the National Academy of Sciences*, vol. 108, no. 46, pp. 18 843–18 848, 11 2011.

[138] K. Kuk and J. L. Taylor-Cousar, "Lumacaftor and ivacaftor in the management of patients with cystic fibrosis: current evidence and future prospects," *Therapeutic Advances in Respiratory Disease*, vol. 9, no. 6, pp. 313–326, 12 2015.

[139] J. P. Clancy, S. M. Rowe, F. J. Accurso, M. L. Aitken, R. S. Amin, M. A. Ashlock, M. Ballmann, M. P. Boyle, I. Bronsveld, P. W. Campbell, K. De Boeck, S. H. Donaldson, H. L. Dorkin, J. M. Dunitz, P. R. Durie, M. Jain, A. Leonard, K. S. McCoy, R. B. Moss, J. M. Pilewski, D. B. Rosenbluth, R. C. Rubenstein, M. S. Schechter, M. Botfield, C. L. Ordoñez, G. T. Spencer-Green, L. Vernillet, S. Wisseh, K. Yen, and M. W. Konstan, "Results of a phase IIa study of VX-809, an investigational CFTR corrector compound, in subjects with cystic fibrosis homozygous for the F508del-CFTR mutation," *Thorax*, vol. 67, no. 1, pp. 12–18, 1 2012.

[140] F. Van Goor, S. Hadida, P. D. J. Grootenhuis, B. Burton, D. Cao, T. Neuberger, A. Turnbull, A. Singh, J. Joubran, A. Hazlewood, J. Zhou, J. McCartney, V. Arumugam, C. Decker, J. Yang, C. Young, E. R. Olson, J. J. Wine, R. A. Frizzell, M. Ashlock, and P. Negulescu, "Rescue of CF airway epithelial cell function in vitro by a CFTR potentiator, VX-770," *Proceedings of the National Academy of Sciences*, vol. 106, no. 44, pp. 18 825–18 830, 11 2009.

[141] C. E. Wainwright, J. S. Elborn, B. W. Ramsey, G. Marigowda, X. Huang, M. Cipolli, C. Colombo, J. C. Davies, K. De Boeck, P. A. Flume, M. W. Konstan, S. A. McColley, K. McCoy, E. F. McKone, A. Munck, F. Ratjen, S. M. Rowe, D. Waltz, and M. P. Boyle, "Lumacaftor–Ivacaftor in Patients with Cystic Fibrosis Homozygous for Phe508del CFTR," *New England Journal of Medicine*, vol. 373, no. 3, pp. 220–231, 7 2015.

[142] C. W. Tuthill and R. S. King, "Thymosin Apha 1–A Peptide Immune Modulator with a Broad Range of Clinical Applications," *Clinical & Experimental Pharmacology*, vol. 03, no. 04, pp. 1–17, 2013.

[143] L. Feriani, M. Juenet, C. J. Fowler, N. Bruot, M. Chioccioli, S. M. Holland, C. E. Bryant, and P. Cicuta, "Assessing the Collective Dynamics of Motile Cilia in Cultures of Human Airway Cells by Multiscale DDM," *Biophysical Journal*, vol. 113, no. 1, pp. 109–119, 7 2017.

[144] S. D. Reynolds, C. Rios, A. Wesolowska-Andersen, Y. Zhuang, M. Pinter, C. Happoldt, C. L. Hill, S. W. Lallier, G. P. Cosgrove, G. M. Solomon, D. P. Nichols, and M. A. Seibold, "Airway Progenitor Clone Formation Is Enhanced by Y-27632–Dependent Changes in the Transcriptome," *American Journal of Respiratory Cell and Molecular Biology*, vol. 55, no. 3, pp. 323–336, 9 2016.

[145] S. Yuan, M. Hollinger, M. E. Lachowicz-Scroggins, S. C. Kerr, E. M. Dunican, B. M. Daniel, S. Ghosh, S. C. Erzurum, B. Willard, S. L. Hazen, X. Huang, S. D. Carrington, S. Oscarson, and J. V. Fahy, "Oxidation increases mucin polymer cross-links to stiffen airway mucus gels," *Science Translational Medicine*, vol. 7, no. 276, pp. 27–276, 2 2015.

[146] H. H. Ussing and K. Zerahn, "Active Transport of Sodium as the Source of Electric Current in the Short-circuited Isolated Frog Skin." *Acta Physiologica Scandinavica*, vol. 23, no. 2-3, pp. 110–127, 10 1951.

[147] H. Li, D. N. Sheppard, and M. J. Hug, "Transepithelial electrical measurements with the Ussing chamber," *Journal of Cystic Fibrosis*, vol. 3, no. SUPPL. 2, pp. 123–126, 8 2004.

[148] J. F. Dekkers, C. L. Wiegerinck, H. R. de Jonge, I. Bronsveld, H. M. Janssens, K. M. de Winter-de Groot, A. M. Brandsma, N. W. M. de Jong, M. J. C. Bijvelds, B. J. Scholte, E. E. S. Nieuwenhuis, S. van den Brink, H. Clevers, C. K. van der Ent, S. Middendorp, and J. M. Beekman, "A functional CFTR assay using primary cystic fibrosis intestinal organoids," *Nature Medicine*, vol. 19, no. 7, pp. 939–945, 7 2013.

[149] J. F. Reiter and M. R. Leroux, "Genes and molecular pathways underpinning ciliopathies," *Nature Reviews Molecular Cell Biology*, vol. 18, no. 9, pp. 533–547, 7 2017.

[150] C. Fisch and P. Dupuis-Williams, "Ultrastructure of cilia and flagella - back to the future!" *Biology of the Cell*, vol. 103, no. 6, pp. 249–270, 6 2011.

[151] R. Faubel, C. Westendorf, E. Bodenschatz, and G. Eichele, "Cilia-based flow network in the brain ventricles," *Science*, vol. 353, no. 6295, pp. 176–178, 7 2016.

[152] M. A. Zariwala, M. R. Knowles, and H. Omran, "Genetic Defects in Ciliary Structure and Function," *Annual Review of Physiology*, vol. 69, no. 1, pp. 423–450, 3 2007.

[153] J. Raidt, J. Wallmeier, R. Hjeij, J. G. Onnebrink, P. Pennekamp, N. T. Loges, H. Olbrich, K. Häffner, G. W. Dougherty, H. Omran, and C. Werner, "Ciliary beat pattern and frequency in genetic variants of primary ciliary dyskinesia," *European Respiratory Journal*, vol. 44, no. 6, pp. 1579–1588, 12 2014.

[154] C. L. Jackson, L. Behan, S. A. Collins, P. M. Goggin, E. C. Adam, J. L. Coles, H. J. Evans, A. Harris, P. Lackie, S. Packham, A. Page, J. Thompson, W. T. Walker, C. Kuehni, and J. S. Lucas, "Accuracy of diagnostic testing in primary ciliary dyskinesia," *European Respiratory Journal*, vol. 47, no. 3, pp. 837–848, 3 2016.

[155] M. R. Knowles, L. A. Daniels, S. D. Davis, M. A. Zariwala, and M. W. Leigh, "Primary Ciliary Dyskinesia. Recent Advances in Diagnostics, Genetics, and Characterization of Clinical Disease," *American Journal of Respiratory and Critical Care Medicine*, vol. 188, no. 8, pp. 913–922, 10 2013.

[156] A. Shoemark and C. Hogg, "Electron tomography of respiratory cilia," *Thorax*, vol. 68, no. 2, pp. 190–191, 2 2013.

[157] L. Bartoloni, J.-L. Blouin, Y. Pan, C. Gehrig, A. K. Maiti, N. Scamuffa, C. Rossier, M. Jorissen, M. Armengot, M. Meeks, H. M. Mitchison, E. M. K. Chung, C. D. Delozier-Blanchet, W. J. Craigen, and S. E. Antonarakis, "Mutations in the DNAH11 (axonemal heavy chain dynein type 11) gene cause one form of situs inversus totalis and most likely primary ciliary dyskinesia," *Proceedings of the National Academy of Sciences*, vol. 99, no. 16, pp. 10 282–10 286, 8 2002.

[158] G. C. Schwabe, K. Hoffmann, N. T. Loges, D. Birker, C. Rossier, M. M. de Santi, H. Olbrich, M. Fliegauf, M. Failly, U. Liebers, M. Collura, G. Gaedicke, S. Mundlos, U. Wahn, J.-L. Blouin, B. Niggemann, H. Omran, S. E. Antonarakis, and L. Bartoloni, "Primary ciliary dyskinesia associated with normal axoneme ultrastructure is caused by DNAH11 mutations," *Human Mutation*, vol. 29, no. 2, pp. 289–298, 2 2008.

[159] M. Pifferi, A. Michelucci, M. E. Conidi, A. M. Cangiotti, P. Simi, P. Macchia, and A. L. Boner, "New DNAH11 mutations in primary ciliary dyskinesia with normal axonemal ultrastructure," *European Respiratory Journal*, vol. 35, no. 6, pp. 1413–1416, 6 2010.

[160] G. M. Solomon, R. Francis, K. K. Chu, S. E. Birket, G. Gabriel, J. E. Trombley, K. L. Lemke, N. Klena, B. Turner, G. J. Tearney, C. W. Lo, and S. M. Rowe, "Assessment of ciliary phenotype in primary ciliary dyskinesia by micro-optical coherence tomography," *JCI Insight*, vol. 2, no. 5, p. e91702, 3 2017.

[161] Z. Bukowy, E. Ziętkiewicz, and M. Witt, "In vitro culturing of ciliary respiratory cells—a model for studies of genetic diseases," *Journal of Applied Genetics*, vol. 52, no. 1, pp. 39–51, 2 2011.

[162] M. S. Elliot and W. C. Poon, "Conventional optical microscopy of colloidal suspensions," *Advances in Colloid and Interface Science*, vol. 92, no. 1-3, pp. 133–194, 9 2001.

[163] H. Olbrich, M. Schmidts, C. Werner, A. Onoufriadis, N. T. Loges, J. Raidt, N. F. Banki, A. Shoemark, T. Burgoyne, S. Al Turki, M. E. Hurles, G. Köhler, J. Schroeder, G. Nürnberg, P. Nürnberg, E. M. Chung, R. Reinhardt, J. K. Marthin, K. G. Nielsen, H. M. Mitchison, and H. Omran, "Recessive HYDIN Mutations Cause Primary Ciliary Dyskinesia without Randomization of Left-Right Body Asymmetry," *The American Journal of Human Genetics*, vol. 91, no. 4, pp. 672–684, 10 2012.

[164] D. B. Hill, V. Swaminathan, A. Estes, J. Cribb, E. T. O'Brien, C. W. Davis, and R. Superfine, "Force generation and dynamics of individual cilia under external loading," *Biophysical Journal*, vol. 98, no. 1, pp. 57–66, 2010.

[165] K. Y. Wan and R. E. Goldstein, "Rhythmicity, Recurrence, and Recovery of Flagellar Beating," *Physical Review Letters*, vol. 113, no. 23, p. 238103, 12 2014.

[166] K. S. Wilson, O. Gonzalez, S. K. Dutcher, and P. V. Bayly, "Dynein-deficient flagella respond to increased viscosity with contrasting changes in power and recovery strokes," *Cytoskeleton*, vol. 72, no. 9, pp. 477–490, 2015.

[167] S. Werner, J. C. Rink, I. H. Riedel-Kruse, and B. M. Friedrich, "Shape Mode Analysis Exposes Movement Patterns in Biology: Flagella and Flatworms as Case Studies," *PLoS ONE*, vol. 9, no. 11, p. e113083, 11 2014.

[168] G. J. Stephens, B. Johnson-Kerner, W. Bialek, and W. S. Ryu, "Dimensionality and Dynamics in the Behavior of C. elegans," *PLoS Computational Biology*, vol. 4, no. 4, p. e1000028, 4 2008.

[169] J. Kotar, M. Leoni, B. Bassetti, M. C. Lagomarsino, and P. Cicuta, "Hydrodynamic synchronization of colloidal oscillators," *Proceedings of the National Academy of Sciences*, vol. 107, no. 17, pp. 7669–7673, 4 2010.

[170] N. Uchida and R. Golestanian, "Generic Conditions for Hydrodynamic Synchronization," *Physical Review Letters*, vol. 106, no. 5, p. 058104, 2 2011.

[171] N. Uchida and R. Golestanian, "Hydrodynamic synchronization between objects with cyclic rigid trajectories," *The European Physical Journal E*, vol. 35, no. 12, p. 135, 12 2012.

[172] A. Maestro, N. Bruot, J. Kotar, N. Uchida, and R. Golestanian, "Control of synchronization in models of hydrodynamically coupled motile cilia," *Submitted*.

[173] G. Perkins and R. Jones, "Hydrodynamic interaction of a spherical particle with a planar boundary," *Physica A: Statistical Mechanics and its Applications*, vol. 189, no. 3-4, pp. 447–477, 11 1992.

[174] J. R. Blake, "A note on the image system for a stokeslet in a no-slip boundary," *Mathematical Proceedings of the Cambridge Philosophical Society*, vol. 70, no. 02, p. 303, 9 1971.

[175] D. L. Ermak and J. A. McCammon, "Brownian dynamics with hydrodynamic interactions," *The Journal of Chemical Physics*, vol. 69, no. 4, pp. 1352–1360, 8 1978.

[176] W. Thielicke and E. J. Stamhuis, "PIVlab – Towards User-friendly, Affordable and Accurate Digital Particle Image Velocimetry in MATLAB," *Journal of Open Research Software*, vol. 2, 10 2014.

[177] C. M. Smith, R. A. Hirst, M. J. Bankart, D. W. Jones, A. J. Easton, P. W. Andrew, and C. O'Callaghan, "Cooling of Cilia Allows Functional Analysis of the Beat Pattern for Diagnostic Testing," *Chest*, vol. 140, no. 1, pp. 186–190, 7 2011.

[178] M. W. Leigh, J. E. Pittman, J. L. Carson, T. W. Ferkol, S. D. Dell, S. D. Davis, M. R. Knowles, and M. A. Zariwala, "Clinical and genetic aspects of primary ciliary dyskinesia/Kartagener syndrome." *Genetics in medicine : official journal of the American College of Medical Genetics*, vol. 11, no. 7, pp. 473–87, 7 2009.

[179] M. W. Leigh, C. O'Callaghan, and M. R. Knowles, "The Challenges of Diagnosing Primary Ciliary Dyskinesia," *Proceedings of the American Thoracic Society*, vol. 8, no. 5, pp. 434–437, 9 2011.

[180] N. R. Friedman, R. Pachigolla, R. W. Deskin, and H. K. Hawkins, "Optimal Technique to Diagnose Primary Ciliary Dyskinesia," *The Laryngoscope*, vol. 110, no. 9, pp. 1548–1551, 9 2000.

[181] J. S. Lucas, A. Burgess, H. M. Mitchison, E. Moya, M. Williamson, and C. Hogg, "Diagnosis and management of primary ciliary dyskinesia," *Archives of Disease in Childhood*, vol. 99, no. 9, pp. 850–856, 9 2014.

[182] D. Sun, S. Roth, and M. J. Black, "Secrets of optical flow estimation and their principles," in *2010 IEEE Computer Society Conference on Computer Vision and Pattern Recognition*. IEEE, 6 2010, pp. 2432–2439. [Online]. Available: http://ieeexplore.ieee.org/document/5539939/

[183] H. Matsui, S. H. Randell, S. W. Peretti, C. W. Davis, and R. C. Boucher, "Coordinated clearance of periciliary liquid and mucus from airway surfaces." *Journal of Clinical Investigation*, vol. 102, no. 6, pp. 1125–1131, 9 1998.

[184] J. Hussong, R. Lindken, P. Faulhammer, K. Noreikat, K. Sharp, W. Kummer, and J. Westerweel, "Cilia-driven particle and fluid transport over mucus-free mice tracheae," *Journal of Biomechanics*, vol. 46, no. 3, pp. 593–598, 2 2013.

[185] P. Jayathilake, Z. Tan, D. Le, H. Lee, and B. Khoo, "Three-dimensional numerical simulations of human pulmonary cilia in the periciliary liquid layer by the immersed boundary method," *Computers & Fluids*, vol. 67, pp. 130–137, 8 2012.